

This electronic thesis or dissertation has been downloaded from the King's Research Portal at <https://kclpure.kcl.ac.uk/portal/>



Characterisation of human induced pluripotent stem cells in 3D artificial microenvironment using high content analysis

Alsehli, Haneen

Awarding institution:
King's College London

The copyright of this thesis rests with the author and no quotation from it or information derived from it may be published without proper acknowledgement.

END USER LICENCE AGREEMENT



Unless another licence is stated on the immediately following page this work is licensed

under a Creative Commons Attribution-NonCommercial-NoDerivatives 4.0 International

licence. <https://creativecommons.org/licenses/by-nc-nd/4.0/>

You are free to copy, distribute and transmit the work

Under the following conditions:

- Attribution: You must attribute the work in the manner specified by the author (but not in any way that suggests that they endorse you or your use of the work).
- Non Commercial: You may not use this work for commercial purposes.
- No Derivative Works - You may not alter, transform, or build upon this work.

Any of these conditions can be waived if you receive permission from the author. Your fair dealings and other rights are in no way affected by the above.

Take down policy

If you believe that this document breaches copyright please contact librarypure@kcl.ac.uk providing details, and we will remove access to the work immediately and investigate your claim.

Characterisation of human induced pluripotent stem cells in 3D artificial microenvironment using high content analysis

Haneen Sohail Alsehli

Thesis submitted for the degree of Doctor of Philosophy

First Supervisor: Dr Davide Danovi
Second Supervisor: Dr Eileen Gentleman



Centre for Gene Therapy & Regenerative Medicine

King's College London

2023

To Mother and Father

Whose affection, love, encouragement, and prays day and
night make me able to reach this point of success.

ASSOCIATED MANUSCRIPTS

Published

Alsehli H, Mosis F, Thompson C, Hamrud E, Wiseman E, Gentleman E, Danovi D. “An integrated pipeline for high-throughput screening and profiling of spheroids using simple live image analysis of frame to frame variations”. *Methods*. 2021 Jun;190:33-43. [doi: 10.1016/j.ymeth.2020.05.017](https://doi.org/10.1016/j.ymeth.2020.05.017).

Chapter 3 includes this publication without breaking the publisher’s copyright.

Submitted Manuscript (under review)

This manuscript was written based on Chapters 4 and 5.

Haneen S. Alsehli, Errin Roy, Thomas Williams, Alicja Kuziola, Yunzhe Guo, Jeremy Green, Eileen Gentleman, Davide Danovi. “Morphogen-driven human iPS differentiation in 3D models of gastrulation *in vitro* is precluded by physical confinement”.

ACKNOWLEDGEMENTS

Firstly, I would like to thank my supervisors, Dr Davide Danovi and Dr Eileen Gentleman, for allowing me to be part of their groups and providing guidance and support from day one. I consider myself lucky to have such wonderful supervisors; thank you both for your inspiration and encouragement in all times, good and bad. I have been learning a lot with you, which has shaped me into who I am now. I am grateful for having such great supervisors; you are the best role models. Thank you for making my PhD journey so enjoyable. Second, I am so thankful to Dr Davide Danovi for being so supportive and always available whenever needed for the project during the COVID-19 pandemic. It touched my heart how you cared and supported in difficult times, and I could fill pages writing about that.

I am also thankful to Prof Fiona Watt for her time and feedback on my project frequently. Special thanks to Prof Jeremy Green for providing insight, knowledge, and feedback on my manuscript. I want to thank my thesis committee members, Prof Ulrike Eggert, Dr Ciro Chiappini, and Dr Rocio Sancho, for the time and expertise that they provided.

I thank Prof Susan Kimber and Dr Anthony Callanan for agreeing to read and examine my thesis. Thank you for your time, and the chance to discuss my project with you.

Special thanks to Dr Mukul Tewary, Dr Alice Vickers, and James Williams for their help to establish my tissue culture experiments. I would also thank members of the Gentlemen's group, former and present, Dr Michael Norman, Dr Geraldine Jowett, and Suzie Lust, for their help and training on hydrogel formation; special thanks to Yunzhe Guo, and Kuziola Alicja for their contribution to performing the measurements to characterise the PEG-peptide hydrogel. I am so grateful to Dr Fuad Mosis, and Errin Roy for their incredible help to establish the image analysis pipelines. Many thanks to the Stem Cell Hotel Team, Dr Lazaros Fotopoulos, Thomas Willams (Tom), and former member Erika Wiseman for all

their support in the imaging facilities and analysis. I want to thank all the management, technical, and public engagement members for all their hard work in helping us.

It has been a privilege to be a member of the CSCRM/ CGTRM (“new name” during my PhD). I am thankful for being in such a place with a great environment of productivity and fun, not to mention the amazing view from the 28th floor that I will miss. I want to thank my “neighbours” Inês Tomas, Vassia Salameti, Tom (again), Mahedah Rehman, also Georgina Goss, who always come to join! For creating so much fun. Special thanks to my friend Victoria Tsang at the centre and Danovi group, “the creative artist,” for all the time we spent together and for supporting each other.

I am fortunate to have my friends Alaa and Reem (from SA) here in the UK; thank you both for your support and the warm welcome whenever I feel stressed and visit you in Cardiff. Thank you, Lubna, for being such a good friend in many good and bad moments, even though we are miles apart.

I am grateful to my mentor and previous director, Prof Mamdooh Gari, whom I dreamt of being successful one day, for his encouragement and inspiration, just like a (Father) to me—special thanks to Dr Mohammed Abuzinadah for his support and helpful advice during my PhD journey.

I gratefully acknowledge the Royal Embassy of Saudi Arabia Cultural Bureau and the Ministry of Education for the scholarship and PhD funding.

Finally, I am thankful beyond words to my family; this PhD would not have happened without their financial and emotional support. Thank you, Mom and Dad, for the tremendous encouragement and care, epically my Mom, for all the moments every day on a video call. I have nothing to say but love you so much, my brothers Hosam, Hazem, Ammar, and my sisters Maram and Yara.

COVID Impact Statement

The COVID-19 restrictions disrupted my PhD research in several ways.

- The laboratory was closed for four months during the first national lockdown in 2020, and as I couldn't perform experiments, I went back home from May 2020 until the end of September 2020. I was stuck in Saudi Arabia due to international flight restrictions. These circumstances kept me away from the laboratory for almost eight months.
- When I returned during the second national lockdown, access to the lab was limited under shift work. During that time, I could work in a partial capacity and resourced to prioritise finishing experimental assays on one cell line to obtain complete readouts.
- The live imaging device (JuLiStage) was out of operation for about six months, which resulted in a major technical issue. Other devices like Operetta CLS and MARK1 were incompatible with the V-bottom plates. This issue prevented me from screening more cell lines as planned earlier in my PhD aims.

Table of Abbreviations

A-P	Anterior posterior
AMD	Age-related macular degeneration
AVE	Anterior visceral endoderm
BRA	Bone morphogenic protein 4
C-MYC	C-MYC proto-oncogene
CRISPR	Clustered regularly interspaced short palindromic repeats
DAPI	4',6-diamidino-2-phenylindole
Deg-PEG	degradable PEG hydrogel (75% PEG-4Acr)
DMEM	Dulbecco's modified eagle medium
E-CAD	E-cadherin
E8	Essential 8
EBs	Embryoid bodies
ECM	Extracellular matrix
EMT	Epithelial-to-mesenchymal transition
EOMES	Eomesodermin
ETS	Extraembryonic trophoctoderm stem cells
ExE	Extra-embryonic ectoderm tissue
FGF	Fibroblast growth factor
G' prime	Storage modulus
GWAS	Genome wide association study
HCA	High-content images
HEPES	4-(2-hydroxyethyl)-1-piperazineethanesulfonic acid
hESC	Human embryonic stem cells
hiPSC	Human induced pluripotent stem cells
HipSci	Human induced pluripotent stem cell initiative
HLA	Human leukocyte antigen
HTS	High-throughput screening
ICM	Inner cell mass
IKBKAP	I- κ -B kinase complex-associated protein
KLF4	Kruppel-like factor 4
KSR	Knockout serum replacement
mESC	Mouse embryonic stem cells
MMPs	Matrix metalloproteinases
N-CAD	N- cadherin
non-degPEG	Non degradable PEG hydrogel (100% PEG-4VS)
OCT4	Octamer-binding transcription factor 4
PBMCs	Peripheral blood mononuclear cells
PBS	Phosphate-buffered saline

PDMS	Poly (dimethylsiloxane)
PE	Primitive endoderm
PEG	Poly (ethylene glycol)
PEG-4Acr	Poly (ethylene glycol) 4 arms acrylate
PEG-4VS	Poly (ethylene glycol) 4 arms vinyl sulfone
PEG-NPC	Poly (ethylene glycol) Nitrophenyl Carbonate
PGCs	Primordial germ cells
PI	Positional information
PLL-g-PEG	Poly(L-lysine)-grafted-poly (ethylene glycol)
PSCs	Pluripotent stem cells
RD	Reaction-diffusion
RGD	Aginylglycylaspartic (Arg-Gly-Asp)
ROCKi	Rho-associated protein kinase inhibitor
ROIs	Regions of interest
ROS	Reactive oxygen species
RPE	Retinal pigment epithelial
RT	Room temperature
SD	Standard deviation
SMAD	Mothers against decapentaplegic homolog
SMN	Spinal muscular atrophy
SOX17	Sex determining region Y-box transcription factor 17
SOX2	Sex determining region Y-box transcription factor 2
TE	Trophectoderm
TGF-β	Transforming growth factor beta
VE	Visceral endoderm
WNT	Wingless-related integration site
YAP	Yes-associated protein 1

LAY SUMMARY

A clearer understanding of the human developmental process from fertilised egg to organogenesis has started in recent years to translate into applications for regenerative medicine. The first steps in early embryogenesis, cell divisions of the fertilised egg, leads to a spherical sphere-like formation called blastula, which develops as a cavity and is referred to as a blastocyst. This spherical globe is surrounded by uterine tissue that provides mechanical forces and strains affecting the gastrulation process, where the three germ layers (ectoderm, mesoderm, and endoderm) arise to form the embryo. The dynamic interplay between mechanics and biochemical signals during morphogenesis of early development in human is poorly understood. Since their discovery, pluripotent stem cells have become a valuable tool to mimic early embryogenesis *in vitro* due to their ability to self-renewal and give rise to all cell types of an embryo. Approaches such as 3D culture and synthetic biomaterial and hydrogels enabled to create models attempting to mirror the native extracellular matrix (ECM) microenvironment. Progress in imaging and computation has enabled detailed and quantitative readouts of cell biology. In this project, we bring together stem cell biology, high-content imaging, and hydrogel-based technology to explore morphogenesis events and cell fate organisation in a 3D model.

ABSTRACT

During gastrulation, the pluripotent stem cells of the epiblast differentiate, ultimately shaping the embryo's body plan. This process is tightly associated with extensive cellular movements that induce breaking symmetry to form anterior-posterior axial elongation giving rise to the three germ layers. Morphogenesis events and lineage specifications of the tri-germ layers are regulated by distinctive interactions, including cell-cell contacts that transmit biochemical signals and cell-ECM interplay with physical forces exerted from the extra-embryonic environment. Nonetheless whether tissue rearrangements are regulated mechanically (tissue environment) or biochemically (cellular response) is poorly understood. Cultures of human induced pluripotent stem cells (hiPSC) offer unprecedented scope to profile and screen conditions affecting cell fate decisions and self-organisation during early embryonic development. The impact of biochemical signalling (BMP4, NODAL, and WNT) in 2D micropattern systems has been well-established, which recapitulates the three germ layers patterning *in vivo*.

I have proposed here a 3D hiPSC platform to induce gastrulation upon BMP4 treatment. My aim is to investigate how biochemical cues and physical confinement separately influence morphogenesis and differentiation. To investigate the biochemical effect, I used BMP4 to trigger symmetry breaking and elongation of hiPSC spheroids in suspension culture. Having different medium conditions representing self-renewing (E8 medium) and differentiation (KSR BMP4) and their controls (E8 BMP4 and KSR) gave rise to distinct morphologies in suspension. I also postulated that morphogenesis and changes in shape are regulated by cellular tension in response to biochemical cues. Hence, I hypothesised that PEG-peptide hydrogel systems inhibit elongation and thus enable us to interrogate if physical confinement affects not just morphogenesis but also cell fate specification. High content analysis (HCA) was used as readouts obtained from live imaging to observe morphological changes and immunostaining techniques to detect the expression of pluripotency and differentiation markers. Our approach enables us to investigate changes in shape and patterning of the three germ layers using hiPSC and sheds light on the interplay between chemical signals and physical forces.

TABLE OF CONTENTS

ASSOCIATED MANUSCRIPTS.....	III
ACKNOWLEDGEMENTS	IV
COVID IMPACT STATEMENT	VI
TABLE OF ABBREVIATIONS	VII
LAY SUMMARY	IX
ABSTRACT	X
1 GENERAL INTRODUCTION	16
1.1 GASTRULATION	16
1.1.1 <i>Biochemical signals</i>	19
1.1.2 <i>Hippo pathway and YAP signalling</i>	20
1.2 PLURIPOTENT STEM CELLS	22
1.2.1 <i>Modelling development and its importance</i>	27
1.2.2 <i>Models of gastrulation in vitro</i>	29
1.2.2.1 2D systems	29
1.2.2.2 3D systems	30
1.2.3 <i>Modelling human diseases and drug discovery</i>	32
1.2.4 <i>Cell therapy</i>	34
1.2.5 <i>HipSci</i>	35
1.3 THE ROLE OF THE TISSUE MICROENVIRONMENT.....	38
1.3.1 <i>ECM and cell interactions</i>	38
1.3.2 <i>Bioengineering approaches</i>	40
1.3.2.1 Synthetic hydrogel.....	40
1.4 HIGH-CONTENT IMAGE ANALYSIS	42
1.5 AIMS & HYPOTHESIS	44
2 MATERIALS AND METHODS	46
2.1 CELL CULTURE.....	46
2.1.1 <i>hiPSC cells</i>	46
2.1.2 <i>hiPSC thawing and culture</i>	46
2.1.3 <i>hiPSC maintenance</i>	47
2.1.4 <i>hiPSC freezing</i>	47
2.2 SPHEROIDS FORMATION AND 3D CULTURE	47

2.2.1	<i>Spheroids derivation from hiPSC</i>	47
2.2.2	<i>Gastrulation-like induction of hiPSC spheroids</i>	48
2.3	PEG HYDROGELS	48
2.3.1	<i>PEG-peptide conjugation and purification</i>	48
2.3.2	<i>PEG-peptide hydrogel formation</i>	50
2.3.3	<i>Rheological measurements of hydrogels</i>	50
2.3.4	<i>Tryptophan release quantification</i>	51
2.3.5	<i>hiPSC spheroids encapsulation in PEG-peptide hydrogel</i>	51
2.4	IMMUNOFLUORESCENCE LABELLING	52
2.4.1	<i>Spheroids in suspension immunostaining</i>	52
2.4.2	<i>Cell proliferation assay</i>	53
2.4.3	<i>Embedded spheroids in PEG-peptide hydrogel immunostaining</i>	53
2.4.4	<i>Cell viability assay</i>	54
2.5	IMAGING AND QUANTIFICATION	56
2.5.1	<i>Live cell imaging</i>	56
2.5.1.1	<i>Image analysis for time-lapse imaging of spheroids in suspension</i>	56
2.5.1.2	<i>Computational neural networks for spheroids in suspension clustering</i>	56
2.5.2	<i>Confocal microscopy</i>	57
2.5.2.1	<i>Imaging of spheroids in suspension</i>	57
2.5.2.2	<i>Imaging of embedded spheroids in PEG-peptide hydrogel</i>	57
2.5.2.3	<i>Image analysis</i>	57
2.5.2.4	<i>Icy analysis pipeline</i>	58
2.6	STATISTICAL ANALYSIS	59
3	DISTINCT MORPHOLOGY IN 3D GASTRULATION-LIKE MODELS UNDER DIVERSE CULTURE	
	CONDITIONS	60
3.1	INTRODUCTION	60
3.2	BMP4 SIGNALLING INDUCES AXIAL ELONGATION IN 3D GASTRULATION-LIKE MODELS	61
3.3	HIGH-CONTENT IMAGE ANALYSIS	63
3.3.1	<i>Quantification of 3D hiPSC distinct variations under diverse culture conditions based on endpoint images</i>	63
3.3.2	<i>An integrated pipeline for high-throughput screening and profiling of spheroids using simple live image analysis of frame to frame variations</i>	65
3.4	DISCUSSION	77
4	DISTINCT EXPRESSION OF LINEAGE DIFFERENTIATION MARKERS IN 3D GASTRULATION- LIKE	
	MODELS.....	80
4.1	INTRODUCTION	80

4.2	MORPHOGENESIS IN hiPSC 3D GASTRULATION-LIKE MODEL DRIVES THREE GERM LAYERS SPECIFICATION POST-BMP4 TREATMENT.....	81
4.3	BIOCHEMICAL CUES OF DIVERSE MEDIUM CONDITIONS REGULATE MORPHOGENESIS VIA PROLIFERATION AND CELLULAR TENSION IN 3D SPHEROIDS.....	90
4.3.1	<i>The addition of BMP4 and KSR medium reveals distinct cell proliferation phenotype drives morphological changes in 3D spheroids.</i>	91
4.3.2	<i>Cellular tension drives elongation and budding formation under differentiation conditions</i>	93
4.4	DISCUSSION	96
5	PHYSICAL CONFINEMENT INFLUENCES MORPHOLOGICAL CHANGES AND EXPRESSION OF LINEAGE SPECIFICATION MARKERS	102
5.1	INTRODUCTION	102
5.2	PEG-PEPTIDE HYDROGEL MODULATION RESULTED IN SOFTER GELS	103
5.3	PEG-PEPTIDE HYDROGEL ENCAPSULATION PREVENTS MORPHOLOGICAL CHANGES	107
5.4	SOFT PEG-PEPTIDE HYDROGELS PROMOTE CELL VIABILITY.....	109
5.5	PHYSICAL CONFINEMENT DISTURBS THE EMERGENCE OF LINEAGES SPECIFICATIONS	112
5.6	MODULATING PEG-PEPTIDE DEGRADABILITY PROMOTES SOX17 EXPRESSION.....	114
5.7	DISCUSSION	119
6	DISCUSSION & FUTURE DIRECTIONS.....	124
6.1	DISCUSSION	124
6.1.1	<i>Strengths.....</i>	127
6.1.2	<i>Limitations.....</i>	129
6.2	FUTURE DIRECTIONS.....	132
6.2.1	<i>Genetic variation of hiPSC</i>	132
6.2.2	<i>Time-course of germ layer differentiation.....</i>	133
6.2.3	<i>Transcriptomics characterisation</i>	134
6.2.4	<i>PEG-peptide hydrogel modification.....</i>	135
	APPENDIX 1	137
	APPENDIX 2	138
	REFERENCE LIST	139

LIST OF FIGURES

FIGURE 1.1 EARLY EMBRYONIC DEVELOPMENT IN VIVO.....	17
FIGURE 1.2 REACTION-DIFFUSION AND POSITIONAL INFORMATION MODELS REGULATE CELL FATE PATTERNING IN EMBRYO DEVELOPMENT.	18
FIGURE 1.3 SIGNALLING DYNAMIC PATHWAY THAT REGULATES GASTRULATION EVENTS.....	22
FIGURE 1.4 GENERATING hiPSC FROM ADULT SOMATIC CELLS.....	25
FIGURE 1.5 APPLICATIONS OF hiPSC.	26
FIGURE 1.6 THE IDENTIFICATION OF PHENOTYPE OUTLIERS IN hiPSC THAT CORRELATE WITH GENETIC VARIATIONS USING hiPSci CELL LINES.	37
FIGURE 1.7 THE ROLE OF MICROENVIRONMENT IN CELL BEHAVIOUR AND DIFFERENTIATION.....	39
FIGURE 2.1 SCHEMATIC OF EXPERIMENTAL WORKFLOW.	52
FIGURE 2.2 OVERVIEW OF F-ACTIN ANALYSIS PIPELINE.	59
FIGURE 3.1 hiPSC FORMING A DISTINCT MORPHOLOGY UNDER DIVERSE MEDIUM CONDITIONS.....	62
FIGURE 3.2 QUANTIFICATION OF MORPHOLOGICAL CHANGES.....	64
FIGURE 4.1 BMP4 SIGNALLING INDUCES SOX17 SPECIFICATION IN 3D MODEL OF GASTRULATION.....	84
FIGURE 4.2 TRACKING AXIAL ELONGATION VIA LIVE IMAGING DURING TIME POINTS.....	85
FIGURE 4.3 THE EMERGENCE OF MESODERMAL MARKERS BRA AND EOMES IN 3D MODEL OF GASTRULATION.....	87
FIGURE 4.4 THE EXPRESSION OF SOX2 MARKER IN 3D MODEL OF GASTRULATION.	90
FIGURE 4.5 DISTINCT PROLIFERATION PHENOTYPE IN RESPONSE TO BIOCHEMICAL CUES.....	92
FIGURE 4.6 F-ACTIN NETWORK ORIENTATION DRIVES ELONGATION IN THE 3D MODELS.	94
FIGURE 4.7 YAP TRANSLOCATION INFLUENCES MORPHOGENESIS IN hiPSC.....	95
FIGURE 5.1 PEG-PEPTIDE HYDROGEL NETWORK FABRICATION.....	105
FIGURE 5.2 PEG-PEPTIDE HYDROGELS CHARACTERISATION.....	106
FIGURE 5.3 hiPSC ENCAPSULATION IN PEG-PEPTIDE HYDROGEL PREVENTS MORPHOLOGICAL CHANGES.	108
FIGURE 5.4 CELL VIABILITY IN DIFFERENT HYDROGEL CONDITIONS.	111
FIGURE 5.5 hiPSC SPHEROIDS ENCAPSULATED IN NON-DEGPEG AND THE EMERGENCE OF SOX17 EXPRESSION.	114
FIGURE 5.6 hiPSC SPHEROIDS POST-ENCAPSULATION IN 75%PEG-4ACR AND SOX17 EXPRESSION.	117
FIGURE 5.7 DIVERSE EXPRESSION OF OCT4 AND SOX17 MARKERS IN NON-DEG PEG AND DEG-PEG HYDROGELS.	118

LIST OF TABLES

TABLE 2.1. ANTIBODIES USED FOR 3D SPHEROIDS IMMUNOSTAINING.....55

1 GENERAL INTRODUCTION

1.1 *Gastrulation*

In early human development, fertilised egg undergoes a series of cell fate divisions that lead to the formation of the blastocyst, consisting of an external layer trophectoderm (TE) and the inner cell mass (ICM). In the late blastocyst stage, the ICM give rise to the epiblast cells and hypoblast: a layer of cells known as primitive endoderm (PE) (Figure 1.1 A). Gastrulation occurs when the pluripotent cells of the epiblast segregate and gives rise to the three germ layers (ectoderm, mesoderm, and endoderm), ultimately forming the human embryo (Figure 1.3 B) (Tam and Behringer, 1997, Wolpert et al., 2015, Rossant and Tam, 2022). This complex process involves highly dynamic events resulting in changes in cell shape and cellular rearrangement (Kim et al., 2017, Hashmi et al., 2022).

The onset of the process is marked by the changes in embryo morphology through the formation of the primitive streak, which is indicated by symmetry breaking to initiate anterior-posterior (A-P) axis elongation. One of the crucial steps during gastrulation is that the epiblast cells undergo epithelial-mesenchymal transition (EMT). The cells collectively migrate and ingress toward the primitive streak to facilitate the formation of the tri-lineages of germ layers (Tam et al., 1997, Simunovic et al., 2019). During the EMT process, the epithelial layer of the epiblast loses its apical-basal polarity and cell adhesions to facilitate cellular movement (Kim et al., 2017). Hence, the epithelial marker E-cadherin (E-CAD) undergoes downregulation which reduces adhesion molecules between cells, thus increasing cell motility and switching to N-cadherin (N-CAD), the characteristic of the mesenchyme phenotype. These mesenchymal features allow for cytoskeleton remodelling to promote differentiation during gastrulation (Kim et al., 2018a, Nakaya and Sheng, 2008, Thiery et al., 2009).

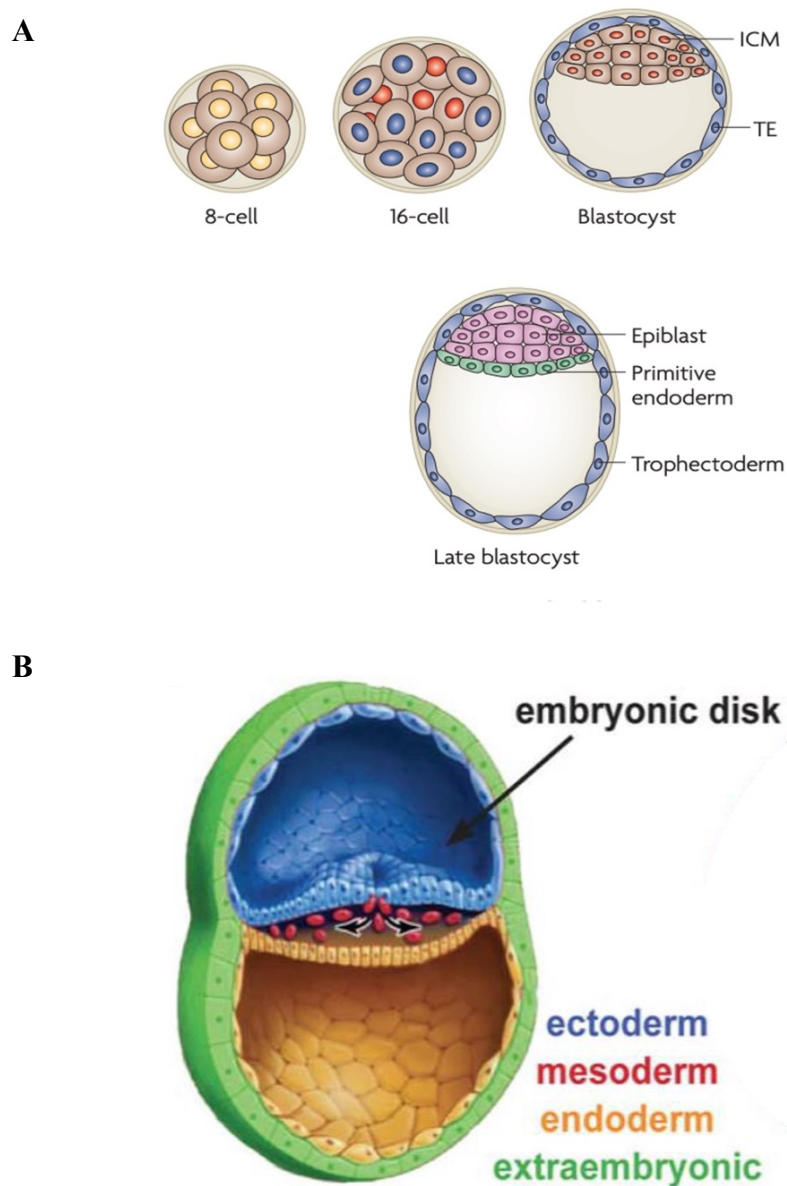


Figure 1.1 Early embryonic development *in vivo*.

A) Post-fertilisation cells undergo series of cell division to develop the blastocyst a hollow ball of cells that consists of ICM, PE and TE. **B)** later in development the ICM in the blastocyst gives rise to the three germ layers (ectoderm, mesoderm, and endoderm), whereas the TE gives rise to the extra-embryonic ectoderm tissue (ExE) tissue. Figures adapted from (Arnold and Robertson, 2009, Heemskerk and Warmflash, 2016).

Models of the role of chemical morphogen signals in cell fate control during development were introduced by Alan Turing (Reaction Diffusion, RD, Turing, 1952) and Lewis Wolpert (Positional Information, PI, Wolpert et al., 2015). The RD model (the Turing system) is described as an activator that can regulate its expression and an inhibitor, which is upregulated and diffuses faster than the activator, thereby creating self-organised gradients of pathway signalling (Figure 1.2 A). In contrast, the PI model (Wolpert's system) suggests that the early asymmetry in the embryo, including spatial polarisation of the signalling cascade, controls the pattern formation of cell fate (Figure 1.2 B). The diffusible signals are distributed asymmetrically and expose cells to distinct concentrations which determine cell fate decisions based on concentration manner (Turing, 1952, Green and Sharpe, 2015, Wolpert et al., 2015).

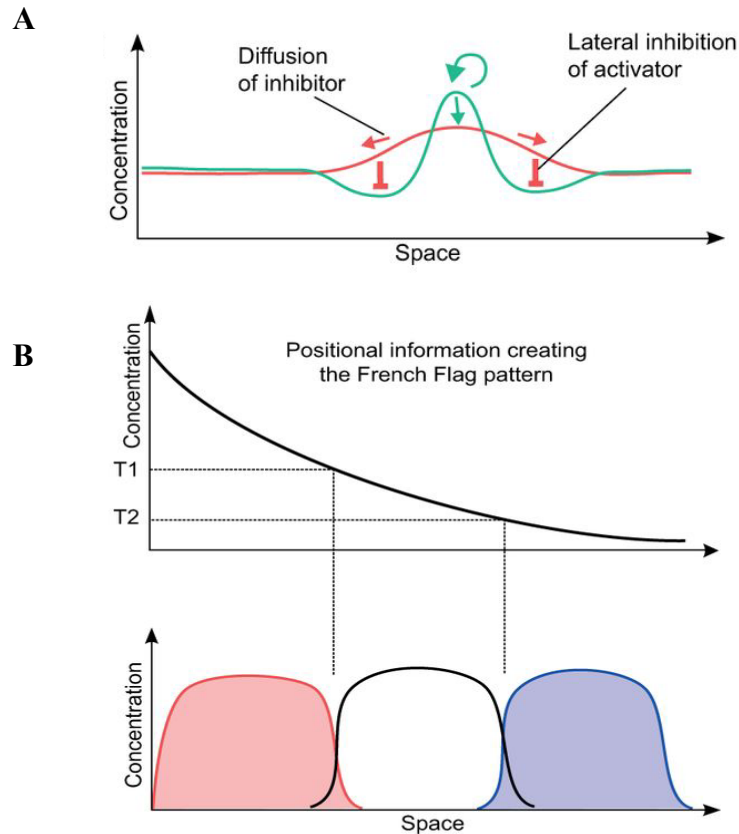


Figure 1.2 Reaction-diffusion and positional information models regulate cell fate patterning in embryo development.

A) In the RD system, a homogenous distribution of morphogen cues reacts in an activator-inhibitor manner that triggers its own expression (green) and the expression of its inhibitors (red). A positive feedback diffusion from the activator maintains the stability of its high levels, while the higher diffusion rate of the inhibitor results in lateral inhibition

of the activator. This creates different zones of substrate distribution which regulate cell fate patterning. **B)** The PI model defines the concept of morphogens gradient signal, in which the concentration of molecule determines cell fate. Adapted from (Green and Sharpe, 2015).

1.1.1 Biochemical signals

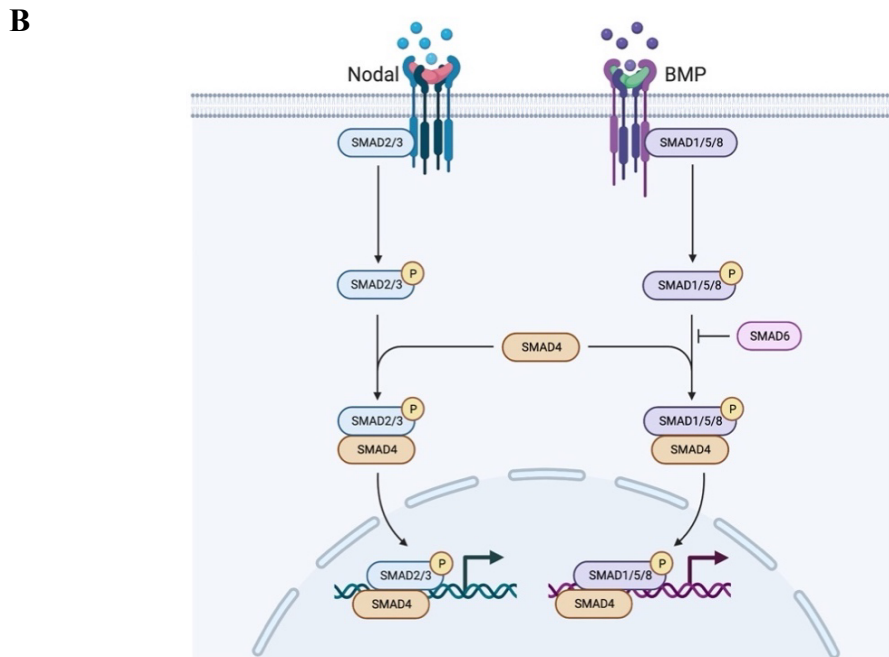
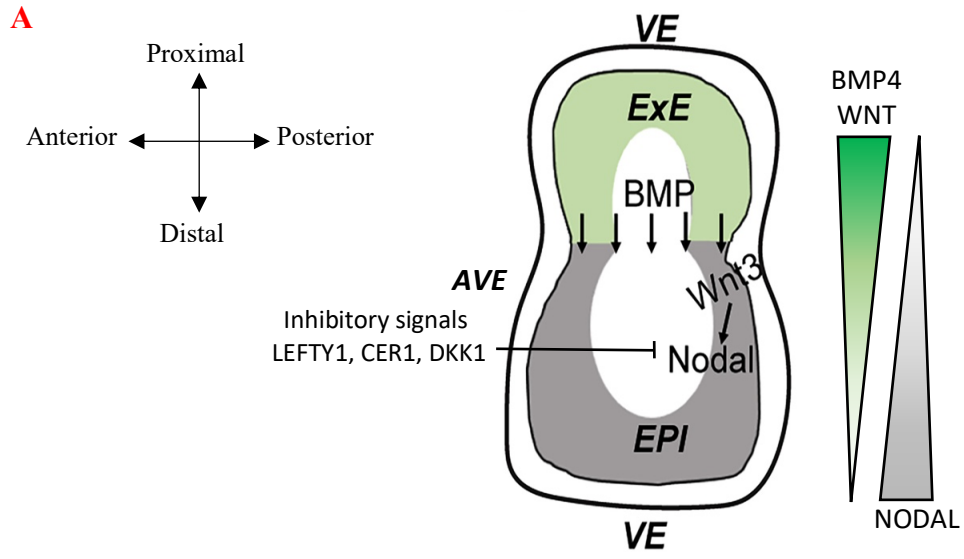
Decades of biochemical studies in mouse embryos revealed the dynamic morphogen pathways essential in the mammalian gastrulation process (Arnold and Robertson, 2009, Green and Smith, 1991). Therefore, recent studies of human stem cell models provide insights into signalling pathways that lead to axial elongation and germ layer specifications (Camacho-Aguilar and Warmflash, 2020). The signalling cascades include fibroblast growth factor (FGF) families, WNT and members of the transforming growth factor Beta superfamily (TGF- β) such as NODAL and bone morphogenetic protein (BMP) (Camacho-Aguilar and Warmflash, 2020, Chhabra et al., 2019).

The signalling pathway in the early mouse embryo during *in vivo* gastrulation is well established. TE, the extra-embryonic ectoderm tissue (ExE), initiates BMP4 secretion, and the signalling activity increases through a positive feedback loop (Figure 1.3 A). Thus, the BMP signal induces WNT expression in the epiblast and visceral endoderm (VE), which activates NODAL signalling, and subsequently, NODAL stimulates BMP4 signalling in return (Ben-Haim et al., 2006b, Chhabra et al., 2019). In parallel, BMP, WNT and NODAL antagonists (LEFTY1, CER1 and DKK1) are expressed from the anterior visceral endoderm (AVE) and restrict the primitive streak (the site of gastrulation) to the posterior domain of the embryo. The migrated epiblast cells, through the EMT process, are exposed to NODAL signalling to trigger the expression of mesoderm marker Brachyury (BRA) which then forms mesoderm and definitive endoderm (Rivera-Pérez and Magnuson, 2005, Shahbazi and Zernicka-Goetz, 2018, Chhabra et al., 2019). Other studies showed that BMP signals induce primordial germ cells (PGCs) specification in posterior epiblast cells (Leitch et al., 2013, Irie et al., 2015). In contrast, the anterior epiblast induces the formation of ectodermal cells where WNT and NODAL signals are inhibited by the AVE tissues (Perea-Gomez et al., 2002). The interplay between biochemical signals creates gradients along the A-P domain that are thought to control gastrulation in a concentration-dependent manner and specify the germ

layers (Arnold and Robertson, 2009, Siggia and Warmflash, 2018). Several studies demonstrated that the signalling cascade during gastrulation is regulated through ligands such as BMP4 and NODAL signals that transduce SMAD1/5/8 and SMAD 2/3, respectively, WNT signals activate β -catenin to induce germ layers differentiation (Figure 1.3 B-C) (Chhabra et al., 2019, Camacho-Aguilar and Warmflash, 2020, Nemashkalo et al., 2017). However, FGF signalling transduces MEK, which regulate cell proliferation, migration, and survival during gastrulation event (Figure 1.4 C) (Camacho-Aguilar and Warmflash, 2020, Oki et al., 2010).

1.1.2 Hippo pathway and YAP signalling

The hippo pathway /YES-associated protein (YAP) function as mechanotransduction sensor that perceives mechanical stimuli and transmits these signals to regulate cell proliferation, fate decisions, and organ development. In response to biochemical cues, mechanical tension is generated between cell-ECM and cell-cell; the YAP activity mediates these signals (Heng et al., 2021, Cai et al., 2021). The mechanosensing response is initiated at cell surfaces via integrins which trigger the activation of YAP signalling and promote its localisation in the cytoplasm (inactive) and translocation to the nucleus (active). Hence, this prompt changes at the protein activity level, localisation, and gene expression to determine cell fate (Cai et al., 2021). YAP signalling has been reported to contribute to cell rearrangement and morphogenesis during development. In addition, the YAP protein stimulates genes encoding expression for cytoskeletal regulators such as actin networks, focal adhesions, and ECM molecules to facilitate morphogenesis. During early gastrulation phases in mouse embryos, YAP protein was shown to be active in the migratory cells. This suggested that YAP protein is necessary to direct cell migration and initiate axial formation during gastrulation (Sousa-Ortega et al., 2023).



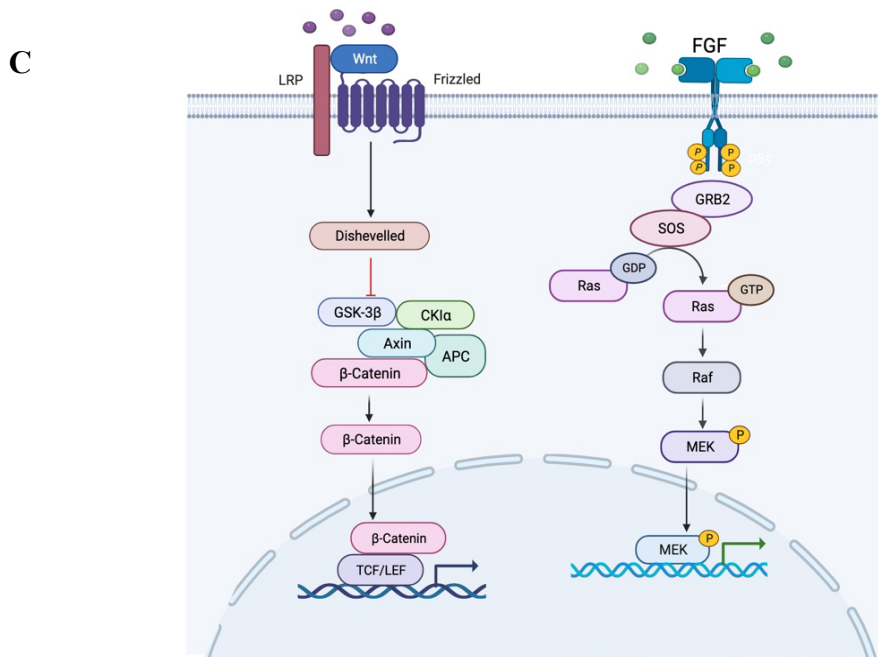


Figure 1.3 Signalling dynamic pathway that regulates gastrulation events.

A) Schematic of signalling cascade flow in a mouse embryo (E5.5, E6.5), BMP signals from the ExE activate WNT in the epiblast (EPI) which resulted in NODAL activation and initiate the primitive streak during gastrulation, thus BMP4, WNT, and NODAL are antagonised by LEFTY1, CER1 and DKK1 secreted from AVE. **B)** NODAL and BMP ligands members of the TGF- β family, activates pSMAD2/3, and pSMAD1/5/8. **C)** WNT receptor eventually induces β -catenin, and FGF activates MEK. The signalling pathways direct cell lineages specification. Figures adapted from (Liu and Warmflash, 2021) and signalling pathways created by BioRender.com

1.2 *Pluripotent stem cells*

Defining features of stem cells are self-renewal (the capacity to replicate into identical cells) and differentiation (to give rise to cells performing a function). The differentiation potential is referred to as ‘potency’ (Smith, 2006, Martello and Smith, 2014). Pluripotent stem cells (PSCs) have the potential to maintain self-renewal by producing identical daughter cells and undergo differentiation generating, in principle, all somatic cell lineages of the embryonic germ layers (ectoderm, mesoderm, and endoderm) (Figure 1.4 A). These cells offer an unprecedented tool for human disease modelling and drug screening. Great insights into cell fate decisions, signalling pathways, disease

mechanisms and fundamental aspects of early development can be thus obtained *in vitro* (Shi et al., 2017, Rowe and Daley, 2019, Niakan et al., 2012).

Human PSCs are typically obtained from two main sources: human embryonic stem cells (hESC) or human induced pluripotent stem cells (hiPSC). A breakthrough happened as hESC were successfully isolated in 1998 from the ICM of the human blastocyst (Thomson et al., 1998, Reubinoff et al., 2000). However, using hESC raised some major issues: first, ethical concerns because of their origin from human embryos; second, their immunogenicity response, restricting use for cell-based therapies (Sugarman, 2008, Niakan et al., 2012, Parr et al., 2017). Since then, much progress has been made in the stem cells field towards a readily source of human PSCs for the purpose of regenerative medicine (Figure 1.4 B) (Shi et al., 2017, Parr et al., 2017). In 2007, Yamanaka and colleagues reported that hiPSC could be produced by reprogramming differentiated adult human somatic cells into a pluripotent state using four transcription factors KLF4, SOX2, OCT4, and C-MYC (Takahashi and Yamanaka, 2006, Takahashi et al., 2007). Since the debate of whether hiPSC differentiation is as efficient as hESC and whether differences exist at the molecular level has been a focal point of discussion (Chin et al., 2009, Yamanaka, 2012). Few studies reported that several genes are expressed in hESC and not in hiPSC; changes in DNA methylation suggest that hiPSC could represent another subtype of pluripotent cells (Chin et al., 2009, Deng et al., 2009). Later, other groups analysed a wide range of hiPSC and hESC lines and demonstrated overlapping in gene expression between the two types of cells (Guenther et al., 2010, Newman and Cooper, 2010, Bock et al., 2011). These findings determined that these cells are relatively consistent (Bock et al., 2011, Yamanaka, 2012). Since then, because of the benefits, the reprogramming technology provided hiPSC lines derived from adult donors that most likely share the same, including morphology, and gene expression of hESC during culture *in vitro* (Parr et al., 2017, Yamanaka, 2012).

hiPSC can be generated from fibroblast cells via skin punch biopsies or other adult somatic cells such as peripheral blood mononuclear cells (PBMCs) and keratinocytes (Takahashi et al., 2007, Silva et al., 2015, Aasen et al., 2008). Several protocols have described the reprogramming process to produce hiPSC lines using integrating and non-integrating vectors or free DNA methods (Silva et al., 2015, Schlaeger et al., 2015). The

integrating techniques widely used to generate hiPSC are based on retroviral vectors, which incorporate transcription factors into the host genome to activate the pluripotency genes (González et al., 2011, Takahashi and Yamanaka, 2006). It has been reported that this method can lead to mutagenesis and residual expression of reprogramming factors in hiPSC and their derivatives, thereby limiting their use for clinical applications (Kang et al., 2015, Schlaeger et al., 2015). Improvement in reprogramming technology to reduce footprint, i.e., avoiding the persistence of exogenous genetic materials in the host cell, has been effective. Non-integrating methods include RNA virus such as adenovirus gene delivery (Zhou and Freed, 2009), Sendai virus (Fusaki et al., 2009), as well as non-viral methods such as episomal vectors (Okita et al., 2011), synthetic mRNA (Warren et al., 2010), and piggyBac transposons (Kaji et al., 2009). Many of these non-integrating or DNA-free approaches to generate hiPSC showed low reprogramming proficiency, excluding the Sendai virus and episomal vectors (Schlaeger et al., 2015). Using the two technologies resulted in extremely reliable reprogramming efficiency and is well-suited for manufacturing or clinical use compared to all integrated and non-integrated methods (Schlaeger et al., 2015, Chen et al., 2011, Yu et al., 2011).

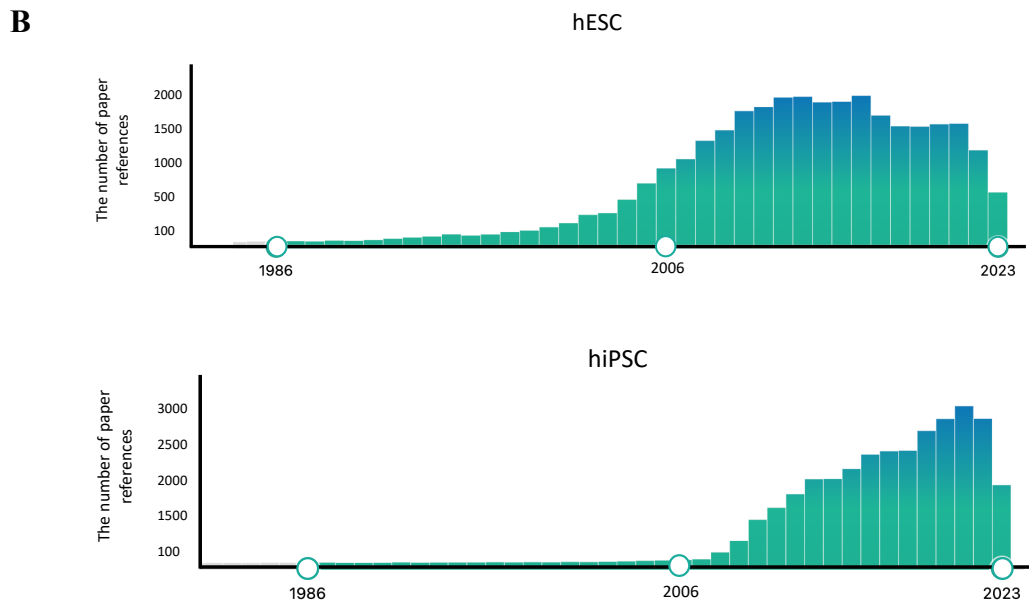
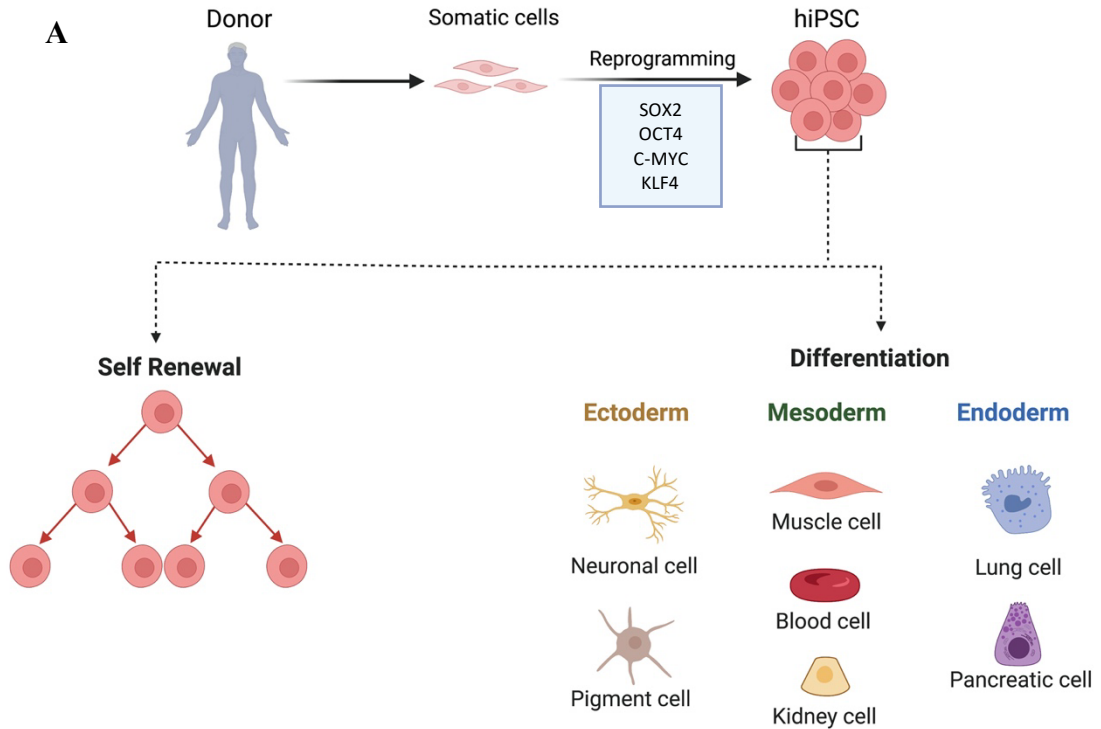


Figure 1.4 Generating hiPSC from adult somatic cells.

A) Adult somatic cells can be turned into an embryonic-like state via a reprogramming technique using the Yamanaka’s factors (SOX2, OCT4, C-MYC, KLF4). Under defined medium conditions the pluripotent cells maintain self-renewal or undergo differentiation into the three germ layers, which give rise to all cell types in the body. **B)** Graphs representing the volume of published research using hESC (top) versus hiPSC (bottom). The use of hiPSC has been increased recently in comparison to hESC. Figure was created with BioRender.com, and graphs adapted from <https://pubmed.ncbi.nlm.nih.gov/>.

The remarkable progress in cell reprogramming technology to produce hiPSC lines over the past years has allowed scientists to develop strategies for modelling human disease and drug screening (Figure 1.5) (Wu and Hochedlinger, 2011). Several studies have described differentiation protocols representing specific human diseases or tissue development often guided by the signalling molecules driving *in vivo* differentiation (Csobonyeiova et al., 2015, Tabar and Studer, 2014). Using *in vitro* hiPSC approaches provides significant advantages compared to some animal models to gain insight into the inheritance and rare human diseases (Saito-Diaz and Zeltner, 2019b, Rowe and Daley, 2019). On the other hand, the reprogramming technology that leads to hiPSC offers great potential for cell therapy applications.

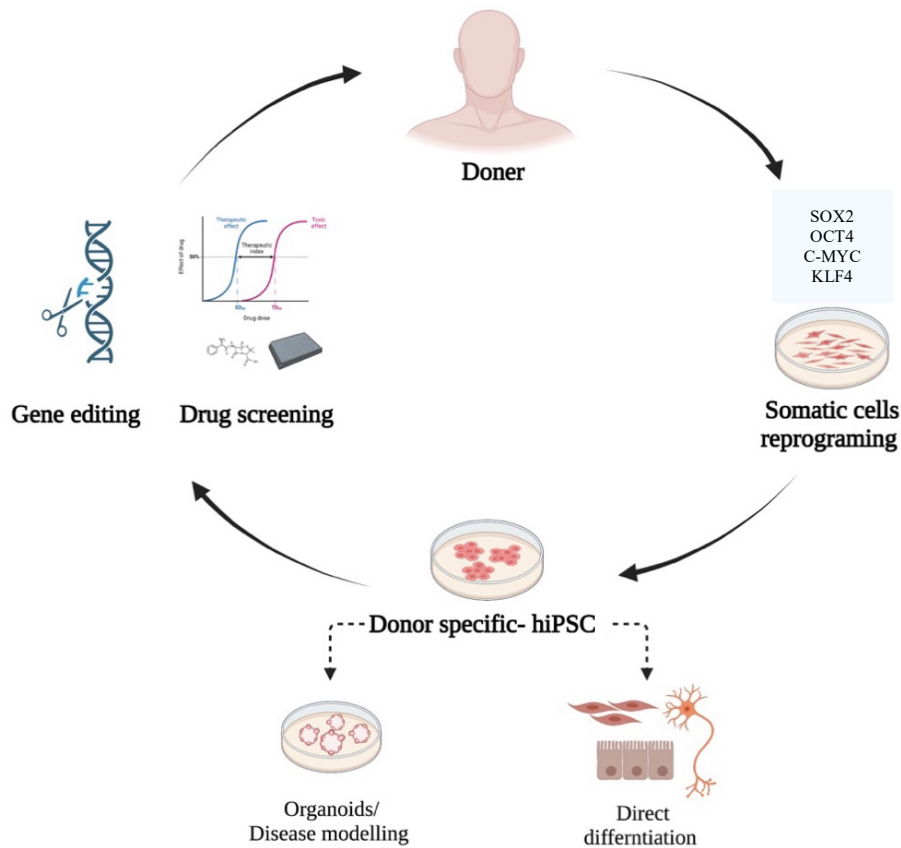


Figure 1.5 Applications of hiPSC.

A Schematic shows hiPSC obtained from adult somatic cells via reprogramming using four transcription factors (SOX2, OCT4, C-MYC, KLF4). Cells can be obtained from healthy donors or patients, which allows investigation of molecular or cellular phenotypes through direct differentiation or 3D organoid systems that are amenable to multiple applications, including gene editing and drug screening. Figure was created with BioRender.com.

1.2.1 Modelling development and its importance

The emergence of hiPSC -based models and, notably, the improvement in differentiation protocols and genetic manipulations offer great opportunities to investigate the mechanism of many aspects of the human embryo (Zhu and Huangfu, 2013). Their potential to be differentiated into all cell lineages *in vitro* is applicable to generate distinct organ structures such as the pancreas, intestine, liver, brain, and lung that recapitulate the native tissue (Pagliuca et al., 2014, Sato and Clevers, 2013, Csobonyeiova et al., 2015, Dye et al., 2015).

Monolayer differentiation protocols have been widely employed to mimic signalling pathways during *in vivo* embryonic development by manipulating growth factors or cytokines in the culture medium (McCauley and Wells, 2017, Lenne et al., 2021). The hiPSC -derived cell types in traditional two-dimensional (2D) systems are only restricted to express markers of specific lineage but lack tissue organisation (Zhu and Huangfu, 2013, McCauley and Wells, 2017). However, the complexity of the *in vivo* processes and capacity of self-organisation in 2D systems is not fully adequate. This opens the opportunity for three-dimensional (3D) models and organoids system (Simunovic and Brivanlou, 2017). The basic 3D technique is multi-cellular aggregates embryoid bodies (EBs) that express some features of the *in vivo* signalling cues and phenotype aiming to understand the molecular and cellular events. In most human models, the EBs undergo spontaneous differentiation and poorly assemble the native tissue organisation (Simunovic and Brivanlou, 2017, McCauley and Wells, 2017). Therefore, recent efforts have been made to modify the 3D structure using bioengineering approaches for more sophisticated culture systems. These advances in 3D culture strategies developed an organ-like structure termed organoids, a PSCs-derived structure consisting of multiple cell types and tissue layers mimicking the complexity of the human organ (Simunovic and Brivanlou, 2017, Zhu and Huangfu, 2013, McCauley and Wells, 2017). Several studies adopted this method which provides a unique tool to investigate the process of organ development or tissue regeneration in adults, particularly for primary cells that are difficult to access, such as neurons, gut and early embryonic development (Clevers, 2016, Lancaster and Huch, 2019, Kim et al., 2020).

The use of hiPSC as a starting point owing to their ability to differentiate into the three germ layers (ectoderm, mesoderm, and endoderm) in the absence of the extraembryonic tissue is a great advantage (Lancaster and Huch, 2019). Manipulating culture conditions through signalling factors or extracellular matrices (ECM), microenvironment has proven very successful in generating endoderm-derived organoids such as intestine, liver, and pancreas, ectodermal organoids including mini-brains, and mesoderm-derived organoids such as kidney and blood vessels (Kim et al., 2020, Clevers, 2016). The ECM is a highly dynamic factor that influences cell behaviour, self-renewing and fate decisions; however, changes in ECM composition resulted in various diseases (Hofer and Lutolf, 2021, Bateman et al., 2009, Cox and Erler, 2011). Matrigel or Geltrex have been widely used to model artificial ECM matrices to provide cell-ECM interactions in the structure of the organoids (Hofer and Lutolf, 2021, Kleinman and Martin, 2005). Enhanced cell viability, growth and differentiation have been reported in various organoids. The lack of flexibility in modifying the physical properties is a major limitation in defining cellular interaction and signalling mechanisms (Kleinman and Martin, 2005, Hofer and Lutolf, 2021).

Furthermore, modern bioengineering strategies such as designing synthetic hydrogels are now effectively poised to mirror more closely native microenvironments (Lutolf and Hubbell, 2005). These biomaterials allow controlling stiffness, degradability, and adhesions, thereby opening opportunities to investigate the impact of the microenvironment on organoid growth and differentiation. This sophisticated approach has been used successfully to support intestinal organoid and neural tube formation, which showed better viability and organisation compared to Matrigel (Hofer and Lutolf, 2021, Cruz-Acuña et al., 2017, Ranga et al., 2016). Overall, several studies have proposed use of 3D culture systems as a valuable tool to dissect the role of the physical microenvironment on hiPSC self-organisation and morphogenesis (Terhune et al., 2022, Hofer and Lutolf, 2021, Lancaster and Huch, 2019).

1.2.2 Models of gastrulation *in vitro*

The limitation of obtaining embryos at an early stage due to both ethical and technical reasons opens opportunities for the use of animal models such as mice, *Xenopus* and chicken to provide insight into the human embryogenesis (Beccari et al., 2018, Green, 2002, Chapman et al., 2001, Arias et al., 2022). The fundamental signalling pathway is well-studied in mouse embryos owing to its similarity to human development; however, there are significant variations between the two models in shape and time (Rayon et al., 2020, Molè et al., 2021a). One of the main differences is that the early mouse embryo creates a cup-shaped structure. In contrast, the human embryo forms a flat disk shape suggesting that both species have different mechanisms that direct morphogenesis and cell fate decisions (Molè et al., 2021a, Niakan et al., 2012).

Therefore, intense research focuses on developing *in vitro* models and remarkable efforts to generate a reminiscent model of an early human embryo (Vianello and Lutolf, 2019). Using hESC or hiPSC, various models have been established, including a 2D system (simplicity) and 3D systems (complexity) (Warmflash et al., 2014, Moris et al., 2020). These models enable the understanding of the mechanism of morphogenesis in human embryos and capture complex developmental events. Such models are amenable to gene editing and can be combined with drug screening to tackle quantitative questions, which can help improve developmental biology and fertility medicine (Heemskerk and Warmflash, 2016, Arias et al., 2022).

1.2.2.1 2D systems

The stem cells culture advancements enabled the use of micropatterned substrates that provide geometrical control and organised signalling environments to recapitulate aspects of *in vivo* gastrulation (Warmflash et al., 2014). This platform was created by coating the culture surfaces with a substrate that prevents cell and protein adhesion, generating defined ECM regions. Biomaterials such as polymer poly(L-lysine)-grafted-poly(ethylene glycol) (PLL-g-PEG) or poly(dimethylsiloxane) (PDMS) stamps are often used to create the desired pattern (D'Arcangelo and McGuigan, 2015, Théry, 2010).

Micropatterned systems in 2D have been used to investigate the signalling pathways underlying self-organisation and fate decisions in early human development. Various groups have harnessed techniques to develop models of gastrulation by integrating biochemical cues and control of the pattern size (Warmflash et al., 2014, Camacho-Aguilar and Warmflash, 2020). Initially, hESC were cultured on micropatterned designed by PDMS stamps to examine the effect of geometry on cell fate, which resulted in spontaneous differentiation into endoderm and neural lineages without the addition of exogenous growth factors (Bauwens et al., 2008). Another study has demonstrated that hESC cultured on defined patterns can radially organise and differentiate into cells of the three germ layers following BMP4 treatment. The pattern formation in the colonies showed ectoderm (SOX2 positive cells) in the innermost region, surrounded by concentric rings of mesoderm (BRA and EOMES positive cells) and endoderm (SOX17 positive cells) cells with an exterior TE ring (Warmflash et al., 2014). In a later study, hiPSC cultured on micropatterned surfaces produced differentiated cells specified to the three lineages. These processes were guided by stepwise biochemical models predicting the formation of radial signalling gradient upon BMP4 induction (Tewary et al., 2017).

In 2D models, germ layer differentiation is achieved by manipulating signalling pathways of WNT, NODAL, and BMP, highlighting the interplay between morphogen dynamics that direct cell fate (Camacho-Aguilar and Warmflash, 2020). Nevertheless, the interconnection of patterning, cell fate and morphogenesis during embryo development remains difficult to untangle.

1.2.2.2 3D systems

Several 3D models have been employed to mimic the *in vivo* environment cues to provide a reliable platform to investigate signalling pathways and morphogenesis (Bedzhov and Zernicka-Goetz, 2014, Simunovic et al., 2019, ten Berge et al., 2008, Moris et al., 2020). The proposed systems address the interconnections across the two questions of how germ layer fate patterns form and how the shape of the embryo emerges.

One approach is the use of co-culture of hESC and extraembryonic trophoblast stem cells (ETS) to develop embryo-like structure (Bao et al., 2022, Bedzhov and Zernicka-Goetz, 2014). Aggregated cells in Matrigel or collagen ECM-coated matrices formed

cavity, axis polarisation and self-organisation recapitulating gastrulation events of a natural embryo. Their finding demonstrated that interaction between embryonic and extraembryonic cells in 3D ECM is necessary to form embryo-like axis elongation and induce gene expression pattern (Harrison et al., 2017, Morris et al., 2012).

On the other hand, various protocols have harnessed systems to trigger gastrulation *in vitro*, focusing on controlled geometrical size and biochemical cues without adding or forming extra-embryonic tissues (Siggia and Warmflash, 2018, Deglincerti et al., 2016). These studies have shown inducing a range of morphogens of the TGF- β family, including BMP4 and NODAL, the WNT and FGF or their inhibitors to regulate hESC/hiPSC germ layers differentiation (Liu and Warmflash, 2021, Martyn et al., 2018). A 3D hESC model of epiblast exposed to exogenous BMP4 signalling resulted in spontaneous segregation with a mutually exclusive expression of SOX2 /BRA (Simunovic et al., 2019). This model demonstrated the symmetry breaking without showing axial elongation; however, after BMP4 treatment, epiblast formed the anterior domain of SOX2 (pluripotent) and posterior domain of BRA (mesoderm) (Simunovic et al., 2019). Another group has shown ESCs aggregates could specify mesoderm when WNT pathway is stimulated; nonetheless, WNT inhibition induces neuroectoderm differentiation (ten Berge et al., 2008).

Human ‘gastruloids’ derived from hPSCs arrange as a multicellular system that undergoes elongation and differentiates to form the three germ layers (Arias et al., 2022, Moris et al., 2020). Recently, Moris et al. proposed a 3D hESC gastruloids culture system most similar to early embryo development using hESC induced with WNT signalling, which builds upon a previously defined 3D model of mouse gastruloids (Moris et al., 2020, Beccari et al., 2018). Here, hESC were pre-treated with CHIRON pulse a (WNT agonist) before the spheroid formation, which triggered symmetry breaking and thus drove elongation along the A-P axis in the absence of extraembryonic tissues (Moris et al., 2020, Bedzhov and Zernicka-Goetz, 2014). Human gastruloids formed polarised patterns of the three germ layers (ectoderm, mesoderm, and endoderm), and spatial transcriptomics analysis showed patterns of HOX genes expression and somitogenesis mirroring human development *in vivo* (Moris et al., 2020).

Furthermore, 3D gastruloids cultured under hypoxia conditions showed spontaneous axial elongation and enhanced mesodermal differentiation in the absence of a WNT activation (López-Anguita et al., 2022).

The ability of these various 3D gastrulation-like models to recapitulate aspects of gastrulation, including axial elongation and patterning organisation, morphogenesis and signalling (Bao et al., 2022) helped overcome limitations of the 2D systems (Lenne et al., 2021, Liu and Warmflash, 2021).

1.2.3 Modelling human diseases and drug discovery

Integrating disease modelling derived from patient-specific hiPSC that manifest cell-based phenotype and drug compounds assays provides a high-throughput screening (HTS) platform to ensure efficacy and safety (Grskovic et al., 2011, Seki et al., 2020). Successful attempts to generate robust *in vitro* models of various diseases to identify pathological mechanisms have been reported (Grskovic et al., 2011, Shi et al., 2017, Rowe and Daley, 2019). Ebert and colleagues described spinal muscular atrophy (SMN) disease modelling by generating SMN patient-derived hiPSC line and another line obtained from a healthy relative differentiated into motor neurons. These cells successfully recapitulated the disease genotype and phenotype in culture, thereby used to analyse the cellular response to drug compounds aiming to rescue motor neuron defects (Ebert et al., 2009, Grskovic et al., 2011). Another study focussed on modelling a rare fatal neural disorder named (Familial dysautonomia) characterised by a mutation in the I- κ -B kinase complex-associated protein (IKBKAP) gene. Therefore, this mutation results in autonomic and sensory neuron degeneration (Saito-Diaz and Zeltner, 2019a, Shi et al., 2020). Patient-specific hiPSC were differentiated towards the neural crest lineage, which expresses low IKBKAP *in vitro*, mirroring the disease phenotype *in vivo*. In this study, various drug molecules screening was performed using the developed hiPSC model, revealing several promising candidate drugs that could increase the expression of IKBKAP (Shi et al., 2020). Since then, several disease-specific hiPSC have been generated to identify novel therapeutic strategies targeting Parkinson's disease (Nguyen et al., 2011, Seibler et al., 2011), Amyotrophic lateral sclerosis (Wainger et al., 2014), and Alzheimer's disease (Bright et al., 2015). These studies illustrate the impact of hiPSC-

based disease modelling could presumably be used to enhance the personalised medicine approach to the drug discovery (Saito-Diaz and Zeltner, 2019b).

Utilising hiPSC in cell-based assays for HTS by testing large-scale compounds is an effective approach to explore drug side effects and cytotoxicity (Shi et al., 2017, Saito-Diaz and Zeltner, 2019b). The ability to test cells from patients can provide a valued insight into assessing phenotypic behaviour in response to compounds' sensitivity or toxicity during clinical trials in the drug development (Shi et al., 2017, Grskovic et al., 2011). Clinical trial failure due to compounds' efficiency or safety is widespread. Therefore, many pharmaceutical companies have established the use of healthy hiPSC and patients derived for proof-of-concept trials (Grskovic et al., 2011). For example, hepatocyte-like cells derived from hiPSC express functional markers that are used to explore the response to hepatotoxic drugs (Shi et al., 2017, Takayama et al., 2012). Another study demonstrated that hiPSC-cardiomyocytes could be employed to obtain a reproducible assessment for the electrophysiological cardio-toxicity screening (Harris et al., 2013). Likewise, this approach has been proposed to predict neuro-toxicity in response to a large set of compounds during clinical trial (Schwartz et al., 2015). Differentiated hiPSC to various cell types provide a clinically relevant platform to predict drug toxicity or sensitivity of potential compounds during drug development (Shi et al., 2017).

1.2.4 Cell therapy

The use of patient-specific hiPSC in cell-based therapy is a promising application in the field of regenerative medicine. This provides an opportunity to overcome the current challenges of allogeneic transplants, including immunogenicity and the limited source of donor tissues (Yamanaka, 2020). Since the establishment of hiPSC and the growing excitement in cell-based therapies, few successful autologous hiPSC transplant cases have been reported (Kimbrel and Lanza, 2020, Okano and Sipp, 2020). The first breakthrough study was reported in 2017 for the cell replacement of age-related macular degeneration (AMD). In this study, autologous hiPSC differentiated toward retinal pigment epithelial (RPE), which was then transplanted into the patient's eye (Mandai et al., 2017). The transplanted RPE cells exhibited gene expression consistent with those of the native RPE tissue; four years later, a follow-up study verified the treatment efficiency without signs of immune rejection (Takagi et al., 2019). In another study for a patient with Parkinson's disease, autologous hiPSC-derived dopamine neurons were transplanted in the patient. After two years of transplantation, clinical evidence showed graft survival and improved patient symptoms (Schweitzer et al., 2020). Furthermore, ongoing clinical trials using autologous hiPSC-based cell therapies on treating diseases such as corneal epithelial, spinal cord injuries, and cardiomyocytes for heart failure to avoid the risk of immune rejection response (Okano and Sipp, 2020).

Although these autologous clinical trials showed encouraging results for hiPSC-based cell therapies, manufacturing production and biobanking costs remain major limitations. In contrast, the advent of allogeneic hiPSC approaches scaled up manufacturing batch production and reduced the cost (Yamanaka, 2020, Okano and Sipp, 2020). The hiPSC can be cryopreserved and immediately accessible for patients who require acute treatment, unlike autologous derived cells, which take time to generate before implantation. In addition, hiPSC can be obtained from healthy donors and ensure the delivery of healthy cells, not harbour disease-causing mutations. However, the critical issue with this type of cell therapy is their rejection due to incompatibility with the host immune system (Yamanaka, 2020, Pearl et al., 2011). A possible approach to avoid the risk of immune response from the patient is human leukocyte antigen (HLA)-matching (Hanatani and Takasu, 2020, Sullivan et al., 2018). These cells are clinical grade that was

first produced and biobanked in many institutes, including the Centre for iPS Cell Research and Application (CiRA) in Japan and UK's Cell and Gene Therapy Catapult (Barry et al., 2015, Umekage et al., 2019). Nevertheless, some reports revealed that HLA-matching type failure was observed in several cases. Further investigations are needed to validate the safety and whether these cells are enough to reduce the long-term immuneorejection (Okano and Sipp, 2020, Sugita et al., 2020).

Another approach in cell therapies is the gene editing of hiPSC-derived models such as clustered regularly interspaced short palindromic repeats (CRISPR), which targets the correction of specific gene mutations for disease treatments (Kimbrel and Lanza, 2020, Yamanaka, 2020). For example, in a mouse model, the phenotype of sickle cell anaemia could be rescued after the implantation of hematopoietic progenitors *ex-vivo* from the autologous hiPSC (Hanna et al., 2007).

Notably, the progress in developing hiPSC-based cell therapy technologies increased the number of potential clinical trials offering unique tools for personalised and regenerative medicine. However, therapeutic safety and efficiency remain vital concerns (Okano and Sipp, 2020).

1.2.5 HipSci

The applications of hiPSC in modelling diseases, aspects of development and cell therapy attempts are well-established. However, several studies suggested that hiPSC lines are heterogeneous due to the genetic background of the individual cell line between donors (Kim et al., 2011, Leha et al., 2016, Kilpinen et al., 2017). The high variability of phenotypic and genetic characterisations of hiPSC restricts their use for potential studies and clinical trials (Kilpinen et al., 2017).

The Human Induced Pluripotent Stem Cells Initiative (HipSci) (www.hipsci.org) is an open-access resource of hiPSC lines obtained from healthy donors and patients with genetic diseases. The HipSci project has generated large-scale of hiPSC libraries over 700 lines, which have been characterised via genomic and proteomic assays and analysed for morphology, proliferation, and cell adhesion properties (Streeter et al., 2016, Kilpinen et al., 2017). The data for each cell line is readily accessible to the wider research society as

a reference which is an important tool to identify and elucidate phenotypic outliers associated with specific hiPSC due to genetic variation. A later study was built upon the initial characterisation of HipSci resource and DNA data sets; they integrated high-content imaging and gene expression from 110 hiPSC lines to identify inter-individual genetic variation that drives cell phenotype. hiPSC lines were cultured on different concentrations of fibronectin (ECM protein), an extrinsic factor (environmental), to examine cell behaviour (Figure 1.6 A). These observations were then linked to the intrinsic factor (genetic) characterisation of hiPSC demonstrated phenotypic outliers in 37 cell lines (Vigilante et al., 2019). A recent study by the group in our centre utilised the HipSci cell lines to establish a 2D platform to identify genetic variants that influence hiPSC differentiation (Figure 1.6 B). Their findings showed that normal hiPSC cell lines undergo differentiation. However, cell lines with genetic variation exhibited outliers in the differentiation (Vickers et al., 2021). This platform opens the opportunity to investigate genetic variations that impact lineage differentiation and morphogenesis in 3D models, which could reveal unidentified phenotypic outliers in 2D models.

HipSci is a unique source to investigate the influence of genetic background on inter-individual variability in cell behaviour and differentiation phenotypes. This will remarkably improve the outcome of hiPSC-disease modelling, drug development or cell therapeutics studies.

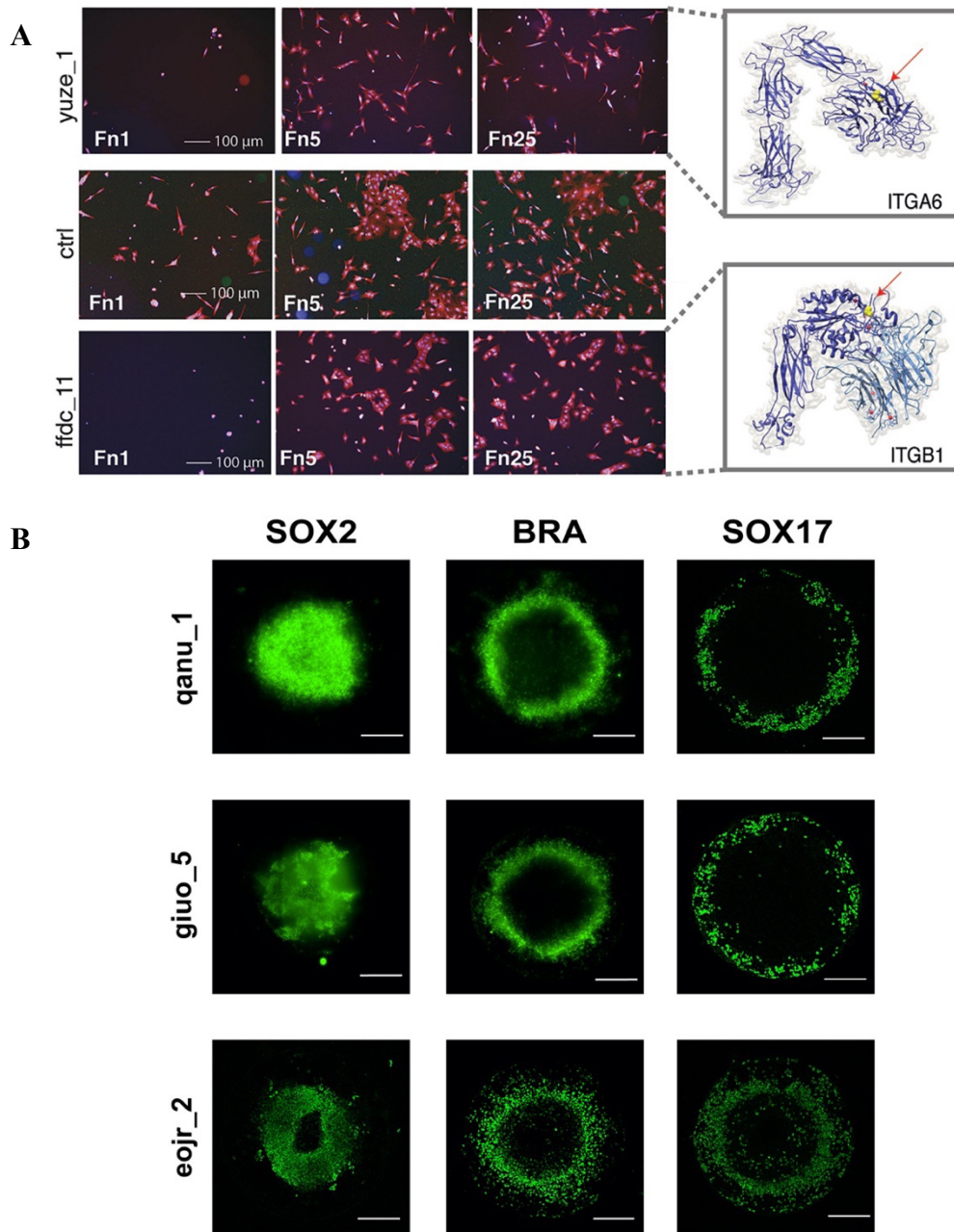


Figure 1.6 The identification of phenotype outliers in hiPSC that correlate with genetic variations using HipSci cell lines.

A) Selection of hiPSC cell lines were cultured and screened on different fibronectin concentrations (Fn1, Fn5, and Fn25), cell lines (Yuze_1) on top, and (ffdc_11) associated with nsSNVs in genes related to cell adhesion integrins (ITGA6 and ITGB1) respectively. These cell lines showed phenotypic outliers in cell behaviour compared to the control cell line in the middle. **B)** 2D micropattern system showed variation in germ layers differentiation between cell lines. Figures adapted from (Vigilante et al., 2019, Vickers et al., 2021).

1.3 *The role of the tissue microenvironment*

In human embryo development, when the blastocyst reaches the uterus, it becomes embedded into the uterine wall and completely embedded by the inner layer of uterus tissue. This provides mechanical interactions between the environment (uterus) and embryonic tissues, which play a key role in cell fate and direct embryo development. Physical confinements and mechanical forces exerted from the uterus, such as constraint, provide pressure that controls body axis formation and cell fate commitments (Vianello and Lutolf, 2019, Lenne et al., 2021, Petzold and Gentleman, 2021).

1.3.1 ECM and cell interactions

Cell-ECM interactions through integrins within the local tissue environment regulate the tri-lineage germ layers specification (Ranga et al., 2014, Arnold and Robertson, 2009). This is mediated by physical cues from molecules such as integrins that bind to ECM proteins that promote cell adhesion and govern differentiation (Figure 1.7) (Vining and Mooney, 2017, Vianello and Lutolf, 2019). Integrins are transmembrane receptor heterodimers for cell-ECM adhesion consisting of α 18, and β 8 subunits; their specific expression depends on the type of cell-ECM interaction (Kawase and Nakatsuji, 2023, Vitillo and Kimber, 2017). Integrins link the ECM with intracellular cytoskeleton (such as actin) allowing cells to sense the external stimuli of the local environment. In addition, integrins transmit biochemical signals into the cell and contribute to trigger intercellular signalling pathways and regulate cell attachment, cell spreading, migration and proliferation (Vitillo and Kimber, 2017, Jansen et al., 2017). During the early stages of development, β 1-integrin secreted by extra-embryonic tissue initiates a signal to bind to the ECM of the epiblast which facilitates polarisation and tissue morphogenesis (Bedzhov and Zernicka-Goetz, 2014, Molè et al., 2021b). Lack of integrin signalling is associated with cells' inability to form polarising structures and to establish the gastrulation process (Molè et al., 2021b). Moreover, it has been demonstrated that the ECM modulate cell fate decisions through integrins molecule that transmits signals from the ECM proteins to the cell that stimulates the cytoskeleton remodelling and tissue rearrangement for germ layers patterning (Petzold and Gentleman, 2021, Cheng et al., 2013). It has been reported that both hESC and hiPSC express a range of integrins activated when bound to selective

ECM substrates, such as laminin-rich, vitronectin, and fibronectin which mediate cell adhesion (Vitillo and Kimber, 2017).

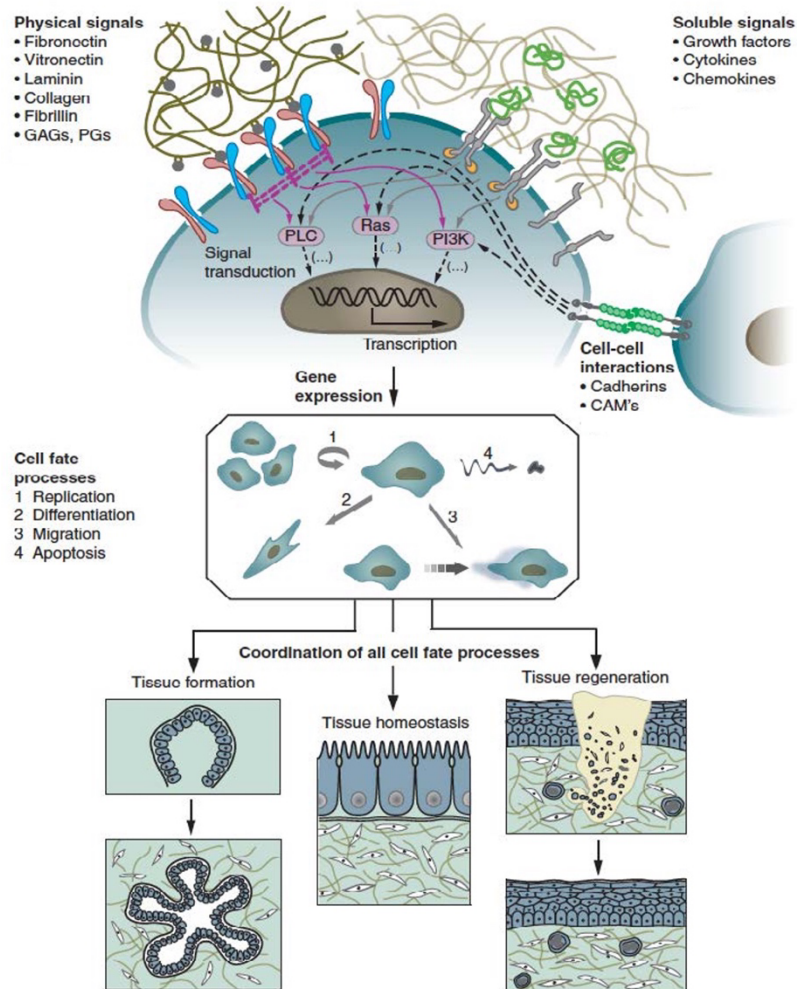


Figure 1.7 The role of microenvironment in cell behaviour and differentiation.

The interaction between the cell and the local environment via integrins and cell adhesion molecules. This specific cell- ECM binding induce intracellular signalling that regulates gene expressions, cell phenotypes, cell fates, homeostasis and tissue regeneration. Figure adapted from (Lutolf and Hubbell, 2005).

1.3.2 Bioengineering approaches

The use of free-floating 3D models (i.e., spheroids in suspension culture) to manipulate the molecular and physical stimuli provided by the surrounding tissue is limited. Mirroring the *in vivo* microenvironment of the human embryo to understand the interaction between signalling molecules and physical forces from local tissue remains challenging (Lenne et al., 2021, Vianello and Lutolf, 2019). Bioengineering approaches have become promising alternatives to overcome the limitation of manipulating the physical constraints more closely to the native tissue environment (Gjorevski and Lutolf, 2017).

1.3.2.1 Synthetic hydrogel

Synthetic biomaterials such as PEG-based hydrogels are cross-linked polymer networks, hydrophilic, and water-swollen, used to provide well-defined, reproducible environments. The hydrogel network can be formed at different sizes to allow for nutrients and growth factor transport, and their physical properties (i.e., stiffness, degradation) can be modified to design a 3D culture system that mimics the native ECM environment (Walters and Gentleman, 2015, Ranga et al., 2014). The cell-ECM interactions play an important role in cell fate decisions and cell behaviour (Blache et al., 2022). *In vivo* cells receive biochemical or mechanical cues when binding to the ECM or via cell-cell adhesion, thus allowing cells to control matrix remodelling and govern many cellular functions. Hydrogels can be used to manipulate cell-ECM in a 3D *in vitro* model to create a culture system that brings together the mechanical and biochemical cues and gain insight into the impact of cell fate decisions (Blache et al., 2022, Walters and Gentleman, 2015, Guvendiren and Burdick, 2013). This approach often provides a suitable scaffold for encapsulated cells to promote adherence, proliferation, and differentiation into different cell types.

Previously, the hydrogel system has been reported by Lutolf's group using 8-arm PEG-vinyl sulfone (VS) and PEG-acrylate (Acr) functionalised by transglutaminase factor (FXIIIa). The hydrogels initially crosslink with two identical bifunctional peptides, which resulted in reacting with the chain end of any PEG arm, which disturbs the network efficiency (Grskovic et al., 2011, Gjorevski and Lutolf, 2017, Gupta et al., 2021).

However, another hydrogel system has been described to overcome the limitation of the previous system's enzymatic reaction and insufficient network formation by using a 4-arm PEG-based system and hetero-bifunctional peptide. This improves network efficiency, especially when creating low polymer concentration hydrogels below 4% (Jowett et al., 2021, Lust et al., 2021, Norman et al., 2021).

Constructing such a complex 3D platform with independent control of biochemical cues, ECM, and hydrogel physical properties enables us to elucidate how extrinsic factors influence cell fate decisions (Walters and Gentleman, 2015, Vining and Mooney, 2017). Indeed, hydrogel stiffness can be tuned by varying the polymer concentration, and biological cues controlled by incorporating integrin-binding arg-gly-asp (RGD) and matrix metalloproteinase (MMPs) degradable peptide sequences (Gjorevski et al., 2016, Petzold and Gentleman, 2021). The RGD sequence is a cell attachment site binds to specific integrins such as $\alpha\beta3$, $\alpha\beta5$ to promote cell adhesion, proliferation, and cell viability (Yamada et al., 2022, Jansen et al., 2017). Various studies have determined the role of matrix stiffness and degradability on multiple cellular processes, including cell proliferation, differentiation, and migration (Vining and Mooney, 2017, Gjorevski and Lutolf, 2017). Low matrix stiffness (soft conditions) promotes cell proliferation, whereas intermediate conditions support self-renewal and colony formation of single mouse embryonic stem cells (mESC) (Ranga et al., 2014). The cell adhesion (RGD) ligand density is shown to induce lumen formation in intestinal organoids and control the neural (Jansen et al., 2017) tube morphogenesis (Gjorevski and Lutolf, 2017, Ranga et al., 2016). Recent work showed intestinal organoid formation is favoured in hydrolytically degradable or viscoelastic (rather than purely elastic) matrices (Jowett et al., 2021). Overall, these flexible physical properties of the hydrogel are a potential tool to investigate the role of the microenvironment and morphogen regulating hiPCSs morphology and differentiation.

1.4 *High-content image analysis*

High-content analysis (HCA) approaches to obtain quantitative readouts from digital microscopy images provide unprecedented opportunities to derive automated multi-parametric data to quantify cell behaviours and morphology at the single-cell level (Mattiuzzi Usaj et al., 2016). This approach can be used in high throughput to generate data from many conditions. Studies have employed HCA to characterise the effect of small molecules in several aspects of cell-based assays, including cell proliferation, cell morphology, cell cycle, cytotoxicity, and protein expression (Kerz et al., 2016, Massey, 2015). The cells under distinct culture conditions exhibit dramatic changes over time including cell shape (roundness vs. spreading) (Leha et al., 2016, Kerz et al., 2016). These phenotypic features are often analysed by object detection and segmentation methods to create analysis pipelines. In most pipelines, multi-channels per image were used as a reference to identify cellular objects or phenotypes; however, an automated workflow using phase contrast images has been described based on cell shape and area. In this method, live imaged hiPSC were analysed in response to different concentrations of fibronectin by integrating a novel CellProfiler- based image analysis pipeline. This platform generated robust image segmentation, which can be utilised to analyse other cell types and to characterise large panels of hiPSC (Kerz et al., 2016). Another study has reported high-content image analysis coupled with immunofluorescence to characterise endothelial cells phenotype from different sources such as hiPSC-derived endothelial cells and human umbilical vein endothelial cells. This platform enables to analyse of cell phenotypes under distinct culture conditions, including the presence or absence of biochemical cues (Wiseman et al., 2019).

Different assays can be set up to capture one specific condition for screening analyses, such as the effect of a drug and perturbations, or profiling assays to compare conditions to characterise a panel of cell lines. Quantitative information about cell behaviour can be obtained from both live imaging data and endpoint image datasets (Mattiuzzi Usaj et al., 2016, Danovi et al., 2013). However, analysing images acquired from live microscopy is challenging due to the 2D representation (Kerz et al., 2016). Clearly, there is an advantage to combining these two methods. In particular, morphogenetic events can be better

understood if observed at time intervals and if information for single cells can be obtained (Wiseman et al., 2019).

Improvements in microscopy, computational capabilities and data analysis have enabled to deliver of robust quantitative cell phenotypic data within cell populations, allowing researchers to answer various biological questions (Massey, 2015, Mattiazzi Usaj et al., 2016). A wealth of image information can be obtained through proprietary software including Harmony (PerkinElmer), and Imaris (Oxford Instruments) or open-source software such as CellProfiler (Carpenter et al., 2006) and Icy bioimage software to gain quantitative readouts (Kerz et al., 2016, Hale et al., 2018).

1.5 *Aims & hypothesis*

Cell fate decision during gastrulation is regulated by cell-cell interactions, cell-ECM communications, and signalling mechanisms of the native microenvironment and its mechanical properties (Arnold and Robertson, 2009, Vianello and Lutolf, 2019). Several 3D models under distinct environments cues have been described as mirroring aspects of gastrulation and obtaining an organised differentiation pattern (Bedzhov and Zernicka-Goetz, 2014, Simunovic et al., 2019, ten Berge et al., 2008, Moris et al., 2020). The mechanism of the signalling pathway during this event has been well-studied in micropattern 2D systems suggesting that the BMP4 signal is the main regulator to initiate *in vivo* gastrulation (Warmflash et al., 2014, Tewary et al., 2017). Moreover, insights into how biochemical cues and physical cues trigger tissue rearrangements and whether they are regulated mechanically (tissue environment) or biochemically (cellular response) are not fully investigated.

In my project, the aims are:

- 1) To investigate how biochemical cues (BMP4/ KSR) influence morphogenesis and the tri-germ layers lineages in a 3D hiPSC model of gastrulation.
- 2) To explore how physical confinement separately influences morphogenesis and germ layers differentiation.

Here, I proposed an adapted method of a previously well-defined 2D micropattern platform based on BMP4 induction in a 3D model and integrating a PEG-peptide hydrogel system to provide physical constraints. I hypothesised that BMP4 provides sufficient signals to trigger symmetry breaking, elongation and differentiation of hiPSC spheroids in suspension culture. Next, I postulated that cellular tension governs spheroids morphological changes in 3D models in suspension. I also hypothesised that PEG-peptide hydrogel systems would inhibit elongation and thus enable us to interrogate if physical confinement affects not just morphogenesis but also cell fate specification.

The main objectives of this thesis are:

- To characterise the distinct morphological phenotypes of 3D hiPSC spheroids cultured under self-renewing and differentiating media conditions and to quantify the dynamic changes using HCA (Chapter 3).
- To investigate the contribution of morphological changes and the germ layers specification under distinct medium conditions (biochemical cues) via protein expression of specific markers using immunostaining (Chapter 4).
- To explore the effect of PEG-peptide hydrogel encapsulation (physical confinement) in morphological changes and germ layers differentiation (Chapter 5).

These objectives will provide a platform to dissect the contribution of biochemical and physical cues addressing whether morphogenesis is required to direct lineage differentiation and patterning.

2 MATERIALS AND METHODS

2.1 *Cell culture*

2.1.1 hiPSC cells

hiPSC lines were selected from HipSci biobank (www.hipsci.org). Cell lines were obtained from various donors who donated skin fibroblast and reprogrammed using Sendai virus vectors (CytoTune, Life Technologies, A1377801) expressing the four reprogramming factors OCT4, SOX2, C-MYC and KLF4. Each clonal hiPSC line is anonymised with four letters followed by a number representing the clone from that donor. Cells are assessed for quality control profile to verify pluripotency and genotyping as previously described (Kilpinen et al., 2017).

2.1.2 hiPSC thawing and culture

Selected hiPSC cells obtained from a healthy donor (Hoik_1), which has been chosen for its growth quality and viability post-thawing. Cells were cultured in a feeder-free medium using a 6-well plate (Thermo Fisher Scientific,10578911) coated with 10 ug/ml vitronectin (Stemcell Technologies, 07180) in phosphate buffer saline (PBS, Sigma, P4474). Vitronectin-coated 6-well plate (Thermo Fisher Scientific,10578911) was incubated for 1 hour at room temperature (RT) and washed once with PBS. On thawing, hiPSC were resuspended in Essential 8 kit (E8) medium containing 2% E8 supplement (50x) (Thermo Fisher Scientific, A1517001), 1% Penicillin Streptomycin (5000U/ml) (Life Technologies,15070063). Cells were centrifuged at 200g for 3 minutes and subsequently resuspended with E8 medium supplemented with 10 µM Y-27632 Rho-kinase inhibitor (ROCKi) (ENZO Life Sciences, ALX-270-333-M005) to improve cells recovery post thawing, then cultured on a vitronectin-coated 6-well plate and placed in a humidified incubator at 37 °C, 5% CO₂. The following day, the medium was changed to E8 medium upon colonies formation, fed daily and passaged every 4-5 days when reaching 70-80% as routine hiPSC maintenance.

2.1.3 hiPSC maintenance

For hiPSC passaging, as previously described, a 6-well plate (Thermo Fisher Scientific, 10578911) was coated with 10 µg/ml vitronectin (Stemcell Technologies, 07180) in PBS (Sigma, P4474). hiPSC colonies were washed once with Hank's balanced salt solution (HBSS) (Gibco, 14170120) and detached by incubating in Versene (Gibco, 15040033) for 3-4 minutes at 37 °C, 5% CO₂. After the Versene solution was removed, cells were released from the surface using E8 medium, followed by plating cells on vitronectin-coated 6-well plates at a split ratio (1:6 – 1:10). Cells were cultured in a humidified incubator at 37 °C, 5% CO₂ with daily feeding.

2.1.4 hiPSC freezing

Cells were frozen to generate long-term stocks and cryopreserved in liquid nitrogen containers. When hiPSC colonies reached 70-80% confluence, cells were washed with HBSS, detached using Versene (Gibco, 15040033) for 3-4 minutes, and incubated at 37 °C, 5% CO₂. Cells were resuspended in E8 medium containing 10% dimethyl sulfoxide (DMSO) (Sigma, D2650) and transferred to cryogenic vials (Nuc cryoTubes, 377267). Cells were maintained in Mr Frosty™ freezing container (Thermo Fisher Scientific, 10110051) at -80 °C for 24 hours; then vials were transferred to liquid nitrogen.

2.2 *Spheroids formation and 3D culture*

2.2.1 Spheroids derivation from hiPSC

Prior to hiPSC dissociation into single cells and seeding, low attachment 96-well V-bottom plates (Thermo Fisher Scientific, 268200) were coated with 5% (w/v) Pluronic solution (Sigma, P2443) in PBS (Sigma, P4474). Cells on plates were centrifuged at 500g for 5 minutes to settle, incubated for 30 minutes at RT, and washed once with PBS (Gibco). To dissociate hiPSC colonies into single cells, colonies were washed once with HBSS (Gibco, 14170120) and incubated in Accutase (Gibco, A1110501) for 4 minutes at 37 °C, 5% CO₂. Cells were resuspended in E8 medium (Thermo Fisher Scientific, A1517001) to inactivate the Accutase effect. Cells were centrifuged at 200g for 3 minutes and resuspended in E8 medium supplemented with 10 µM ROCKi (ENZO Life Sciences,

ALX-270-333-M005) to promote the survival of dissociated hiPSC. Single cells were seeded in low attachment 96-well plates at a density of 750 cells/ well and cultured in E8 medium with 10 μ M ROCKi (ENZO Life Sciences, ALX-270-333-M005) to prevent cell apoptosis and enhance cell viability. After seeding, cells were centrifuged at 200g for 2 minutes to bring all single cells to the bottom in the centre of V-bottom well plate and incubated for a further 48 hours at 37° C, 5% CO₂ to allow aggregation (Figure 2.1).

2.2.2 Gastrulation-like induction of hiPSC spheroids

The spheroids formation protocol was modified and adapted from (Ungrin et al., 2008, van den Brink et al., 2014). After 2 days in culture and medium replacement (Figure 2.1), hiPSC spheroids formed were cultured in self-renewing and differentiation conditions as follows before being incubated at 37 °C, 5% CO₂ and cultured for 96 hours; (1) E8 medium supplemented with 2% E8 supplement (50x) (Thermo Fisher Scientific, A1517001), 1% Penicillin Streptomycin (5000U/ml) (Life Technologies,15070063), and 10 μ M ROCKi (ENZO Life Sciences, ALX-270-333-M005); (2) Knock out serum medium KSR consist of Advance DMEM/F-12 medium (Thermo Fisher Scientific, 12634010), supplemented with 20% KnockOut serum replacement (Gibco, 10828010), 1% L-Glutamine (Gibco 25030081), 1% Penicillin Streptomycin (5000U/ml) (Life Technologies,15070063), 0.1mM β -mercaptoethanol (Gibco,31350-010), 10 ng/ml basic fibroblast growth factor (bFGF, Invitrogen, PHG0026),10 μ M ROCKi (ENZO Life Sciences, ALX-270-333-M005), and supplemented with 50 ng/ml BMP4 (R&D, 314-BP-050). For control conditions, (3) E8 medium composition as in (1) supplemented with 50 ng/ml BMP4; and (4) KSR medium as described without adding 50 ng/ml BMP4.

2.3 PEG hydrogels

2.3.1 PEG-peptide conjugation and purification

PEG-peptide conjugates were created following the protocol described in (Jowett et al., 2021, Lust et al., 2021). Custom-designed peptide non-adhesive/ non-degradable Ac-KDW-ERC-NH₂ (consists of amino acids Ala, Cys , Lys, Asp, Trp, Glu, Arg, Cys, Asn) was obtained from (Peptide Protein Research, Ltd. (UK), >98% purity; <https://web.expasy.org/cgi-bin/protparam/protparam>). This custom-designed peptide Ac-

KDW-ERC-NH₂ is a non-functional sequence that does not interact with the cells; however, it was used to produce a physical confinement environment. To create the conjugates, the peptide was dissolved in anhydrous dimethyl sulfoxide (Sigma, D2650) at 10 mg/ml and anhydrous triethylamine (TEA, Sigma, 471283) at a ratio of 2:1 molar to deprotonate the primary amine from the lysine side chain. Then, peptides were conjugated to 4-arm PEG; each arm contains nitrophenyl carbonate (PEG-4NPC) (JenKem Technology, USA). In this reaction, 16.67 mg/ml solution of 10 kDa PEG-4NPC (JenKem Technology, USA) in DMSO (Sigma, D2650) was added to the peptide drop by drop with continuous mixing and allowed to react on an orbital shaker at a 12:1 molar ratio of excess peptide to PEG-4NPC at 160 rpm for 30 minutes at RT. After the reaction was complete, peptide conjugates were snap-frozen using dry ice and lyophilised for three days to remove TEA and DMSO. To decrease disulfate bonds, peptide conjugates were dissolved in a sodium carbonate-bicarbonate buffer pH 8.8 - 9.2 with 0.1g/ml Dithiothreitol (DTT, Sigma, D0632) at a ratio 8:1 molar. The solution was purged with nitrogen gas for 5 minutes to maximise disulphide bond cleavage and incubated for 3 hours at RT. Peptide conjugates were purified four times with MiliQ water in Merck Millipore Ultrafiltration 1MWCO units (10 kDa cut-off). This is followed by snap freezing and lyophilisation peptide conjugates prior to storage at -20 °C.

The PEG-peptide conjugates were then quantified via Ellman's assay (Thermo Fisher Scientific, 22582) to measure the free thiols in peptide conjugates. To achieve this, 4 mg/ml solution of Ellman's reagent was prepared in a reaction buffer of 0.1 M in PBS (Sigma, P4474) at pH 8.0 and 1 mM EDTA (Thermo Fisher Scientific, BP2481) Aliquots of 30 µl from the peptide conjugates were incubated in 50 µl of the prepared buffer and allowed to react for 15 minutes at 30 rpm at RT, followed by UV measurement absorbance at 412nm. The concentration of free thiols in Ac-KDWERC-NH₂ conjugates was calculated using the molar extinction coefficient of Ellman's reagent (14150 M⁻¹ cm⁻¹) and equation $c=A/b\epsilon$ (A is the absorbance of the sample at 412 nm, b is 1 cm and ϵ is the molar extinction coefficient). To quantify the peptide yield conjugated in PEG-KDWERC, 2 µl of the solution was measured using the protein A280 function on the nanodrop. Then, the calculation was performed using ϵ and Mw of the peptide.

2.3.2 PEG-peptide hydrogel formation

PEG-peptide hydrogels were synthesised by reacting 4-arm PEG-peptide conjugates with 4-arm PEG-vinyl sulfone (PEG-4VS, 20 kDa) (non-degradable) or a mixture of 25% 4-arm PEG-4VS and 75% 4-arm PEG- acrylate (PEG-4Acr, 20 kDa) (degradable) (All JenKem Technology, USA). The reaction was performed in stoichiometric ratio 1:1 30mM HEPES buffer at pH 8 (Sigma, H3375) diluted in 1x HBSS (Gibco, 14025092) via Michael's- type reaction. Briefly, the cysteine free-thiol on the C-terminal of the peptide conjugate reacted with the vinyl-sulfone group on PEG-4VS or the acrylate group on PEG-4Acr.

To create 2.5% or 5% non-adhesive/non-degradable, PEG- KDWERC was reacted with PEG-4VS (to design non-degradable hydrogel) or (25% PEG-4VS with 75% PEG-4Acr to form a degradable gel). This reaction was created in a stoichiometric ratio of 2:1 in 30 mM HEPES buffer (pH 8.0). PEG-peptide were incubated at 37 °C, 5% CO₂ to allow gelation for 30-45 min prior to being placed in a culture medium or PBS. These PEG-peptide hydrogels were formed to perform rheological measurements and degradation assays.

2.3.3 Rheological measurements of hydrogels

The hydrogels 2.5% non-adhesive- non-degradable PEG-4VS and 75% PEG-4Acr were formed as described previously in (section 2.3.2). Briefly, hydrogels were formed at 50 µl volume using 8 mm sigmacoate glass rings (Sigma, SL2) cast on a 24-well plate (Greiner, BC017); rings were removed after gelation and placed in PBS (Sigma, P4474). Storage modulus G' was measured on a strain-controlled ARES from TA Instruments using an 8 mm plate with a 0.01-rad angle. Prior to performing measurements, PEG-peptide hydrogels were removed from the cell culture plate and placed onto the bottom rheometer plate. All measurements were carried out at 37 °C and sealed with paraffin oil to prevent evaporation. A frequency sweep was recorded, measuring G' as a function of shear frequency in 100–0.1 rad s⁻¹ at a fixed strain of 1%. (Orchestrator software, version 7.2.0.2). Rheology assessments were carried out on times after hydrogel formation 0, 72, 120, and 192 hours.

2.3.4 Tryptophan release quantification

Tryptophan cleavage in both hydrogels was quantified to measure hydrogel degradation. PEG-peptide hydrogels were formed as described, cast on 6 mm sigmacoate-treated glass rings (Sigma, SL2) on a 24-well plate (Greiner, BC017), and incubated at 37 °C, 5% CO₂ for 30-45 min to allow gelation. Next, glass rings were removed, and gels were submerged in cell culture media Dulbecco's Modified Eagle Medium (DMEM, Thermo Fisher Scientific, 11965092) and incubated at 37 °C, 5% CO₂. The degradation assay was assessed after hydrogel formation at 0, 72, 168, and 216 hours by measuring the absorbance of tryptophan in solution at 280nm.

2.3.5 hiPSC spheroids encapsulation in PEG-peptide hydrogel

hiPSC spheroids were harvested 48 hours post seeding in 96-wells V-bottom plate as (described in 2.2.1) (Figure 2.1). Before encapsulating, each well's spheroid was rinsed once and then resuspended with 30 mM HEPES buffer (PH 8.0) (buffer preparation described in section 2.3.2). PEG-peptide compositions were mixed at desired volume 10 µl, including spheroids and cast on 96-wellss V-bottom plate (Thermo Fisher Scientific, 268200) single spheroid per well for live imaging. Multiple spheroids were mixed with PEG-gel compositions and fabricated on µ-slides angiogenesis glass bottom (ibidi, 81507) for confocal imaging. PEG-peptide hydrogel, as mentioned previously, consists of 2.5% non-adhesive/non-degradable peptide conjugates PEG-KDWERC crosslinked with either (1) 100% PEG-4VS or (2) 25% PEG-4VS and 75% PEG-4Acr. The embedded spheroids were incubated for 30-45 minutes at 37° C, 5% CO₂ until gelation (after 20 minutes, samples were checked to see if gelation formed to avoid keeping cells without medium for a long time). Upon gelation, the medium was added in the presence of 10 µM ROCKi (ENZO Life Sciences, ALX-270-333-M005) (described in section 2.2.2) as follows: E8 medium, KSR with BMP4 (50 ng/ml), and controls E8 supplemented with 50 ng/ml BMP4, and KSR. Cells were cultured for 96 hours and incubated at 37 °C, 5% CO₂, with daily feeding.

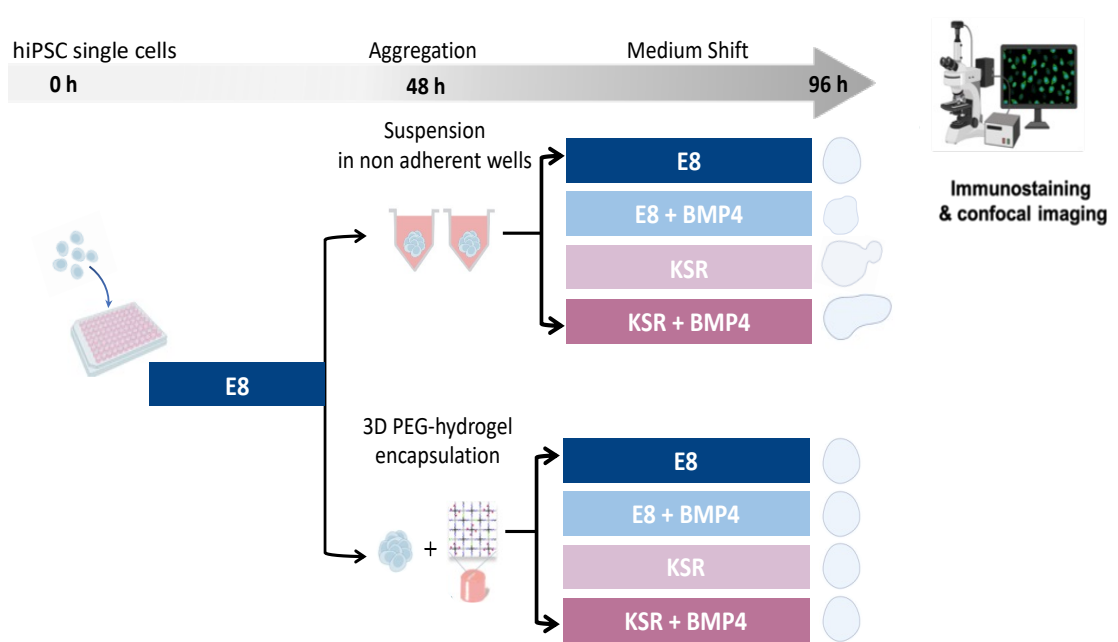


Figure 2.1 Schematic of experimental workflow.

hiPSC in single cells were seeded in low attachment plate 96- well V bottom cultured in E8 medium in suspension; after two days in culture (Top) medium was changed to E8, KSR BMP4, E8 BMP4 and KSR. (Bottom) hiPSC spheroids were encapsulated in PEG-4VS or PEG-4Acr hydrogels; after the hydrogels are fully crosslinked medium was changed to E8, KSR BMP4 medium or control conditions E8 BMP4 and KSR medium. Spheroids in both suspension and hydrogel were imaged using a live imaging microscope every hour for 96 hours, followed by immunostaining for stemness and differentiation markers and imaged using confocal.

2.4 Immunofluorescence labelling

2.4.1 Spheroids in suspension immunostaining

Spheroids in suspension were fixed using 4% paraformaldehyde (PFA) (Sigma) incubated at room temperature (RT) for 45 minutes on a shaker followed by three washes with PBS (Sigma, P4474) 5 minutes/wash. Cells were permeabilised and blocked with 0.3% Triton X100 (Sigma) in PBS (Sigma, P4474), and 3% bovine serum albumin (BSA, Sigma, A9418) for 1 hour at RT on a shaker. Primary antibodies were diluted in the blocking buffer, and spheroids were incubated in primary antibodies overnight in the dark at 4 °C on a shaker. Following three washes with 0.1% TritonX100 (Sigma) in PBS (Sigma, P4474) 5 minutes/wash, cells were incubated in secondary antibodies and DAPI for 2

hours at RT on a shaker. Finally, spheroids were washed three times with 0.1% TritonX100 (Sigma) in PBS (Sigma, P4474) for 10 minutes/ wash. All antibodies used to label spheroids in suspension in this thesis are listed in (Table 2.1). Controls for secondary antibodies only and DAPI to detect non-specific binding were performed for spheroids for each medium condition.

2.4.2 Cell proliferation assay

Spheroids in suspension at day 4 were labelled with 4 μ M EdU and incubated for 6 hours using a Click-iT EdU Alexa fluor 488 imaging kit (Thermo Fisher Scientific, C10337). Spheroids were fixed with 4% PFA (Sigma), incubated RT for 45 minutes on a shaker and washed three times with PBS (Sigma, P4474). Cells were then blocked and permeabilised using 3% BSA and 0.3% TritonX-100 (both Sigma) in PBS (Sigma, P4474) for 1 hour at RT on a shaker, followed by washing three times with 3% BSA (Sigma). Click-iT reaction buffer was prepared (following the manufacturer's instructions) at the desired volume. Cells were incubated in the reaction buffer for 30 minutes at RT on a shaker, followed by washing once with 3% BSA (Sigma). Nuclear staining, Hoechst 33342 (1:1000, Invitrogen) was added to the cells and incubated for 30 minutes at RT on a shaker protected from light. Then, cells were washed twice with PBS (Gibco) for 5 minutes/wash.

2.4.3 Embedded spheroids in PEG-peptide hydrogel immunostaining

Encapsulated spheroids in PEG-4VS and 75% PEG-4Acr were fixed with 4% PFA (Sigma) incubated at RT for 45 minutes on a shaker. Then, cells were washed three times with PBS (Sigma, P4474) for 10 minutes/wash followed by permeabilisation using 0.3% Triton X100 (Sigma) in PBS (Sigma, P4474) for 1 hour. Cells were incubated in a blocking buffer consisting of 0.1% TritonX100 (Sigma) and 3% BSA (Sigma) overnight at 4°C on a shaker. Primary antibodies were diluted in the blocking buffer; cells were stained and incubated for 36 hours in the dark at 4°C on a shaker. Following five extensive washes using 0.1% TritonX100 (Sigma) in PBS (Sigma, P4474) for 10 minutes/wash, cells were stained with secondary antibodies and DAPI overnight in the dark at 4°C with shaking. Then, cells were washed five times with 0.1% TritonX100 (Sigma) in PBS (Sigma, P4474) for 10 minutes/wash. All antibodies used to stain embedded 3D spheroids

in PEG-peptide hydrogels are listed in (Table 2.1). Secondary antibody only and DAPI were performed to detect non-specific binding.

2.4.4 Cell viability assay

A one-step cellular assay was used to detect live/dead cells post-hydrogel encapsulation. Live and Dead Cell Assay (Abcam, ab115347) was used to stain the spheroids embedded in PEG-peptide hydrogels after 96 hours in culture. Cells cultured in E8, KSR BMP4, E8 BMP4 and KSR medium were labelled with 1x live and dead dye to the medium. Spheroids in suspension were stained for live and dead as a control; cells were incubated for 10 minutes at 37 °C, 5% CO₂.

Table 2.1. Antibodies used for 3D spheroids immunostaining.

Antibody	Dilution		Manufacturer	Catalogue Number
	Suspension	PEG-gels		
Rabbit anti-OCT4	1:500	1:50	Abcam	ab19857
Goat anti-SOX17	1:100	1:50	R&D	AF1924
Goat anti-BRA	1:200	1:50	R&D	AF2085
Goat anti- SOX2	1:200		R&D	AF2018
Rabbit anti-EOMES	1:200		Abcam	Ab23345
Mouse anti-YAP1	1:50		Santa Cruz	sc-101199
Alexa Fluor 555 Phalloidin	1:100		Thermo Fisher Scientific	A34055
Donkey anti-rabbit Alexa Fluor 488	1:500	1:50		A32790
Donkey anti-goat Alexa Fluor 633	1:500	1:50		A21082
Donkey anti-mouse Alexa Fluor 594	1:500			A21203
DAPI	1:1000		Invitrogen	D1306

2.5 *Imaging and quantification*

2.5.1 Live cell imaging

Time-lapse imaging was performed at 37 °C, 5% CO₂ using JuLI™ Stage Real-Time Cell History Recorder (NanoEnTek). hiPSC -derived spheroids in 96-wells V-bottom plate in suspension and encapsulated in PEG-peptide hydrogels imaged every hour for 4 days (96 hours). Brightfield time-lapse images were acquired by 10x objective, using the following set-up: exposure time= 65 ms, brightness= 18, and focus at ~8851 to capture spheroids morphological changes over time. The setup could vary slightly between experiments which require some adjustment (i.e., focus and brightness).

2.5.1.1 Image analysis for time-lapse imaging of spheroids in suspension

A time-lapse image analysis pipeline was built to quantify spheroids' area and shape as morphological changes readouts. Firstly, raw images from the JuLI™ Stage Real-Time Cell History Recorder (NanoEnTek) were extracted from time points 1 to 96 before processing images in the segmentation pipeline. In this pipeline, the variation in pixel intensity values between the two following time points was calculated to distinguish values belonging to the spheroids area from the background. We observed the background as a constant area with no change in pixel intensity, whereas regions with pixel intensity variations were referred to as Delta images. Delta images were segmented using CellProfiler (Broad Institute) software. Principal Component Analysis using Spotfire High Content Profiler (Tibco, PerkinElmer) was used based on morphological parameters to cluster spheroids from different conditions and times. A full method description is included in this thesis as described in (Alsehli et al., 2021).

2.5.1.2 Computational neural networks for spheroids in suspension clustering

Here, data from CellProfiler were used to build a centroid of the images and these were included in a training set together with metadata of their medium condition (E8 versus KSR BMP4). The training and test sets were obtained from time-lapse data from time points 1-96. A proof-of-principle phenotypic classification was built using a trained convolutional neural network in collaboration with (Micrographia Bio, UK) that could

indicate with increasing accuracy over time the medium condition of a particular spheroid at a specific time-point as described in (Alsehli et al., 2021).

2.5.2 Confocal microscopy

2.5.2.1 Imaging of spheroids in suspension

After Immunofluorescence labelling as described in (section 2.4) spheroids in suspension culture were transferred into 96-wells plate, flat bottom, μ clear black for imaging (Greiner, 655090). Images for the selected markers and cell viability were acquired using Leica TCS SP8 confocal microscope with a 40x oil objective, Z-stack step size 5 μ m, 60 slices for spheroids cultured (E8 condition), and Z-stack step size 3 μ m for (KSR BMP4, E8 BMP4, and KSR) with a 40, 25, and 40 slices for each condition respectively.

2.5.2.2 Imaging of embedded spheroids in PEG-peptide hydrogel

Encapsulated spheroids in μ -slides angiogenesis glass bottom (ibidi, 81507) were imaged for markers expression and live/dead assay. Embedded spheroids were imaged with a 63x oil objective, and 20 slices were taken at Z-stack step size 2 μ m for all hydrogel conditions. Image processing was performed and visualised using ImageJ version 2.0.0 (Fiji) and OMERO.insight Version 5.5.9.

2.5.2.3 Image analysis

Image analysis for spheroids in suspension and encapsulated spheroids in hydrogels were performed using Imaris software version 9.9. Here, nuclei were quantified using spot-counting methods to determine the expression intensity of the germ layer, pluripotency, and cell proliferation markers. The percentage of positive expression was determined from the total number of cells in the DAPI channel for the respective spheroid. Co-localisation of OCT4 and SOX17 was calculated based on expression thresholds for co-expressed markers, and then spot detection was used to quantify the number of cells.

To measure sphericity after changes in morphology, a surface mask was created on the DAPI channel using Imaris software version 9.9. This surface mask was performed to select the spheroid region based on the DAPI threshold. This provides readouts for

changes in shape via sphericity and deformation values (values range closer to 1 corresponds to spherical structure, while values below 0.7 indicate shape deformation (Szymańda and Witkowski, 2021)).

2.5.2.4 Icy analysis pipeline

To analyse the F-actin distribution around the spheroids, a pipeline was created in Icy software (an open community platform for bioimage informatics) (de Chaumont et al., 2012). Pre-processing of the images included conversion into maximum intensity projections (MIP) and a gaussian blur to improve the segmentation quality of the whole spheroid area based on the DAPI channel and the F-actin network based on the F-actin channel. First, the two channels (DAPI and F-actin) were extracted separately (Figure 2.2). The DAPI channel was used for segmentation to detect the whole spheroid area using HK-means thresholding, creating a mask of the entire spheroid. Here, in the HK-means method, gaussian pre-filter (value =3) was used to remove noise, and the minimum object size was selected at 10000 pixels to generate a region of interest (ROIs) that represents the whole spheroid area.

As DAPI provides consistent and reliable staining, using this channel for mask creation improves the quality and reliability of segmentation and removes any bias due to changes in intensity in the F-actin channel. Next, A 'fill-holes in ROI' step was included to create a single mask that evenly covered the spheroid's whole area. Therefore, we determine our ROIs by dividing the entire area mask into an inner ring area (to measure F-actin within the centre of the spheroid) and an outer ring area (measuring F-actin within the periphery). To create these ROI, for each image, the whole area mask was reduced by a scale percentage of 25 along both the X and Y axis to reduce the ROI to the central region in the inner core. Next, the inner ROI was subtracted from the whole area mask to obtain the outer ring region. Reduction of each mask by a set scale percentage of 25 was chosen to remove bias and maintain as even as possible volume within each ROI. After identifying the ROI, the F-actin channel was used as input to extract the average intensity within each ROI area. The pipeline was run in an automated fashion to remove bias. Gastruloids with poor segmentation quality (if the whole mask value was greater than 1 ROI, due to fragmented gastruloids resulting in multiple masks) were excluded. To

quantify whether F-actin distribution is focused centrally (inner ring) or peripherally (outer ring), the ratio of average intensity (central: periphery) was calculated. The full pipeline is available in (Appendix 1).

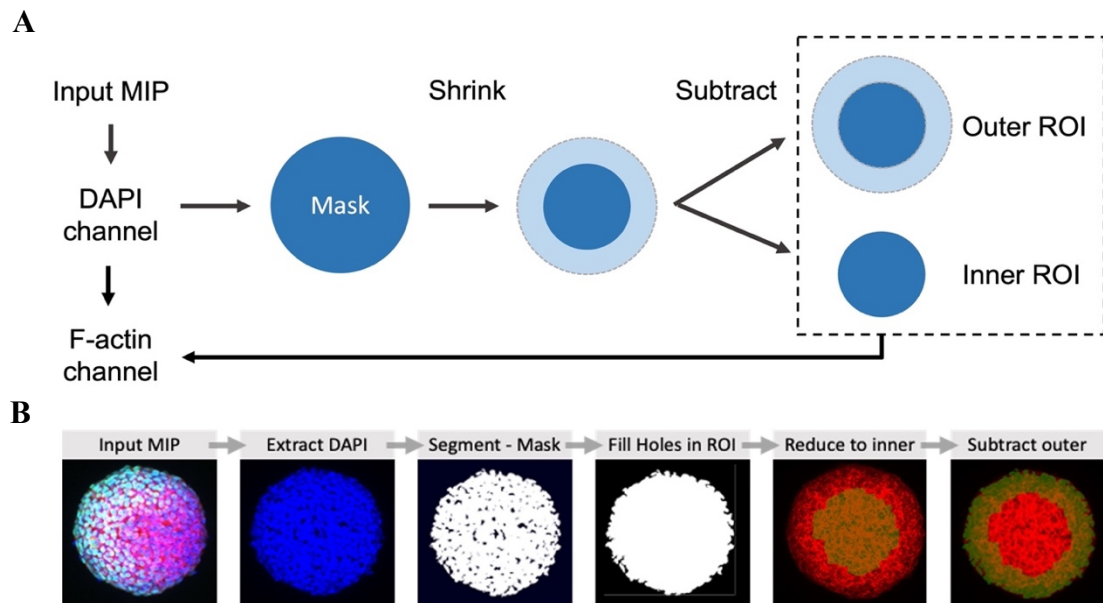


Figure 2.2 Overview of F-actin analysis pipeline.

A) Schematic of a method to extract the average intensity of F-actin in the periphery and centre of gastruloids. **B)** Example of output images of a spheroid after crucial steps of the analysis pipeline, displaying mask creation and ROI extraction. (*This pipeline was created by Errin Roy*).

2.6 Statistical analysis

Data from the live images pipeline and Imaris software were compiled into Microsoft Office 365 Excel 16.62. Data were exported to GraphPad Prism version 9.3.1., Results are represented as means with standard deviation (SD). Statistical analysis was performed via ordinary one-way ANOVA test for multiple comparisons (Šídák test) to analyse markers expression (OCT4, SOX17, SOX2, BRA and EOMES) between medium conditions. The F-actin data t-test was used, and one sample t-test was used for each hydrogel system to analyse degradability from days 0-5. To analyse cell viability after encapsulation between stiff or soft hydrogels, 2-way Anova test was used. Data sets with p values <0.0001, and < 0.05 are considered significant.

3 DISTINCT MORPHOLOGY IN 3D GASTRULATION-LIKE MODELS UNDER DIVERSE CULTURE CONDITIONS

3.1 Introduction

Self-organising in 2D systems such as hiPSC micropatterning models have been successfully used to recapitulate cell fate patterning and differentiation of three germ layers *ex vivo*. In these models, the presence of BMP4 morphogen was found to trigger pattern formation mirroring that in the early embryonic development (Warmflash et al., 2014, Deglincerti et al., 2016, Heemskerk and Warmflash, 2016). However, the capacity of morphogenesis renders 2D systems not fully adequate owing to the complexity of the *in vivo* microenvironment. 3D models, on the other hand, offer a more realistic opportunity to explore key features of gastrulation events inducing axial elongation and lineage specifications (Siggia and Warmflash, 2018, Simunovic and Brivanlou, 2017, Arias et al., 2022).

In this Chapter, I describe how I developed our proposed gastruloid-like model using hiPSC. Cells were seeded at defined density in low attachment 96-well plates and treated with BMP4 to form spheroids in suspension. Spheroids were then cultured in suspension in selected medium conditions as follows: (1) E8, (2) KSR BMP4 with controls, (3) E8 BMP4 and (4) KSR. The main aim of this Chapter is to characterise the dynamic changes of 3D hiPSC spheroids grown in self-renewing versus differentiating media conditions, giving rise to distinct morphologies. We set up for this purpose a robust high-content imaging-based platform to monitor morphology via live imaging and quantification methods.

This Chapter includes my first author publication without breaking the publisher's copyright in (section 3.3.2) <https://doi.org/10.1016/j.ymeth.2020.05.017>

3.2 *BMP4 signalling induces axial elongation in 3D gastrulation-like models*

We first set out to investigate whether 50 ng/ml BMP4 is sufficient to induce axial elongation in hiPSC-derived gastrulation 3D model in suspension. Defined cultured medium conditions (E8) that promote self-renewing and (KSR BMP4) triggers differentiation and their controls (E8 BMP4, and KSR) were used to explore spheroids phenotype behaviour in response to biochemical cues. Here, cells were plated in single cells 750 cells/well and cultured in E8 medium for 2 days to allow aggregation. Aggregates formed standardised spherical shape when cultured in 96- well V bottom plates before changing the medium to E8, KSR BMP, E8 BMP4, KSR and medium (Figure 3.1 A). After 96 hours in culture, live imaging revealed consistent phenotypic variations in each medium condition (Figure 3.1 B). Cells cultured in E8 medium formed a spherical shape, in KSR BMP4 medium spheroids were observed to break symmetry and exhibit axial elongation. The control conditions formed intermediate phenotypes, in E8 BMP4 spheres that were smaller in size and tended to form small protrusions while culturing in KSR alone exhibited a budded morphology.

Based on these observations (~230 spheroids) qualitative readouts showed 3D spheroids in E8 formed consistent round structures, whereas in KSR BMP4 medium most of the spheroids formed a long axis, few created a (budded structure)- defined as a small tip structure shaped out of the spheroid, and some remained sphere (Figure 3.1 C). In the intermediate conditions, the E8 BMP4 formulate spherical shaped structures (smaller in size when compared to E8 condition), while few tend to form a small-budded structure, however in KSR spheroids mostly created budded structures and few remained round (Figure 3.1 C). These observations are consistent with our previous findings in (Alsehli et al., 2021) which demonstrated a robust platform to detect morphological changes in each medium condition.

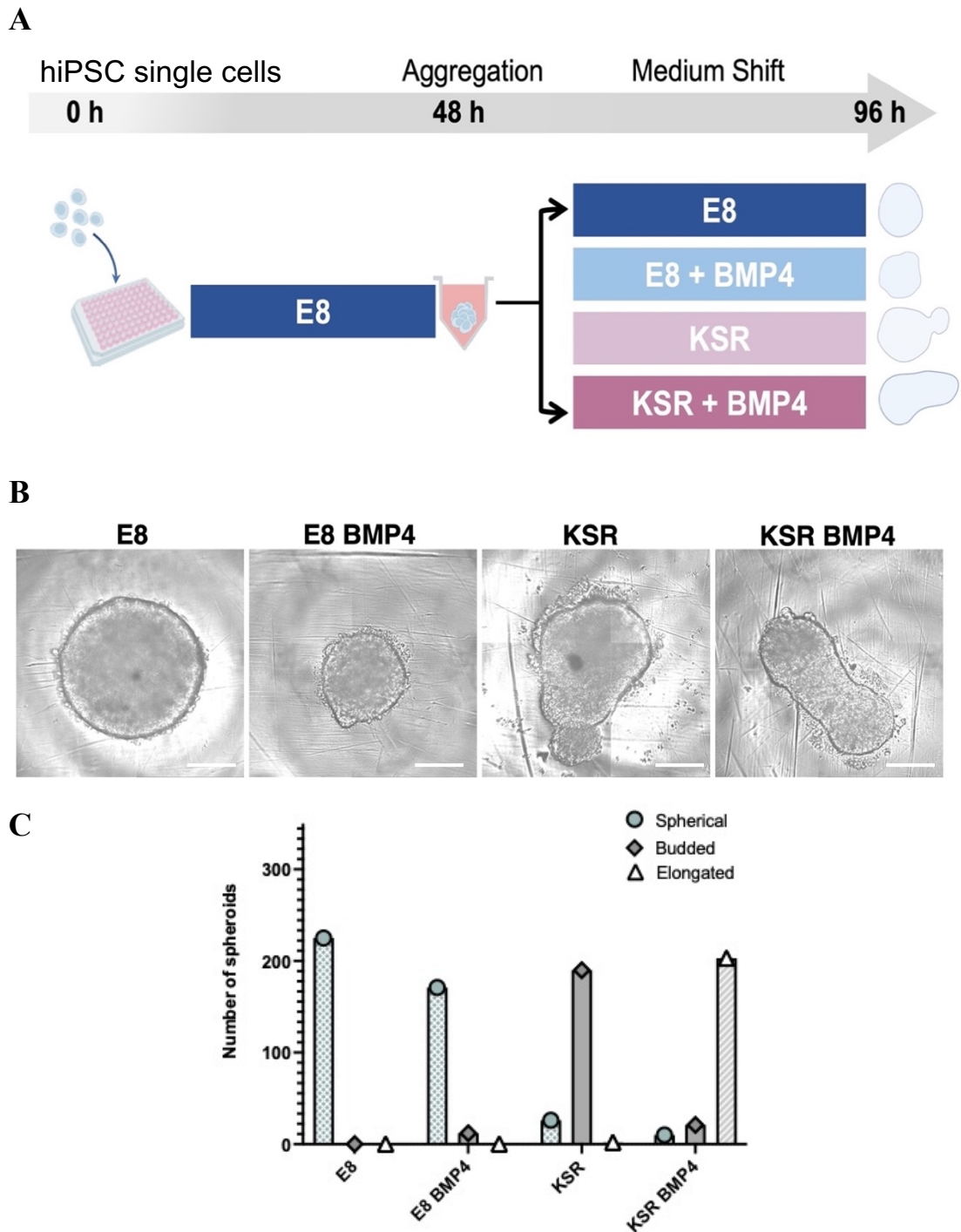


Figure 3.1 hiPSC forming a distinct morphology under diverse medium conditions.

A) hiPSC in single cells were seeded in low attachment plate 96- well V bottom cultured in E8 medium for 2 days to form aggregates, then the medium was changed to E8, KSR BMP4, E8 BMP4 and KSR. Scale bar 500 μm . **B)** The changes in spheroid shape, E8 medium maintained spherical shape, KSR BMP4 induced axial formation, in control conditions E8 BMP4 remains spherical, while KSR formed budded structure. **C)** Qualitative assessment of the dynamic morphological changes in each medium condition (total number of 230 spheroids).

3.3 *High-content image analysis*

Based on these results, we sought to develop image analysis pipelines that quantify changes in morphology using 3D endpoint images obtained from confocal microscopy and a series of time-lapse images acquired (2D) by live imaging microscopy. This allows for analysing the degree of deformation of the final shape (section 3.3.1) and the dynamic changes in morphology over time (section 3.3.2). Here, we propose methods of efficient spheroid area segmentation using Imaris and CellPofiler software.

3.3.1 Quantification of 3D hiPSC distinct variations under diverse culture conditions based on endpoint images

To identify how closely the shape of the 3D structure after 96 hours formed a perfect sphere or showed shape deformation, we used confocal images to measure the volume of the spheroid (Figure 3.2 A). Here, the segmentation of the spheroid area was created by surface mask based on DAPI channel thresholding to outline the whole spheroid area to allow for calculating sphericity values. The changes in morphology revealed that hiPSC spheroids cultured in E8 medium produce nearly perfect spheres with values laid between 0.7 to 0.9 representing a sphere-shaped structure (Figure 3.2 B). In the KSR BMP4 medium, the data showed fluctuations in shape values determined from 0.2 to 0.5 which indicates the massive deformation in shape when compared to the E8 medium (Figure 3.2 B). In the intermediate conditions, E8 BMP4 showed slightly diverse sphericity values hinting at less round structures in comparison to the E8 condition, whereas in KSR cells values are mostly 0.6- 0.7 rounded shapes (Figure 3.2 B). The existence of the budding structure in the KSR decreases the sphericity values to more intermediate structure. These data demonstrate the dynamic changes in spheroids morphology under diverse culture conditions in response to biochemical cues.

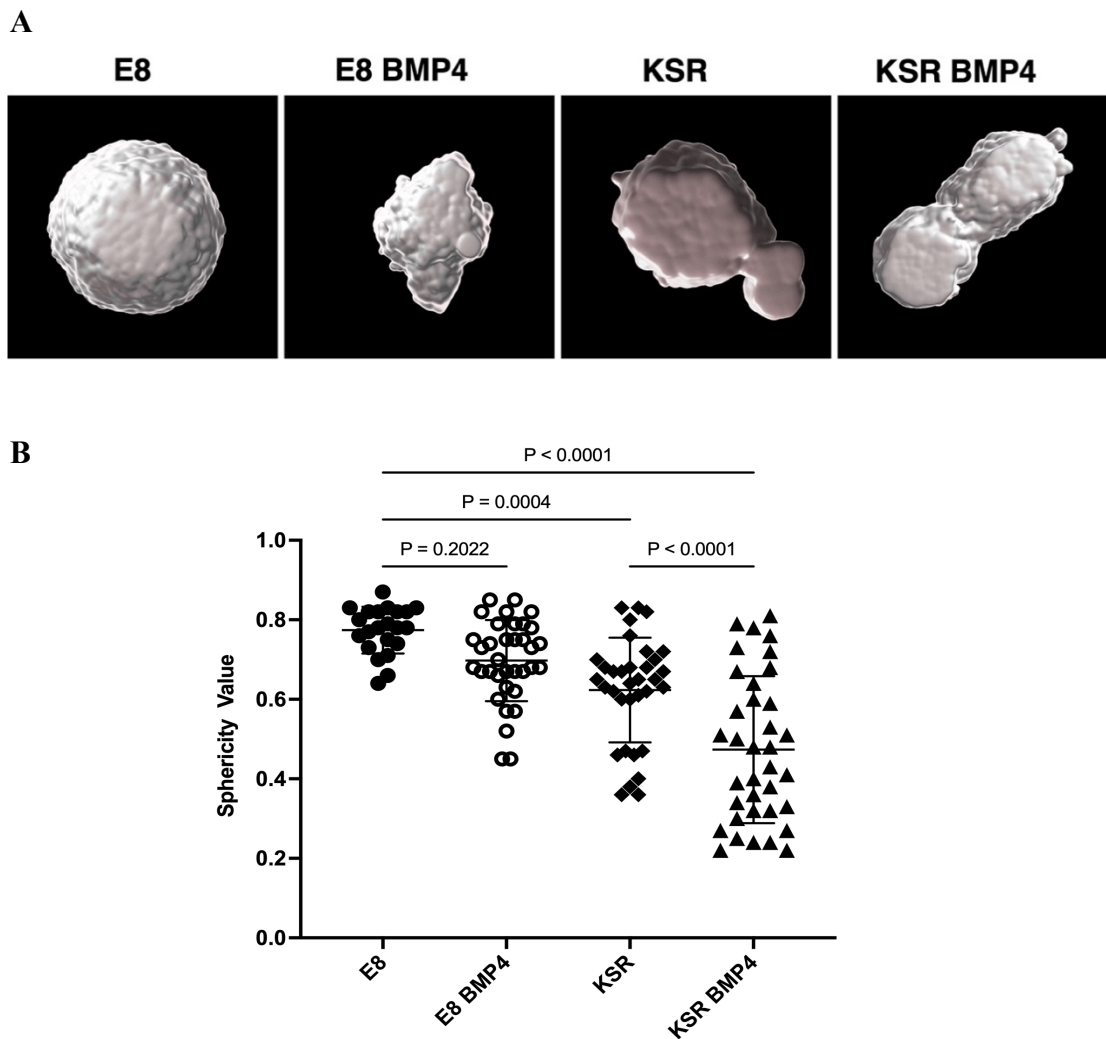


Figure 3.2 Quantification of morphological changes.

A) Confocal representative images of 3D culture masked using surface object tool via Imaris software. A surface mask of spheroid area was created based on the DAPI channel threshold to quantify deformation in shape. **B)** Sphericity values were obtained from the masked images, in E8 values are closer to 1 indicate a round shape, in KSR BMP4 value varies between 0.2 – 0.7 which demonstrates an elongated shape, E8 BMP4 and KSR exhibit substantial variation in sphericity values between rounded to deformed shape, statistic test ordinary one- way ANOVA (n=22, 36 spheroids in E8, and rest of conditions respectively, bars= SD)

3.3.2 An integrated pipeline for high-throughput screening and profiling of spheroids using simple live image analysis of frame to frame variations

Copyright for thesis incorporating publication

Elsevier's "As the author of this article, you are allowed to use it in your thesis and no formal permission is required. Please ensure to credit the original source."



Contents lists available at [ScienceDirect](https://www.sciencedirect.com)

Methods

journal homepage: www.elsevier.com/locate/jmeth



An integrated pipeline for high-throughput screening and profiling of spheroids using simple live image analysis of frame to frame variations

Haneen Alsehli^a, Fuad Mosis^{a,b}, Christopher Thompson^c, Eva Hamrud^{a,d}, Erika Wiseman^c, Eileen Gentleman^d, Davide Danovi^{a,e,*}

^a Centre for Stem Cells & Regenerative Medicine, King's College London, UK

^b National Heart and Lung Institute, Imperial College London, UK

^c Micrographia Bio, London, UK

^d Centre for Craniofacial and Regenerative Biology, King's College London, UK

^e Stem Cell Hotel, King's College London, UK

ARTICLE INFO

Keywords:

High content imaging
High throughput imaging
Cell phenotyping
3D
Spheroids
Stem cells

ABSTRACT

High-throughput imaging methods can be applied to relevant cell culture models, fostering their use in research and translational applications. Improvements in microscopy, computational capabilities and data analysis have enabled high-throughput, high-content approaches from endpoint 2D microscopy images. Nonetheless, trade-offs in acquisition, computation and storage between content and throughput remain, in particular when cells and cell structures are imaged in 3D. Moreover, live 3D phase contrast microscopy images are not often amenable to analysis because of the high level of background noise.

Cultures of Human induced pluripotent stem cells (hiPSC) offer unprecedented scope to profile and screen conditions affecting cell fate decisions, self-organisation and early embryonic development. However, quantifying changes in the morphology or function of cell structures derived from hiPSCs over time presents significant challenges. Here, we report a novel method based on the analysis of live phase contrast microscopy images of hiPSC spheroids. We compare self-renewing versus differentiating media conditions, which give rise to spheroids with distinct morphologies; round versus branched, respectively. These cell structures are segmented from 2D projections and analysed based on frame-to-frame variations. Importantly, a tailored convolutional neural network is trained and applied to predict culture conditions from time-frame images.

We compare our results with more classic and involved endpoint 3D confocal microscopy and propose that such approaches can complement spheroid-based assays developed for the purpose of screening and profiling. This workflow can be realistically implemented in laboratories using imaging-based high-throughput methods for regenerative medicine and drug discovery.

1. Description of theoretical basis and framework for the technique

Significant attention has been dedicated to the development of relevant cell culture models that can mirror the behaviour of human cells in vivo. Imaging methods are being deployed as important tools to analyse cells in complex environments in vitro [1]. This has interesting applications in the establishment of quality control protocols for therapeutics, as well as in cell therapy development and manufacturing. In particular, many systems are emerging that enable scientists to observe

and quantify cell patterning and the formation of 3D structures, such as spheroids [2]. These applications require the ability to acquire dynamic information over time and ideally perform on-the-fly analyses for quality control, screening and profiling campaigns [3].

High content analysis (HCA) approaches designed to obtain quantitative read-outs from microscopy images provide opportunities to derive automated multi-parametric data to quantify single cell behaviour and morphology. This information can be obtained from both live and endpoint image datasets [4]. There is a clear advantage in combining these two methods especially to study morphogenetic events. Indeed,

* Corresponding author at: Centre for Stem Cells & Regenerative Medicine, King's College London, 28th floor, Tower Wing, Guy's Hospital, Great Maze Pond, London SE1 9RT, United Kingdom.

E-mail address: davide.danovi@kcl.ac.uk (D. Danovi).

<https://doi.org/10.1016/j.jmeth.2020.05.017>

Received 28 February 2020; Received in revised form 5 May 2020; Accepted 15 May 2020

Available online 21 May 2020

1046-2023/© 2020 The Authors. Published by Elsevier Inc. This is an open access article under the CC BY license (<http://creativecommons.org/licenses/by/4.0/>).

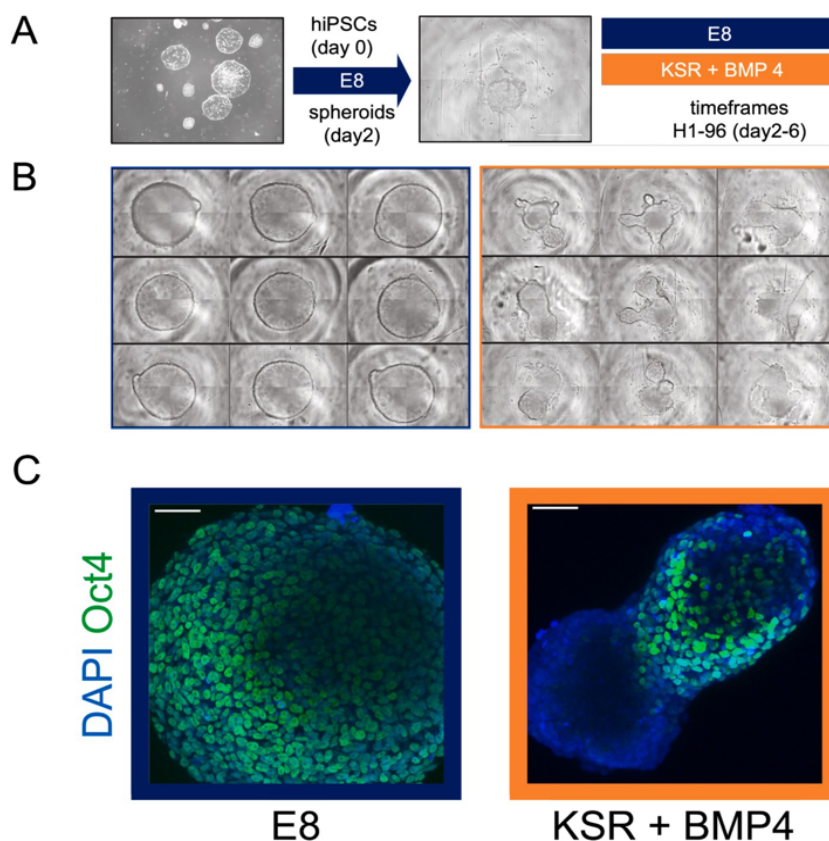


Fig. 1. Spheroids obtained from hiPSCs present consistent changes in morphology in different media conditions. (A) Scheme of this study – hiPSC (left) are plated in suspension. After 2 days medium is changed either maintaining in self-renewing E8 conditions or moved to differentiating KSR BMP4 conditions. Wells are imaged every hour from day 2 to day 6. Scale Bar, 500 uM. (B) Consistency of changes in shape – We observe formation of round or branched spheroids in the different media. Representative experiment at 96 h with $n = 9$ technical replicates. Images included are of spheroids in E8 (left) and KSR BMP4 conditions (right). (C) Endpoint confocal imaging – Representative spheroids at 96 h (endpoint day 6) imaged with confocal microscopy. Note the consistent shape changes in DAPI and staining of Oct4 pluripotency marker.

live imaging yields important time-dependent morphological information despite being more challenging to segment. On the other hand, endpoint images collected from cultures stained with dyes or immunofluorescent cell lineage markers tend to be easier to segment. Quantitative data can be processed via image analysis pipelines and workflows [5,6]. This approach enables scientists to explore cell dynamics, allowing for insights into biological and biochemical mechanisms in vitro [7,8].

Continuous improvements in microscopy and computation have effectively empowered high-throughput HCA from endpoint microscopy images in 2D. Nonetheless, trade-offs between content and throughput remain. In particular, quantifying changes in 3D morphology over time is potentially of great interest and yet generally operationally challenging in terms of set up, workflow, data storage and computation. Moreover, live 3D images from phase contrast microscopy tend to prove suboptimal and bring challenges to segmentation. More complex solutions with dyes, reporters and immunofluorescence have been explored and yet are harder to deploy for characterisation of large panels of human cell lines [9]. Furthermore, especially in complex cultures such as hiPSCs and primary cells, studies often focus on either live or endpoint imaging and are rarely combined [5,7].

hiPSCs have the ability to self-renew (producing identical daughter cells) and to differentiate into virtually all cell types of the human body. These cells offer promising applications for disease modelling and drug discovery. Analysing patterns of cells in vitro has the potential to provide insight into the mechanism of cellular behaviour, cell fate, and early embryonic development [10,11]. However, significant challenges in acquisition and analysis present when attempting to recapitulate self-organisation, cell fate patterning, and morphogenesis of early mammalian embryogenesis in vitro in 3D and in a dynamic manner

[12].

Multicellular aggregates called embryoid bodies (EBs) recapitulate some aspects of in vivo development and facilitate the understanding of cell fate dynamics and organisation [12,13]. More complex 3D approaches have provided robust simulation of in vivo gastrulation including symmetry breaking-like events prior to differentiation [14,15]. Methods have been described that dissect the molecular mechanisms involved in gastrulation in manageable in vitro systems that can be referred to as 2.5D [16]. Interesting examples have recently moved the field forward towards predictive modelling via in silico analysis [17]. These methods will have an important value in quality control of cells and could be exploited across a wide range of applications for regenerative medicine [1].

Our eyes effectively combine low resolution frame to frame variation for detection of movements with refined definition and colours. In fact, synergistic strategies have evolved in mammals that combine detection of movements in low lighting conditions (rods for peripheral vision) with higher resolution and colours (cones in the fovea). This combination can be modelled and has in fact been explored for specific purposes in other fields [18]. Similarly in concept, high content analysis strategies have been developed that couple screening lower magnification images with acquisition of a higher magnification images for regions of interest that satisfy defined criteria (see [19,20]).

Here, we report a method based on frame by frame subtraction, efficiently eliminating areas for which pixel intensities do not vary from frame to frame which in growing spheroids images correspond to the background. This pipeline refines segmentation by considering only the extracted pixels with changes in intensity values from one image to the other in subsequent timeframes. We analyse hiPSC in self-renewing versus differentiating conditions in 96-well plates. We demonstrate

that this method can successfully capture distinct morphology variations dependent upon biological conditions in a scalable and high-throughput manner. We demonstrate the value of this approach and propose it can be applied to a range of cell systems presenting similar challenges.

2. Materials and methods

2.1. Human iPSCs culture

As described [21] 6-well plates were coated with 4% Vitronectin (STEMCELL Technologies) diluted in Phosphate Buffered Saline (PBS, Sigma). Cells were cultured in feeder-free Essential 8 (E8, ThermoFisher) with 2% supplement according to manufacturer's instructions, and 1% (5000U/ml) Penicillin/Streptomycin (Pen/Strep, Gibco). Cultures were medium-changed daily and passaged every 4 days at approximately 80% confluence. hiPSCs colonies are washed with Hank's Balanced Salt Solution (HBSS), incubated with Versene cell dissociation solution (Gibco) for 3–4 min at 37 °C, 5% CO₂ and resuspended in E8 medium in 6-well vitronectin-coated plates. The hiPSC cell line Hoik_1 was obtained from the HipSci biobank (www.hipsci.org) [21].

2.2. Preparation of 96 well V-bottom plates

Before dissociating hiPSCs colonies into single cells and seeding in 96 well V-bottom plates, hiPSCs were observed visually to confirm that they had not undergone spontaneous differentiation as this will affect the spheroid formation and differentiation. To pre-treat the 96 well V-bottom plates, 50 µl of 5% pluronic solution were added before centrifugation for 5 min at 500 × g, to ensure the plate is free of bubbles. If bubbles remain we suggest to centrifuge again at higher speed or maximum speed for an additional 5 min. Incubation at RT for 1 h was followed by washing with PBS and addition of 50 µl of E8 medium with 10 µM Y-27632 Rho-kinase inhibitor (ROCKi, ENZO Life Sciences) to each well to avoid drying. This prevents hiPSCs from adhering to the plate and promotes spheroid formation. Note that for the 96 well V-bottom plate layout of this experiment, cells in E8 condition were plated in columns 1–3 whereas cells in KSR-BMP4 condition were plated in columns 10–12. Results in Fig. 1 are from a representative experiment with n = 9 technical replicates. Over 3 biological replicates have been obtained with these conditions in parallel.

2.3. Spheroid formation

Cells were washed with HBSS (Gibco), colonies dissociated into single cells by incubating them for 4 min in Accutase (BioLegend) at 37 °C, 5% CO₂. Single cells were resuspended in E8 and 10 µM ROCKi. Prior to cell seeding, 96 well V-bottom plates (ThermoFisher Scientific) were coated with 5% (w/v) Pluronic solution (Sigma) for 1 h. In these ultra-low adherence conditions, cells were seeded at a density of 750 cells/well in 96 well V-bottom plates, incubated at 37 °C, 5% CO₂ in E8 and 10 µM ROCKi and left for 24 h to allow cell aggregation. Following another 24 h of culture in E8 medium, hiPSCs cluster and form aggregates. Medium was then replaced with different medium conditions in the presence of 10 µM ROCKi as following: Self-renewing conditions: E8 medium and 1% Pen/Strep; Differentiating conditions: Knock Out Serum Replacement medium (KSR) consisting of Advance DMEM/F-12 medium, supplemented with 20% KnockOut serum replacement, 1% L-Glutamine, 1% Penicillin Streptomycin (5000U/ml) (all Gibco), 0.1 mM β-mercaptoethanol (Sigma), 10 ng/ml basic fibroblast growth factor (bFGF) (Invitrogen) supplemented with 50 ng/ml BMP4 (Invitrogen) morphogen. Culture medium was changed after 48 h once the spheroids formed to the following medium conditions all in the presence of 10 µM ROCKi; E8 medium, and KSR supplemented with (50 ng/ml) BMP4. Subsequently, hiPSCs spheroids were monitored for 96 h using a JuLI™ Stage live imaging microscope in a controlled environment at 37 °C and 5% CO₂ inside a tissue culture incubator. The plate was spun down for

30 s at 200 × g after medium replacement as described in the previous step, to bring all spheroids to the bottom of the plate in the centre of V-bottom wells.

2.4. Immunostaining and comparison with end-point analysis

After 96 h, spheroids were fixed using 4% paraformaldehyde (PFA) for 45 min at RT, and washed three times with PBS. Cells were permeabilised with 0.3% Triton X100 in PBS for 1 h at RT, followed by blocking with 5% donkey serum in PBS for 1 h at RT. Primary anti-Oct4 antibody (Abcam) at (1:500) was diluted in 5% donkey serum in PBS and incubated overnight at 4 °C. After three washes with PBS, secondary antibody donkey anti-rabbit Alexa Fluor 488 at (1:500) (Invitrogen), and DAPI at (1:5000) were added and incubated for 1 h at RT in the dark. Spheroid images were acquired using Leica TCS SP8 Confocal laser scanning microscope with a 40x oil objective. Confocal images were analysed in Columbus (Perkin Elmer). Maximum projection for each channel were merged into one image (Calculated Image) smoothed with a Gaussian filter. The resulting image was used to create a mask of the whole organoid (Image Region) and the morphological properties such as area and width to length ratio were measured from these masks. We used proprietary software exclusively to validate the consistency of morphological changes in the spheroids when imaged in more cumbersome endpoint 3D images.

2.5. Live imaging

Images of spheroids were obtained by acquiring every hour for 96 h. We tiled 4 fields at 10x objective using the JuLI™ Stage Real-Time Cell History Recorder (NanoEnTek). To image all 96 wells in our conditions takes 18 min. The total time of 96 h (4 days) is calculated for every cycle (1 h). In other words, 96 cycles are acquired in parallel with a shift in time of up to 18 min. Thus, the interval time is calculated for each well and the monitoring of spheroid growth for each well can be considered independent. The difference in time for acquisition of neighbouring fields within the same well is negligible as an entire well is imaged in under 12 s. Selection of the image position is nonetheless critical as it is necessary to ensure that spheroids will be imaged for 96 h. We typically define the central position of the 2 × 2 fields within the well within ample margins accounting for the maximum expected spheroid growth in the following 96 h based on previous experiments. These conditions can be modified for other specific spheroids monitoring needs, other devices and different image acquisitions. Importantly, image acquisition set up (focus, time exposure, and level of brightness) may also vary slightly from one experiment to another and adjustment of focus, brightness level and exposure time are recommended. It is worth noting that this analysis applies to imaging spheroids in transparent material suspension and is more challenging in situations in which this is not the case. Because the image analysis pipelines in this study are based on Delta images as detailed below, we recommend choosing the time-frame intervals that effectively capture growth. In other words, if spheroids growth is not detectable in successive timepoints, longer time intervals should be considered.

2.6. Image analysis and segmentation

The image analysis pipeline was created to analyse spheroids' area and shape using CellProfiler (Broad Institute) software [11]. Initially, raw images are extracted from timepoint 1 to 96, then these images are tiled, batch-loaded and processed using the segmentation pipeline. Here, the differences in pixel intensity values between consecutive images are calculated to identify those that are static. Areas that largely do not change pixel intensities value belong to the background and not the growing spheroid. A subtraction (Delta) is thus performed on every pixel of two consecutive timepoints images. A difference of 0 highlights no change in pixel intensity and therefore no movement between the two

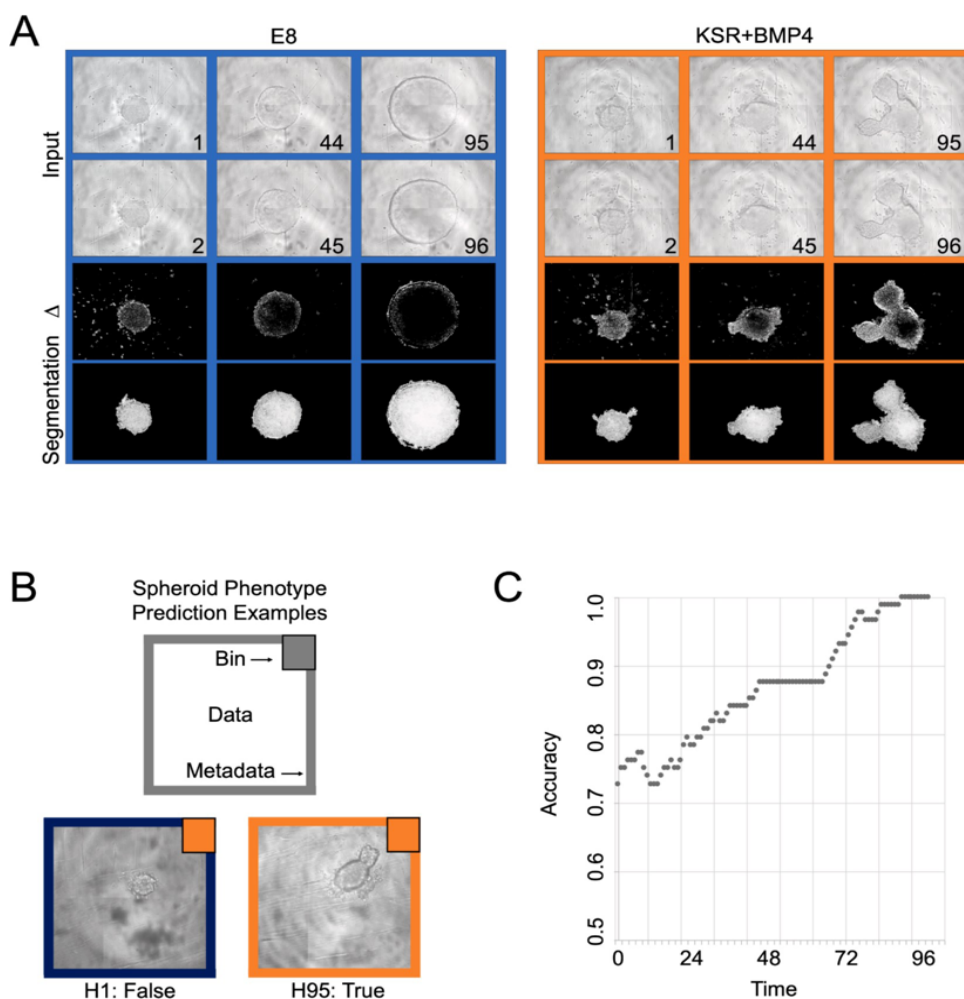


Fig. 2. Exploiting live images' frame-to-frame variations to improve segmentation and automated analysis with computational neural networks. (A) Representative images of spheroids cultured in E8 and KSR+BMP4 media at the beginning (1–2 h), middle (45–46 h), and end (95–96 h) of the observation period. The image Delta is produced by subtraction of pixel intensities: note that background halos surrounding the spheroids are effectively removed with this strategy. Segmentation is obtained from the Delta images via a dedicated CellProfiler pipeline (see Appendix 1 for details). Scale Bar, 500 um. (B) colours refer to prediction (top right square) and actual condition (frame); one early timepoint example is inaccurately classified, whereas one late timepoint example is correct. (C) A tailored Convolutional Neural Network is trained and used to predict Spheroid Phenotype Classification in two classes based on metadata of the medium conditions used. The graph shows phenotype prediction accuracy (rolling average over 10 h) over time increasing at later timepoints.

time frames, which is classified as the background. Any differences above 1 are classified as a moving spheroid and used to generate the Delta image series. The resultant cell area in this processed Delta image series is segmented to quantify changes in morphology. We then expand the pixels that make up the spheroids as detailed in Appendix 1 (step-by-step description of the CellProfiler pipeline). The rationale is similar to methods described by others [22]. In order to evaluate whether quantitatively, the values of features extracted from our pipeline could be used to cluster spheroids from these two conditions, we performed Principal Component Analysis using Spotfire High Content Profiler (Tibco, PerkinElmer) on individual spheroids imaged over a 96 h time course (see Appendix 2B for the list of morphological features considered).

2.7. Spheroid phenotype classification

Images are squared and centred by cropping on the width dimension,

using the centroid of the segmented Delta mask as the focal point for each stored image. Data is preprocessed by defining two simple bins based on metadata obtained from the medium conditions: E8 versus KSR+BMP4. The classification model accepts a batch of single-channel grayscale processed images with dimensions of (batch, 1, height, width) and outputs the softmax probability of spheroid type (rounded or branched). The model network is setup as follows. ResNet18 was selected as the backbone of the spheroid classification model, as it has been well-characterised and is available from the PyTorch model module [23]. The ResNet architecture accepts 3-channels RGB images. To accommodate our single channel grayscale images into this architecture, a single 2D convolutional layer was implemented in between the input and ResNet structure. This layer served to expand the input tensor from 1-channel to 3-channels, creating an artificial “RGB” image for input into ResNet. The output layer of ResNet18 was amended to output 2 possible classifications, instead of 1000. Total experiment dataset includes 36 wells, of 96 timepoints each, broken equally among the

treatment groups. Datasets for training and evaluation were broken up as follows. A held-out evaluation set was composed of the images from four complete wells from each treatment group (~20% of total samples), selected at random. The training set was composed of the remaining wells from each treatment. For training, standard augmentation was used (random flip, random crop, and resize). Cross-entropy against the binary classification for each image was computed as the loss function, and the ADAM optimiser was used for backpropagation. The model weights were checkpointed regularly and each checkpoint model was evaluated against the held-out evaluation set without augmentation or dropout regularisation. Importantly, the evaluation set was composed of images derived from wells completely excluded from the training set to prevent overfitting via timepoints directly before or after that would have existed in the training set.

3. Results

3.1. Spheroid formation

Distinct cellular behaviour is observed in the different medium conditions for 3D spheroids (Fig. 1A). In essence, hiPSCs spheroids cultured in KSR+BMP4 medium elongate in shape producing budding and branches. Conversely, cell structures in E8 medium grow to form larger, round spheroids. These structures stain positively for pluripotency marker Oct4 as observed under confocal microscopy (Fig. 1C). The majority of cells are Oct4 positive in round spheroids from E8 conditions whereas only a minority of cells remain pluripotent in KSR+BMP4 conditions and are typically localised in the ‘neck’ of the budding regions. Examples of the shape parameters obtained for these structures from confocal microscopy images are included indicating changes in spheroid morphology parameters (Appendix 2A).

3.2. Image analysis

Having consistently observed such morphologies in structure from these diverse conditions in endpoints, we set to evaluate whether simple live imaging could be used instead of confocal endpoint analysis. To quantify the phenotypic features variations over time, including size and shape of hiPSCs we developed a dedicated image analysis workflow within the framework of the open source CellProfiler software [11]. An image series, termed Delta, was generated by quantifying the differences in pixel intensity values of consecutive images within a time frame. This strategy efficiently subtracts the background from one image to the other (Fig. 2A). Morphological features from the segmented regions, such as area and form factor, were captured for each timepoint and Principal Component Analysis of all features is shown over time (Appendix 2B). This indicates that as time progresses from 1 h to 96 h the spheroids diverge presenting specific morphological parameters. Altogether these observations prompted us to explore whether the information retained with simple microscopy over time would be sufficient to predict using an automated approach the conditions of culture of the specific spheroid. We used the Delta segmentation images to guide cropped box-shaped image datasets and trained a convolutional neural network by presenting images assigned to two bins of round/E8 versus branched/KSR+BMP4 cell structures. Examples of predicted erroneous and correct classifications are given (Fig. 2B, insets). Confusion is present in early timepoints which appear to be almost random. Conversely, the binning gradually becomes more accurate as the morphology of the

spheroids in the diverse medium conditions becomes more distinct over time (Fig. 2C).

4. Conclusion

We propose a novel method to exploit frame to frame variation for efficient segmentation of simple phase contrast microscopy for live 3D spheroids. This increases significantly the speed and hence the throughput compared to existing strategies based on analysis of endpoints. A CellProfiler based pipeline is coupled with a trained convolutional network to predict distinct media conditions analysing morphology. This self-contained method is validated by unsupervised clustering using principal component analysis and by comparison with 3D confocal microscopy. In this study, spheroids are obtained from hiPSCs. A broad range of application across diverse cell systems in regenerative medicine and drug discovery can be pursued. We recommend such approaches can be immediately adapted and efficiently implemented by laboratories using imaging-based high-throughput methods.

CRedit authorship contribution statement

Haneen Alsehli: Conceptualization, Data curation, Formal analysis, Funding acquisition, Investigation, Methodology, Project administration, Validation, Visualization, Writing - original draft. **Fuad Mosis:** Conceptualization, Funding acquisition, Methodology, Software. **Christopher Thompson:** Software. **Eva Hamrud:** Data curation, Visualization. **Erika Wiseman:** Data curation, Formal analysis, Visualization. **Eileen Gentleman:** Supervision. **Daide Danovi:** Conceptualization, Funding acquisition, Methodology, Project administration, Resources, Supervision, Writing - original draft, Writing - review & editing.

Acknowledgements

HA and DD wish to acknowledge the Ministry of Education in Saudi Arabia for the PhD studentship and funding by the Saudi Arabian Cultural Bureau in the UK. FM and DD acknowledge support from IBIN, a Technology Touching Life initiative funded by the Medical Research Council. EH, EG and DD wish to thank the Advanced Therapies for Regenerative Medicine PhD Programme generously supported by Wellcome. We are grateful to the Wellcome Trust and MRC for funding through the Human Induced Pluripotent Stem Cell Initiative (WT098503). We also gratefully acknowledge funding from the Department of Health by the National Institute for Health Research comprehensive Biomedical Research Centre award to Guy’s & St Thomas’ National Health Service Foundation Trust in partnership with King’s College London and King’s College Hospital NHS Foundation Trust. The views expressed are those of the author(s) and not necessarily those of the NHS, the NIHR or the Department of Health or all other funders. The authors wish to acknowledge Anne Carpenter’s team for the seminal development of Cell Profiler as an open source software to the scientific community; Craig Russell, Paula Gomez and Mike Shaw at the National Physics Laboratory for discussions; Zuming Tang, Errin Roy and Alice Vickers for technical support and discussions; Tung-Jui Trieu and Joana Pereira das Neves for collaborative work within the King’s Together funded Guthop initiative.

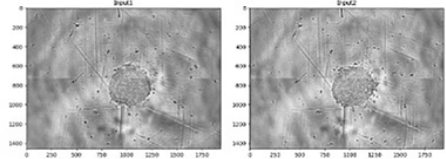
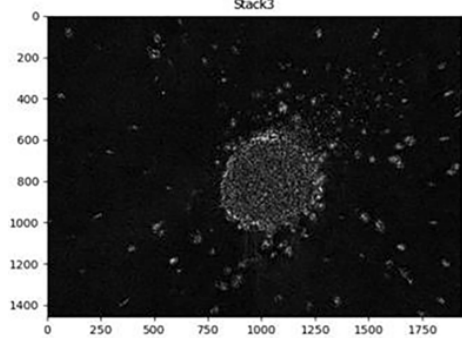
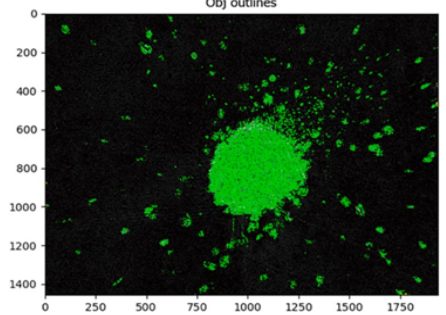
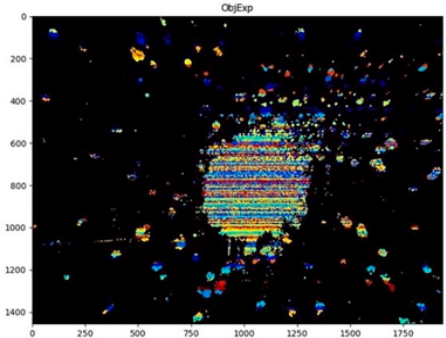
Appendix 1. Detailed CellProfiler pipeline

Step-by-step description of the CellProfiler pipeline modules to facilitate application of the described strategy to specific readers needs.

DISTINCT MORPHOLOGY IN 3D GASTRULATION-LIKE MODELS UNDER DIVERSE CULTURE CONDITIONS

H. Alsehli et al.

Methods 190 (2021) 33–43

Module	Function	Purpose	Output
i. Primary analysis			
Image math	Calculates absolute difference in pixel intensity between each frame and the following frame to generate a new set of images.	Filters out all pixels defined as background, with no change in intensity from each frame to the following frame in the stack.	
Save images	Exports images as a new stack (Delta) for further analysis.	Exports a new set of images as a stack (Delta) that can be analysed.	
Identify primary objects	Filters out objects to only retain those between 1 and 5000 pixels via thresholding.	Identifies objects (areas of pixels intensities that make up the spheroid).	
Expand or shrink objects	Expands each object by 2 pixels.	Allows all objects including the ones that make up the spheroid to be in contact with each other.	

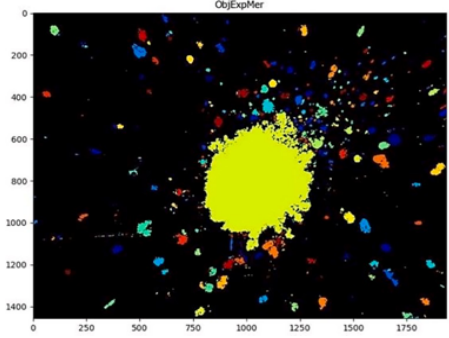
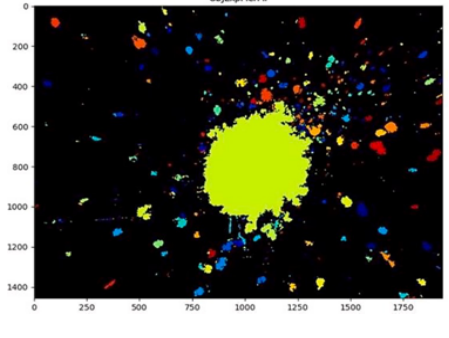
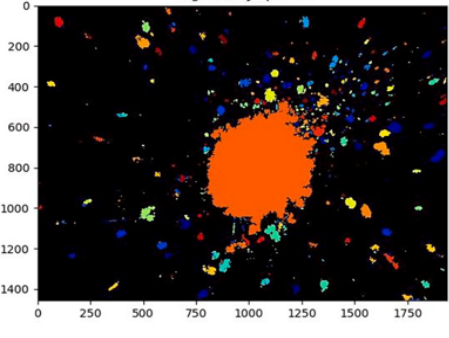
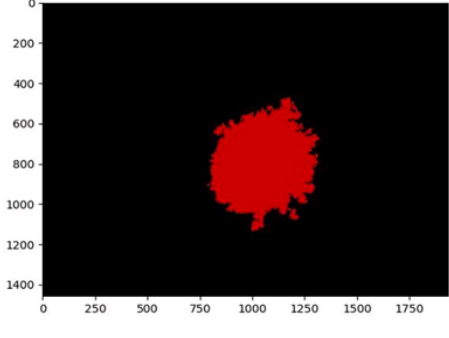
(continued on next page)

DISTINCT MORPHOLOGY IN 3D GASTRULATION-LIKE MODELS UNDER DIVERSE CULTURE CONDITIONS

H. Alsehli et al.

Methods 190 (2021) 33–43

(continued)

Module	Function	Purpose	Output
Split or merge objects	Merges all objects that are in contact with each other (i.e. have a distance in pixels of 0).	Transforms all small objects that make the spheroid into a single object.	
Fill objects	Holes smaller than an area of 800 pixels will be filled.	Fills up left-over holes within the object (spheroid).	
Measure object size shape	Identifies the size of all objects.	Identifies the size of all remaining objects in the field, including the spheroid.	
Filter objects	Removes all objects with an area of less than 60,000 pixels.	Filters out anything not large enough to be a spheroid.	

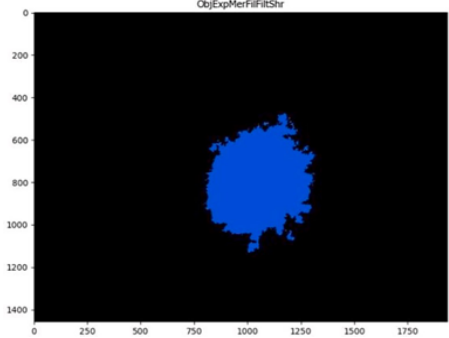
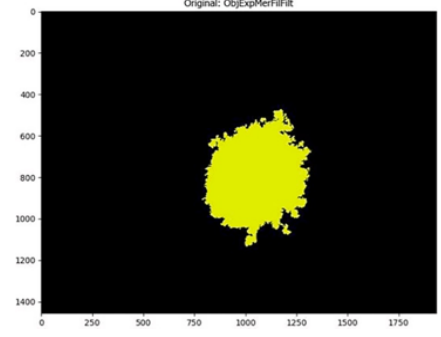
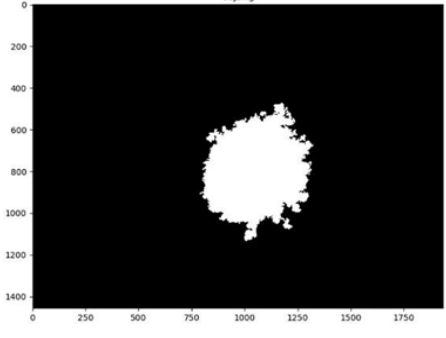
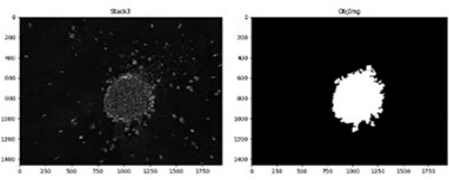
(continued on next page)

DISTINCT MORPHOLOGY IN 3D GASTRULATION-LIKE MODELS UNDER DIVERSE CULTURE CONDITIONS

H. Alsehli et al.

Methods 190 (2021) 33–43

(continued)

Module	Function	Purpose	Output
Expand or shrink objects	Shrinks object by 2 pixels.	Returns the edge of the spheroid to its original size after initial 2-pixel expansion.	
ii. Extract features Measure object size shape	Measures the morphology properties of the object.	Measures features of object (spheroid), e.g. area, form factor.	
Export to spreadsheet	Exports measurements to a spreadsheet for analysis.	Allows subsequent analysis of exported values for desired features.	
iii. Extract segmented spheroid stack Convert objects to image	Converts object to an image, generating a stack of binary spheroid (termed Binary).	Generates an image from the object (currently a binary form) to extract spheroid from Delta stack.	
Image math	Calculates absolute difference in pixel intensity between each frame of Delta against Binary, which generates a set of images of background frames (termed Background).	Uses Binary spheroid image stack to remove spheroid from Delta, thus creating a stack containing only the Background from Delta.	

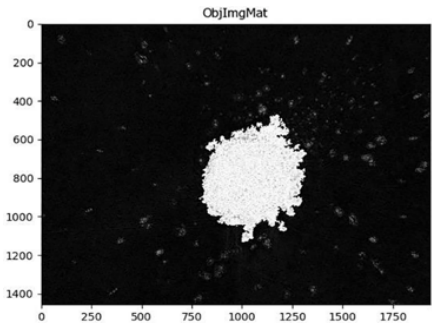
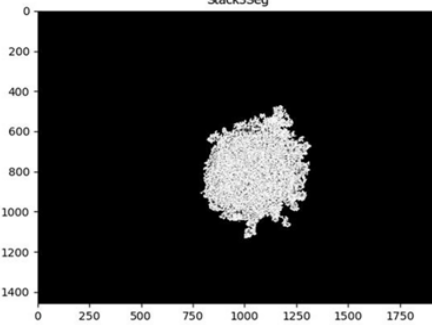
(continued on next page)

DISTINCT MORPHOLOGY IN 3D GASTRULATION-LIKE MODELS UNDER DIVERSE CULTURE CONDITIONS

H. Alsehli et al.

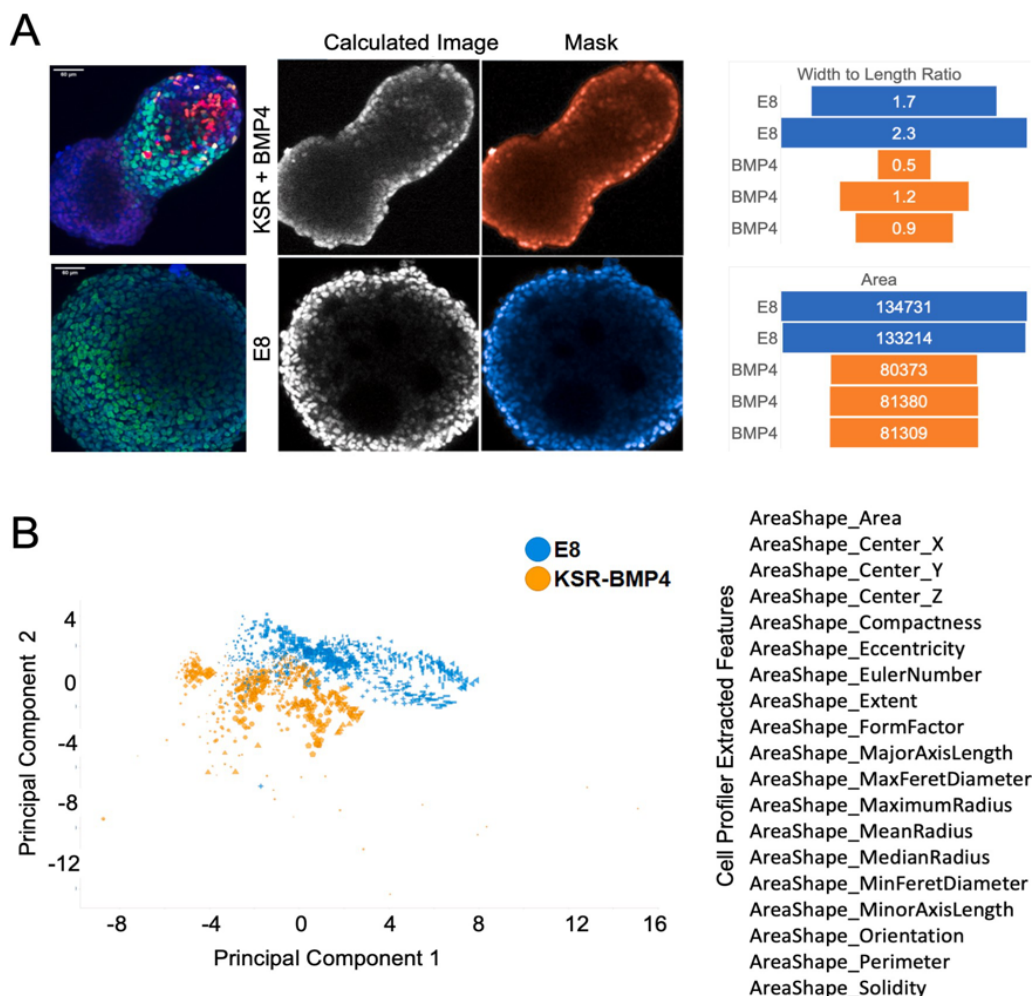
Methods 190 (2021) 33–43

(continued)

Module	Function	Purpose	Output
Image math	Calculates absolute difference in pixel intensity between each frame of Delta and Background to generate a set of images (termed Segmented).	Removes background of spheroid from Delta, and generates a stack of images with a completely segmented spheroid.	
Save images	Exports Segmented as a stack.	Exports Segmented stack to be subsequently analysed.	

CellProfiler pipeline and example dataset included in Supplementary.

Appendix 2. Validation with proprietary software



Validation of morphology change in endpoint (Columbus) (A) For the examples images in Fig. 1B, Maximum projection DAPI staining is segmented with Columbus as Mask from Calculated Image. Morphological parameters Width to Length Ratio (top) and Area (bottom) are shown for representative spheroids analysed to highlight and quantify morphological differences between conditions. (B) Validation of morphology features value change (Spotfire High Content Profiler, Tibco, PerkinElmer). Multidimensional reduction on morphology features extracted from live image analysis through the CellProfiler pipeline allows separation of spheroids based on the different conditions. Principal Component Analysis for segmented images at each timepoint for E8 (blue) or KSR+BMP4 (orange). Size of the data points represents time; shape represents different wells. Unsupervised clustering based on morphology parameters becomes apparent after several hours.

Appendix 3. Supplementary data

Supplementary data to this article can be found online at <https://doi.org/10.1016/j.ymeth.2020.05.017>.

References

[1] P. Horvath, N. Aulner, M. Bickle, A.M. Davies, E.D. Nery, D. Ebner, M.C. Montoya, P. Ostling, V. Pietiainen, L.S. Price, S.L. Shorte, G. Turcatti, C. von Schantz, N. O. Carragher, Screening out irrelevant cell-based models of disease, *Nature Reviews Drug Discovery* 15 (11) (2016) 751–769, <https://doi.org/10.1038/nrd.2016.175>.

[2] S. Vianello, M.P. Lutolf, Understanding the mechanobiology of early mammalian development through bioengineered models, *Developmental Cell* 48 (6) (2019) 751–763, <https://doi.org/10.1016/j.devcel.2019.02.024>.

[3] N. Carragher, F. Piccinini, A. Tesi, O.J.T. Jr, M. Bickle, P. Horvath, Concerns, challenges and promises of high-content analysis of 3D cellular models, *Nature Reviews Drug Discovery* 17 (8) (2018) 606, <https://doi.org/10.1038/nrd.2018.99>.

[4] M. Mattiazzi Usaj, E.B. Styles, A.J. Verster, H. Friesen, C. Boone, B.J. Andrews, High-content screening for quantitative cell biology, *Trends in Cell Biology* 26 (8) (2016) 598–611, <https://doi.org/10.1016/j.tcb.2016.03.008>.

[5] D. Danovi, A. Folarin, S. Gogolok, C. Ender, A.M.O. Elbatsh, P.G. Engstrom, S. H. Stricker, S. Gargica, A. Georgian, D. Yu, K.P. U, K.J. Harvey, P. Ferretti, P. J. Paddison, J.E. Preston, N.J. Abbott, P. Bertone, A. Smith, S.M. Pollard, A high-content small molecule screen identifies sensitivity of glioblastoma stem cells to

DISTINCT MORPHOLOGY IN 3D GASTRULATION-LIKE MODELS UNDER DIVERSE CULTURE CONDITIONS

H. Alsehli et al.

Methods 190 (2021) 33–43

- inhibition of polo-like kinase 1, *PLOS One* 8 (10) (2013) e77053, <https://doi.org/10.1371/journal.pone.0077053>.
- [6] E. Wiseman, A. Zamuner, Z. Tang, J. Rogers, S. Munir, L. Di Silvio, D. Danovi, L. Veschini, Integrated multiparametric high-content profiling of endothelial cells, *SLAS DISCOVERY: Advancing the Science of Drug Discovery* 24 (3) (2019) 264–273, <https://doi.org/10.1177/2472555218820848>.
- [7] S. Singh, A.E. Carpenter, A. Genovesio, Increasing the content of high-content screening: an overview, *Journal of Biomolecular Screening* 19 (5) (2014) 640–650, <https://doi.org/10.1177/1087057114528537>.
- [8] J.C. Caicedo, S. Cooper, F. Heigwer, S. Warchal, P. Qiu, C. Molnar, A.S. Vasilevich, J.D. Barry, H.S. Bansal, O. Kraus, M. Wawer, L. Paavolainen, M.D. Herrmann, M. Rohban, J. Hung, H. Hennig, J. Concannon, I. Smith, P.A. Clemons, S. Singh, P. Rees, P. Horvath, R.G. Linington, A.E. Carpenter, Data-analysis strategies for image-based cell profiling, *Nature Methods* 14 (9) (2017) 849–863, <https://doi.org/10.1038/nmeth.4397>.
- [9] A. Vigilante, A. Laddach, N. Moens, R. Meleckyte, A. Leha, A. Ghahramani, O. J. Culley, A. Kathuria, C. Hurling, A. Vickers, E. Wiseman, M. Tewary, P. W. Zandstra, *C. HipSci*, R. Durbin, F. Fraternali, O. Stegle, E. Birney, N. M. Luscombe, D. Danovi, F.M. Watt, Identifying extrinsic versus intrinsic drivers of variation in cell behavior in human iPSC lines from healthy donors, *Cell Reports* 26 (8) (2019) 2078–2087.e3, <https://doi.org/10.1016/j.celrep.2019.01.094>.
- [10] D.A. Turner, P. Baillie-Johnson, A. Martinez Arias, Organoids and the genetically encoded self-assembly of embryonic stem cells, *BioEssays: News and Reviews in Molecular, Cellular and Developmental Biology* 38 (2) (2016) 181–191.
- [11] A.E. Carpenter, T.R. Jones, M.R. Lamprecht, C. Clarke, I.H. Kang, O. Friman, D. A. Guertin, J.H. Chang, R.A. Lindquist, J. Moffat, P. Golland, D.M. Sabatini, *Cell Profiler*: image analysis software for identifying and quantifying cell phenotypes, *Genome Biology* 7 (10) (2006) R100, <https://doi.org/10.1186/gb-2006-7-10-r100>.
- [12] H. Kurosawa, Methods for inducing embryoid body formation: in vitro differentiation system of embryonic stem cells, *Journal of Bioscience and Bioengineering* 103 (5) (2007) 389–398, <https://doi.org/10.1263/jbb.103.389>.
- [13] M.D. Ungrin, C. Joshi, A. Nica, C. Bauwens, P.W. Zandstra, Reproducible, ultra high-throughput formation of multicellular organization from single cell suspension-derived human embryonic stem cell aggregates, *PLOS One* 3 (2) (2008) e1565, <https://doi.org/10.1371/journal.pone.0001565>.
- [14] I. Heemskerck, A. Warmflash, Pluripotent stem cells as a model for embryonic patterning: from signaling dynamics to spatial organization in a dish, *Developmental Dynamics: An Official Publication of the American Association of Anatomists* 245 (10) (2016) 976–990, <https://doi.org/10.1002/dvdy.24432>.
- [15] A. Deglincerti, F. Etoe, M.C. Guerra, I. Martyn, J. Metzger, A. Ruzo, M. Simunovic, A. Yoney, A.H. Brivanlou, E. Siggia, A. Warmflash, Self-organization of human embryonic stem cells on micropatterns, *Nature Protocols* 11 (11) (2016) 2223–2232, <https://doi.org/10.1038/nprot.2016.131>.
- [16] M. Tewary, J. Ostblom, N. Shakiba, P.W. Zandstra, A defined platform of human peri-gastrulation-like biological fate patterning reveals coordination between reaction-diffusion and positional-information, *bioRxiv* (2017) 102376, <https://doi.org/10.1101/102376>.
- [17] A.R.G. Libby, D. Briens, I. Haghighi, D.A. Joy, B.R. Conklin, C. Belta, T.C. McDevitt, Automated design of pluripotent stem cell self-organization, *Cell Systems* 9 (5) (2019) 483–495.e10, <https://doi.org/10.1016/j.cels.2019.10.008>.
- [18] U. Ales, *Foveal Vision for Humanoid Robots*, in: E. Cheng (Ed.), *Humanoid Robotics and Neuroscience: Science, Engineering and Society*, CRC Press/Taylor & Francis, Boca Raton (FL), 2015, pp. 103–120.
- [19] J. Comley, Latest developments in high content screening systems in drug discovery world, *London RJ Communications* (2016) 8–13. <https://www.ddw-online.com/screening>.
- [20] A. Foitzik, K. Boettcher, H. Preckel, A. Schreiner, 3D volumetric and zonal analysis of solid spheroids, PerkinElmer technical note, <https://pki.High-Content-Screening/Technical-Note>, 2018.
- [21] H. Kilpinen, A. Goncalves, A. Leha, V. Afzal, K. Alasoo, S. Ashford, S. Bala, D. Bensaddek, F.P. Casale, O.J. Culley, P. Danecsek, A. Faulconbridge, P. W. Harrison, A. Kathuria, D. McCarthy, S.A. McCarthy, R. Meleckyte, Y. Memari, N. Moens, F. Soares, A. Mann, I. Streeter, C.A. Agu, A. Alderton, R. Nelson, S. Harper, M. Patel, A. White, S.R. Patel, L. Clarke, R. Halai, C.M. Kirton, A. Kolb-Kokocinski, P. Beales, E. Birney, D. Danovi, A.I. Lamond, W.H. Ouwehand, L. Vallier, F.M. Watt, R. Durbin, O. Stegle, D.J. Gaffney, Common genetic variation drives molecular heterogeneity in human iPSCs, *Nature* 546 (7658) (2017) 370–375, <https://doi.org/10.1038/nature22403>.
- [22] I. Barbaric, Paul J. Gokhale, Peter W. Andrews, High-content screening of small compounds on human embryonic stem cells, *Biochemical Society Transactions* 38 (4) (2010) 1046–1050.
- [23] A. Paszke, S. Gross, F. Massa, A. Lerer, J. Bradbury, G. Chanan, T. Killeen, Z. Lin, N. Gimelshein, L. Antiga, A. Desmaison, A. Köpf, E. Yang, Z. DeVito, M. Raison, A. Tejani, S. Chilamkurthy, B. Steiner, L. Fang, S. Chintala, PyTorch: An Imperative Style, High-Performance Deep Learning Library, <https://arxiv.org/abs/1912.01703>, 2019.

3.4 Discussion

In this Chapter, I described a 3D model of hiPSC-derived spheroids that undergo distinct morphological changes under diverse medium conditions. We used a standardised starting cell number and obtained consistent sizes in low attachment 96-well plates in suspension. Spheroids were cultured in defined medium conditions E8, KSR BMP4 representing self-renewing and differentiation (indicated by markers expressions as described in the next section, Chapter 4), with their controls, E8 BMP4 and KSR respectively, to monitor spheroids' behaviour. The aim here is to characterise the changes in morphology. Thus, I have established a robust high-content imaging-based platform via live imaging followed by quantification methods based on phase-contrast and confocal images.

In our protocol, I initially optimised hiPSC-selected seeding density by plating a range of single cells (500-5000 cells/well) to obtain reproducible hiPSC spheroids. These results showed a seeding density of 750 hiPSC cells/well in 96-wells V-bottom plate formed optimally reproducible homogenous spheroids, while larger spheroids grew in a disorganised manner when cultured. I, therefore, chose 750 cells/ well as the ideal cell number for all experiments when using (Hoik_1 cell line) due to the formation of well-defined spheroids with standardised size when cultured in E8 medium. Following this, I observed highly reproducible morphological changes in (KSR BMP4 and KSR) elongation or budding between technical replicates.

Recent models described that symmetry-breaking and elongation could be driven under defined culture conditions without the addition or formation of extra-embryonic tissues (Moris et al., 2020, Simunovic et al., 2019, Baillie-Benson et al., 2020). hESC in suspension under defined conditions treated with pulses of the WNT agonist (CHIRON) resulting in an A-P axial organisation (Moris et al., 2020). WNT signalling is sufficient to initiate axial elongation and patterning of the three germ layers in 3D human gastrulation models. In contrast, in similar conditions, the presence of BMP4 without WNT signalling, cells failed to drive similar aggregation and elongation without a noticeable patterning (Moris et al., 2020). hESC in single cells embedded in a mixture of hydrogel and Matrigel under a defined BMP4 dose were able to break the symmetry. In

this model, morphogenesis was identified by EMT markers and BRA/SOX2 polarisation without an obvious presence of A-P axis formation (Simunovic et al., 2019) *in vitro* from distinctive perspectives of axial elongation and EMT molecular markers. However, Moris et al. proposed a more realistic mimic of morphogenesis *in vivo*. In this thesis, I have shown a 3D model of gastrulation using hiPSC spheroid in suspension treated with 50 ng/ml selection of medium condition to compare the outcome between self-renewing (E8) and (KSR BMP4) to their controls E8 BMP4 and KSR to observe the effect of BMP4 and KSR separately.

Moreover, the E8 medium was selected for undifferentiated conditions as it has been used in our hiPSC culture and maintenance protocols (Chen et al., 2011, Zhai et al., 2022). When spheroids are cultured in E8 medium, they maintain a spherical structure suggesting uniform self-renewing. KSR BMP4 clearly changed morphology and displayed A-P axis elongation mirroring morphogenesis during gastrulation. To investigate whether BMP4 or KSR medium alone triggers this axial elongation, this observation was compared with controls E8 BMP4 and KSR. This results in intermediate phenotypes, E8 BMP4 remaining spherical and tends to form but small protrusions. However, spheroids in KSR are unable to elongate but mostly generate a budded structure. These findings suggest that the addition of the BMP4 molecule to the KSR medium induced symmetry breakage and, thus, axial elongation. Nevertheless, we observed high variation values between replicates of each medium condition shown in the morphological quantification due to the differences in 3D spheroid size between experiments (i.e., the analysis was performed on the number of spheroids from 10 different experiments pooled together). To overcome this, the analysis could be performed on spheroids per experiment to minimise data variations of the same condition.

High-content imaging methods have been employed to obtain insight into cellular behaviour and provide multi-parametric data to quantify single cells in a 3D context (Mattiuzzi Usaj et al., 2016). Ideally, images from immunofluorescent stained cells are commonly used to acquire quantitative data owing to the simplicity of segmentation of the nucleus or cell area based on transcriptional or cytoplasmic markers (Carpenter et al., 2006, Alsehli et al., 2021). The read-outs from fluorescents microscopy images enable characterising cell fate specification and spatial patterning in 3D gastruloids (Carragher

et al., 2018, Alsehli et al., 2021). However, live images from phase contrast microscopy generate essential time-dependent morphological read-outs that are not often amenable to be analysed because of the difficulties in segmenting the shape or outline of the region of interest (whole spheroid area) of 3D moving structure (Alsehli et al., 2021, Carragher et al., 2018). I have incorporated a first-author publication (section 3.3.2) reporting a novel method based on analysing live phase contrast microscopy images of hiPSC spheroids. Spheroids region segmentation is created by subtracting the background pixel intensities of two following time points to generate an image with the spheroid, which is eventually used for segmentation. This segmentation method enables efficient analysis of phenotypic changes of live 3D spheroids, including area, size, shape, and roundness. This CellProfiler pipeline can be adapted to analyse additional brightfield images for 3D spheroids across diverse cell systems. A limitation of this pipeline, the analysis might be difficult in situations in which the spheroids are not in a fully transparent material in suspension or spheroids exhibit a high level of movement.

The results in this Chapter demonstrated that biochemical cues in medium conditions influence cell behaviour and produce a consistent phenotypic variation. This supports my hypothesis of BMP4 providing sufficient signals to trigger symmetry breaking and elongation of hiPSC spheroids in suspension. Also, live image technology and the generated image analysis pipeline are valuable tools to capture morphological changes in high-throughput systems. Further characterisation of additional hiPSC lines using this platform will give more overview of phenotypic variability between donors.

4 DISTINCT EXPRESSION OF LINEAGE DIFFERENTIATION MARKERS IN 3D GASTRULATION- LIKE MODELS

4.1 *Introduction*

The biochemical signal from morphogen initiates the axial body formation *in vivo*, which coordinates the dynamic cellular movements and the emergence of tri-lineages of germ layers (van den Brink et al., 2014). The interaction between morphogen-triggered signalling events and germ layers differentiation has been well-studied; however, much less is known about how shape regulates cell fate decisions during gastrulation (Fulton et al., 2020, Lecuit and Lenne, 2007).

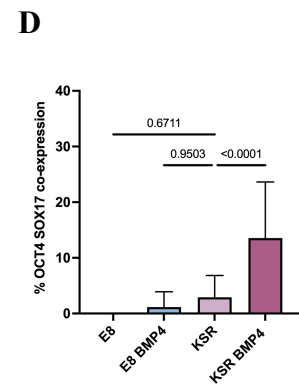
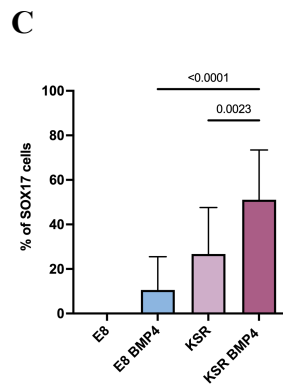
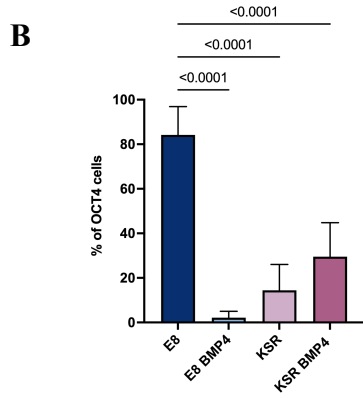
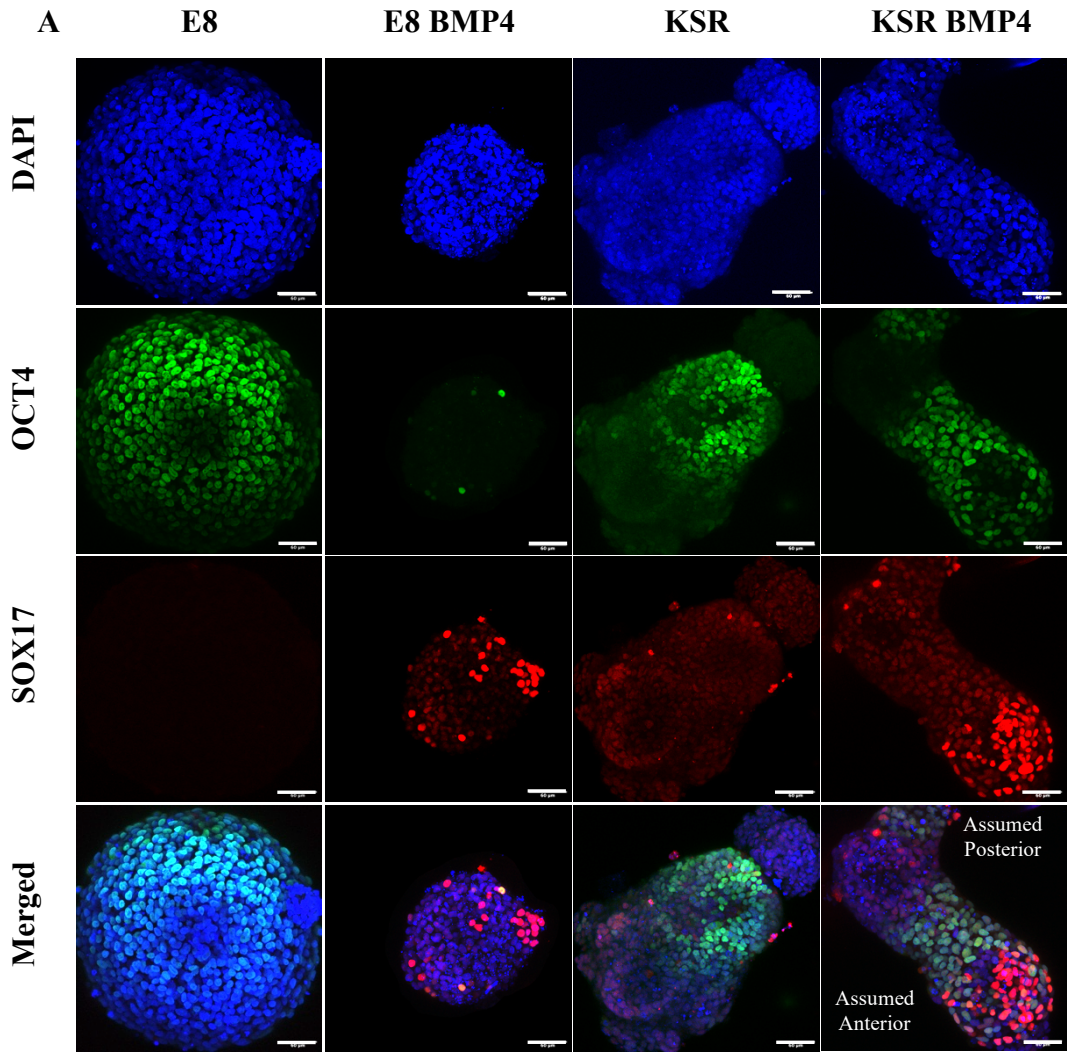
In this Chapter, the main aim is to dissect the relationship between morphological changes and lineage specifications under distinct medium conditions. As explained in the previous Chapter 3 (sections 3.2 and 3.3), I described an experimental set-up adapted from a previous well-defined 2D micropattern, extended into a 3D hiPSC model. This platform showed axial elongation, thus, enabling us to explore whether this model gives rise to the tri-lineage of the three germ layers. I hypothesised that BMP4 signalling is not only sufficient to trigger symmetry breaking and elongation in hiPSC spheroids, but also induces germ layer differentiation in suspension. Secondly, I hypothesised that cellular tension directs spheroids' morphological changes in 3D models in suspension.

4.2 Morphogenesis in hiPSC 3D gastrulation-like model drives three germ layers specification post-BMP4 treatment

Having observed the distinct morphological changes after 96 hours cultured in medium conditions (E8, KSR BMP4 and controls E8 BMP4, KSR), we set to investigate the emergence of the three germ layers differentiation in the different conditions tested. To determine the presence of endoderm, mesoderm and ectoderm lineages, immunostaining for the differentiated markers (SOX17, BRA/EOMES, and SOX2) are respectively used. However, one marker was used to identify each germ layer; markers for endoderm (FOXA2, GATA6); and ectoderm (NESTIN and SOX1) can be used to validate lineage expression (Gao et al., 2020). In addition, the pluripotency marker OCT4 is included, and the percentage of cells expressing a specific marker in the spheroid was then quantified (Figure 4.1 -4.3).

In hiPSC spheroids cultured in E8 medium, the pluripotency marker OCT4 was expressed strongly, but SOX17 was not expressed (Figure 4.1 A). The percentage of cells expressing OCT4 was shown at high levels above 95% of the spheroid, suggesting that cells maintain pluripotency (Figure 4.1 B). In the KSR BMP4, a reduction in the OCT4 marker was observed associated with the emergence of SOX17 expression in the anterior axis, whereas, on the posterior side, OCT4 expression was not detected (Figure 4.1 A). The A-P domains were identified based on visual tracking of the live imaging, the direction of sphere elongation, was classified as anterior, and the original site of the sphere was considered as posterior (Figure 4.2). Then, these images were then compared with confocal images post-immunostaining to validate the assumed A-P domain for each image. Notably, strong SOX17 expression was detected consistently in the distal domain mutually exclusive with the OCT4 marker; the neighbouring cell population co-expressed both OCT4 and SOX17 located in the middle of the elongated structure (Figure 4.1 A). The quantification data showed significant downregulation in the OCT4 marker (P-value <0.0001) and a high percentage of cells expressing SOX17 (endodermal marker); also, a population of cells co-expressing OCT4/SOX17 (Figure 4.1 B-D). However, in E8 BMP4, the pluripotency marker OCT4 was detected at low levels with a polarisation of this marker in the small-budded area (Figure 4.1 A). The percentage of cells expressing OCT4 in this condition was dramatically reduced (P-value <0.0001), and SOX17 was

detected at very low levels (P-value <0.0001) (Figure 4.1 B-C). Spheroids cultured in KSR showed decreased OCT4 expression, and the SOX17 marker was detected (Figure 4.1 A). Quantification of the percentage of marker positive expression in these cells revealed OCT4 reduction (P-value <0.0001) and fewer cells expressed SOX17 (P-value = 0.0023) when compared to SOX17 in KSR BMP4 (Figure 4.1 B-C). Immunostaining controls for the secondary antibodies were performed and shown (see Figure 4.1 E).



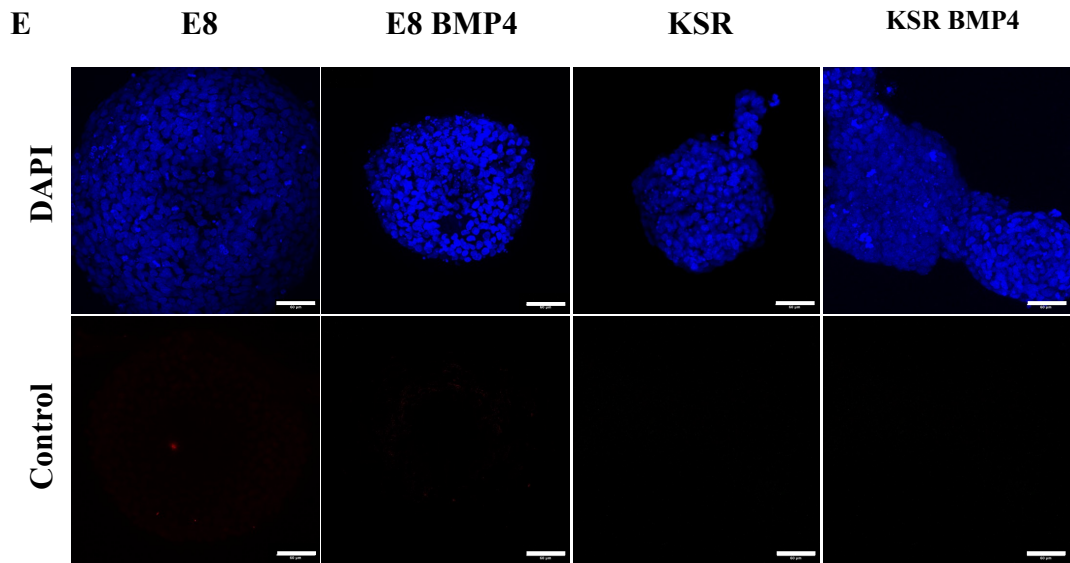


Figure 4.1 BMP4 signalling induces SOX17 specification in 3D model of gastrulation.

A) Immunostaining of OCT4 and SOX17 expression after 96 hours in each medium condition. Spheroids cultured in E8 medium maintained pluripotency indicated by high expression of OCT4 marker, while significant OCT4 reduction was observed in KSR BMP4 and both controls E8 BMP4 and KSR. SOX17 is not detected in E8 medium condition, strong expression of SOX17 marker is expressed in KSR BMP4 and polarised to the assumed anterior side, SOX17 was detected in both E8 BMP4 and KSR conditions. Scale bars 60 μ m. **B)** Quantification of OCT4 positive cells in E8, KSR BMP4, E8 BMP4, and KSR medium condition, statistic test ordinary one-way ANOVA (n=17 spheroids, bars= mean value and SD). **C)** Quantification of SOX17 positive cells in each medium condition, statistic test ordinary one-way ANOVA (n=13 spheroids, bars= mean and SD). **D)** Quantification of OCT4 SOX17 co-expressed cells under the diverse culture conditions, statistical test ordinary one-way ANOVA (n =16, bars= mean and SD). **E)** Secondary only control for (Alexa fluor 488 and 633), images showed DAPI (top), and Controls (bottom).

Therefore, I stained for mesodermal markers (BRA and EOMES) to examine if the proposed 3D models also differentiated towards mesoderm lineages. As expected in the self-renewing condition (E8 medium) the mesodermal markers BRA and EOMES were not expressed (Figure 4.3 A). When 3D spheroids were cultured in KSR BMP4 medium cells were able to specify the mesodermal layer detected by BRA and EOMES expression (Figure 4.3 A). The quantification of the mean of cells expressing BRA is 25% of the spheroid and the highest expression of EOMES was 12% (Figure 4.3 B-C) However, in E8 BMP4 the mesodermal markers BRA was not detected but EOMES weakly expressed

which was confirmed by the percentage of cells quantifications (Figure 4.3 A-C). Low expression of BRA was observed in KSR, whereas EOMES was not expressed (Figure 4.3 A). Moreover, the data revealed that the BRA marker expressed in KSR BMP4 was significantly higher compared to KSR alone (P-value = 0.0175) with no significant differences in EOMES (Figure 4.3 B-C). Secondary antibody controls are shown in (Figure 4.3 D). These readouts indicated that BMP4 not only induces SOX17 (endodermal marker) but also promotes BRA (mesoderm) expression in KSR BMP4.

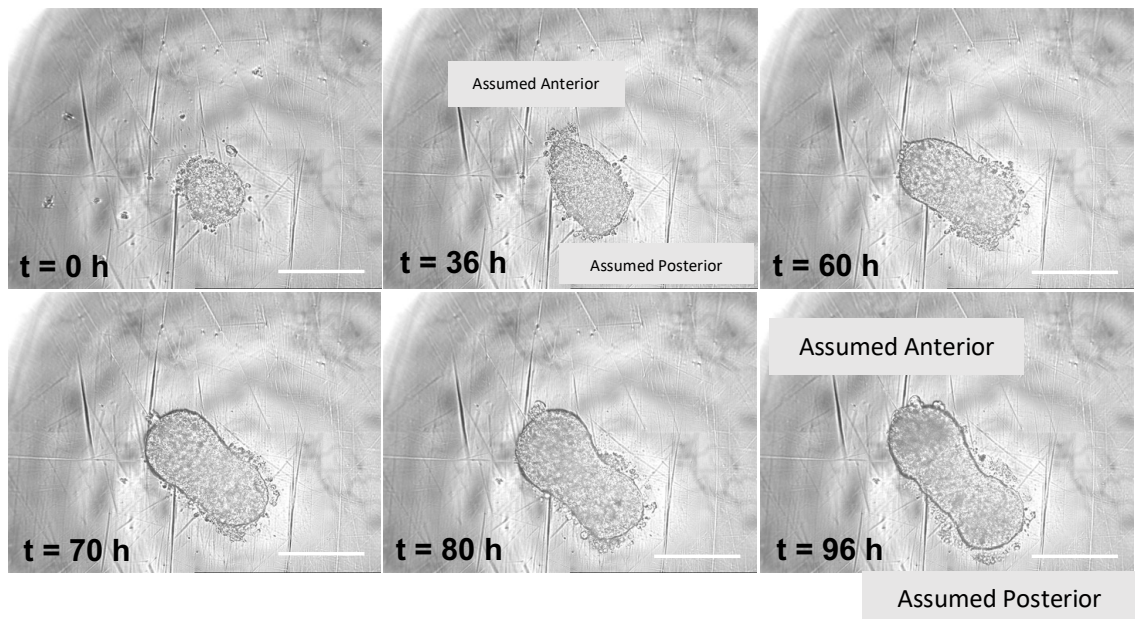
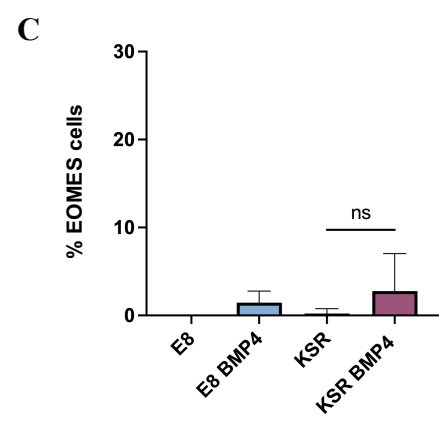
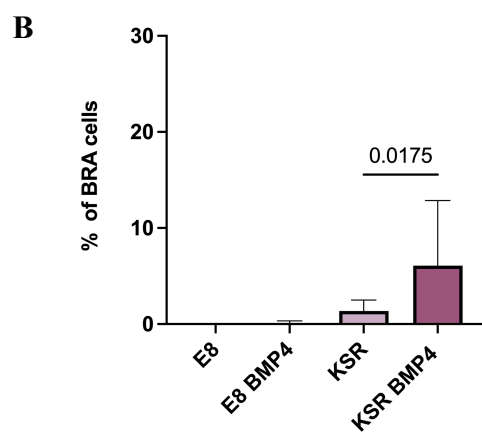
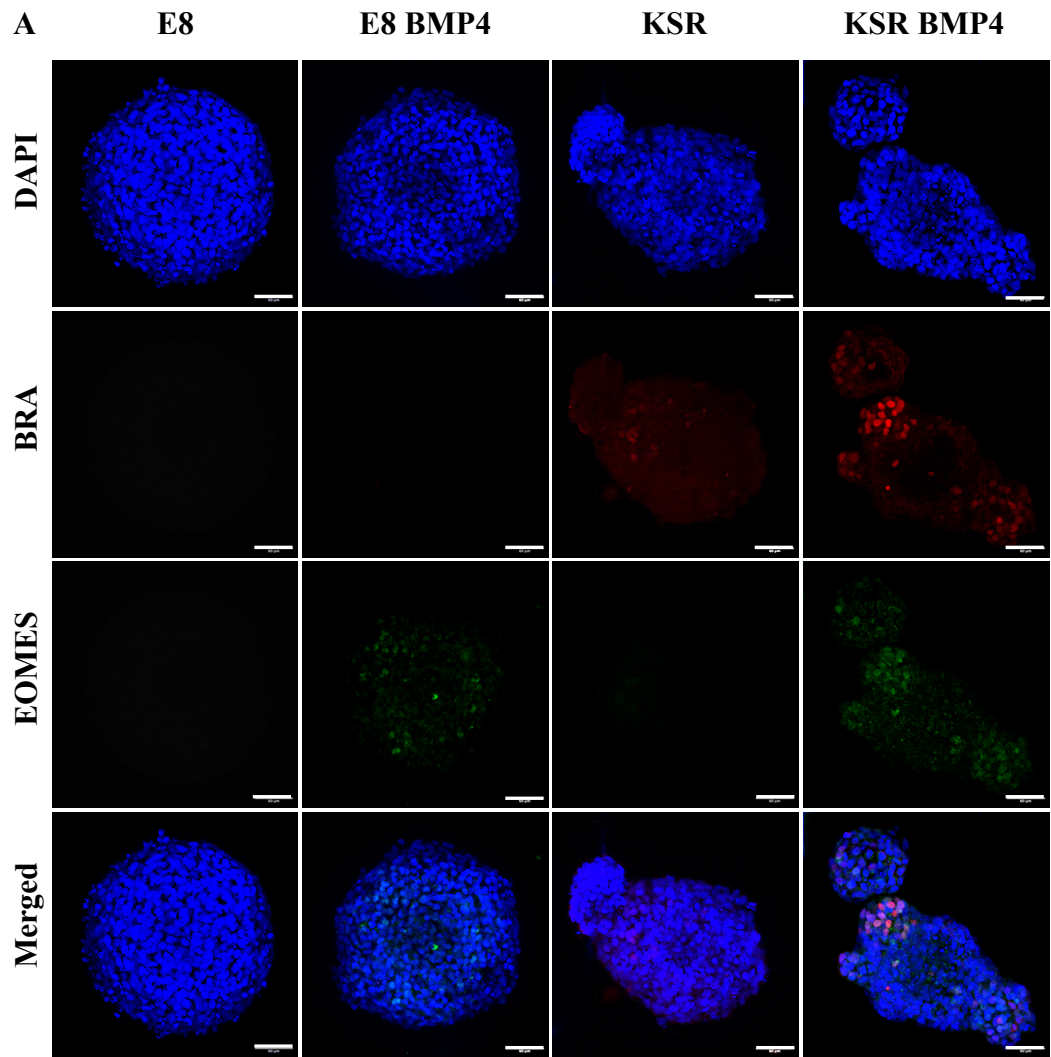


Figure 4.2 Tracking axial elongation via live imaging during time points.

Spheroids cultured in KSR BMP4 medium at different time points showed changes in morphology; at 36 hours the spheroids start to elongate. Tracking the direction of spheroid elongation allow to identify the assumed anterior – posterior domain.



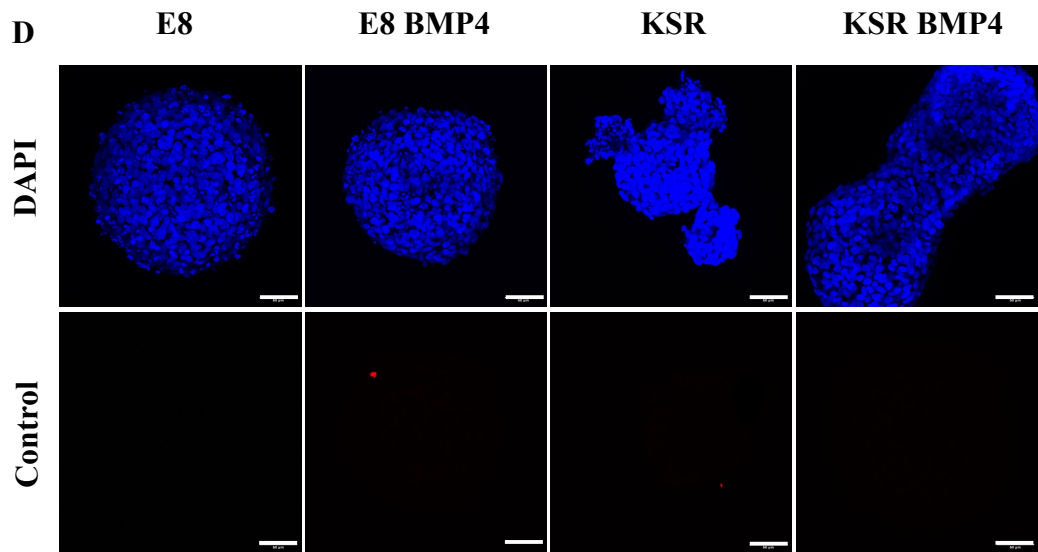


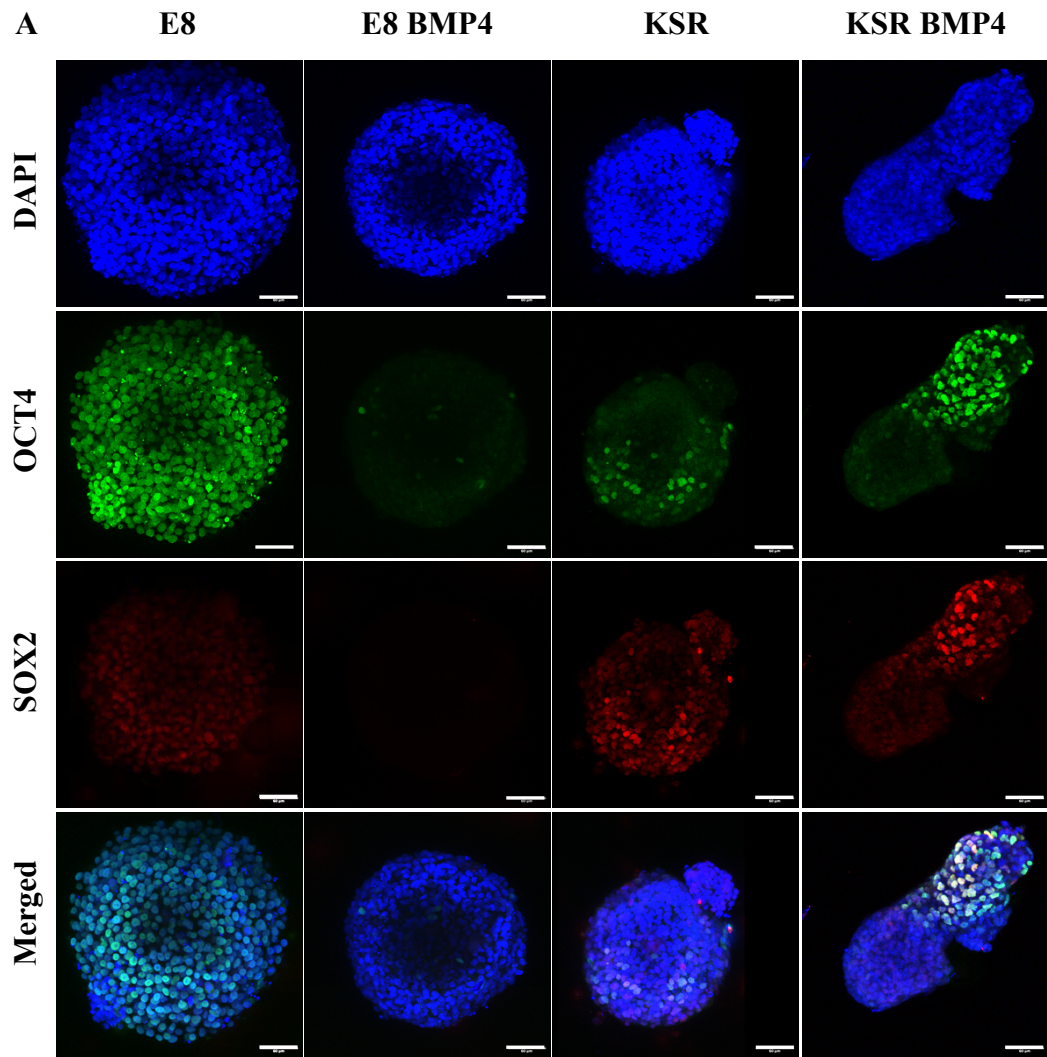
Figure 4.3 The emergence of mesodermal markers BRA and EOMES in 3D model of gastrulation.

A) Immunostaining of BRA and EOMES expression post 96 hours in culture. In E8 medium mesoderm markers were not detected, in KSR BMP4 induced the expression of BRA with a slight EOMES marker, E8 BMP4 showed very low EOMES expression. In contrast, KSR cells exhibited very low BRA expression. Scale bars 60 μm . **B)** Quantification of BRA positive cells in the selected medium conditions E8, KSR BMP4, E8 BMP4 and KSR, statistic test ordinary one-way ANOVA (n=13 spheroids, bars= mean value and SD). **C)** Quantification of EOMES positive cells in the different medium conditions, statistic test ordinary one-way ANOVA (n=13 spheroids, bars= mean and SD). **D)** Control staining for secondary antibodies (Alexa fluor 633 and 488), DAPI (top), and Controls (bottom).

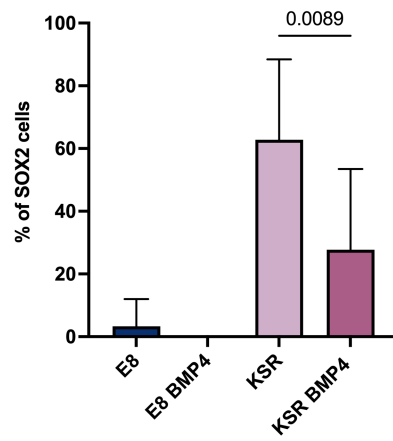
SOX2 is a critical marker involved in pluripotency regulation during the early stages of embryonic development and a marker of ectodermal-like lineage (Nazareth et al., 2013). In the self-renewing condition (E8) spheroids, a slight expression of the SOX2 marker was observed in some spheroids; this was co-expressed with OCT4, the pluripotency marker (Figure 4.3 A-B). In the differentiation medium KSR BMP4, strong expression of SOX2 was detected, and we observed an overlapping between OCT4/ SOX2 (Figure 4.3 A). The data showed an average percentage of cells expressing SOX2 ($\sim 50\%$), and the percentage of cells co-expressing OCT4/SOX2 reaches 15% (Figure 4.3 B-C). In control conditions, spheroids cultured in E8 BMP4 showed negative expression to SOX2, while in KSR, high levels of SOX2 expression and low co-expression levels of OCT4/SOX2 were observed (Figure 4.3 A-C). A comparison between the percentage of SOX2 marker

in (KSR BMP4 and KSR) revealed that SOX2 marker expressed in lower levels compared to KSR (P-value= 0.0089), suggesting that KSR medium promotes ectoderm specification (Figure 4.3 B).

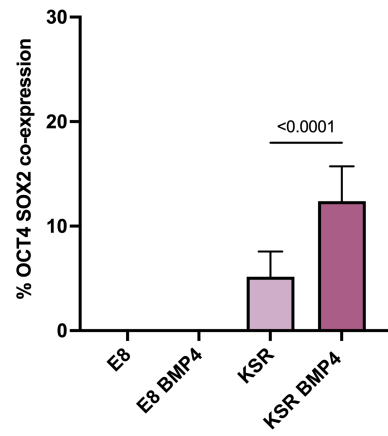
Overall, immunostaining images of 3D hiPSC spheroids showed distinct expression of lineage differentiation markers under diverse culture conditions. In E8 medium, cells maintained OCT4 expression suggesting that spheroids are self-renewing and undifferentiated. However, KSR BMP4 medium induced axial elongation and the emergence of patterned three germ layers (SOX17, BRA, and SOX2 markers). In controls, SOX17 was expressed and polarised toward small budding in E8 BMP4, whereas in KSR, medium cells exhibited high expression of SOX2. Together, these reproducible observations demonstrated that the addition of BMP4 to the KSR medium induces spheroids to undergo gastrulation-like pattern formation, while in E8 BMP4, it triggered SOX17 differentiation; and KSR alone promote spontaneous differentiation mostly toward ectodermal-like lineage. Moreover, additional markers for the germ layer should be tested to validate the presumed lineage specifications.



B



C



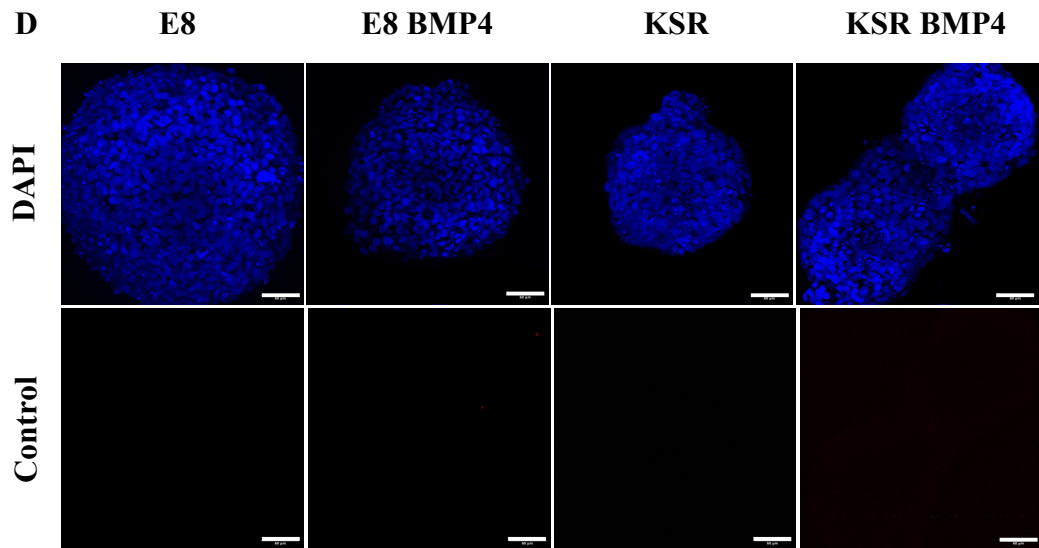


Figure 4.4 The expression of SOX2 marker in 3D model of gastrulation.

A) Immunostaining images representing the OCT4 (pluripotency) and SOX2 marker expressions after 96 hours. OCT4 marker is highly expressed in E8, a significant decrease in OCT4 expression was observed in KSR BMP4, E8 BMP4 and KSR. SOX2 is detected at a low level in E8 medium, and in KSR BMP4 SOX2 is expressed, in control conditions the marker was not detected in E8 BMP4, while it is highly expressed in the KSR condition. Scale bars 60 μm . **B)** Quantification of the percentage SOX2 positive cells in E8, KSR BMP4, E8 BMP4 and KSR, statistic test ordinary one-way ANOVA (n=8 spheroids, bars= mean value and SD). **C)** The percentage of positive cells co-expressing OCT4/SOX2 marker, shown in KSR BMP4 and KSR, statistic test ordinary one-way ANOVA (n=7 spheroids, bars= mean and SD). **D)** Control images DAPI (top), and the secondary only staining (Alexa fluor 488 and 633) (bottom).

4.3 *Biochemical cues of diverse medium conditions regulate morphogenesis via proliferation and cellular tension in 3D spheroids*

Here, we sought to explore whether biochemical cues such as the addition of BMP4 or KSR medium influence the proliferation and cellular tension of the 3D gastrulation model. I hypothesise that proliferation regulates changes in shape and thus promotes morphogenesis. I also postulate that cellular tension under diverse medium conditions within different shapes drives elongation and budding formation therefore differentiation of the three germ layers.

4.3.1 The addition of BMP4 and KSR medium reveals distinct cell proliferation phenotype drives morphological changes in 3D spheroids.

Cell proliferation was investigated using EdU staining on day 6 (before the end of experiments), Edu labelling was incubated for 6 hours before fixation. Previously, optimisation steps were performed to choose the desired working EdU concentration and incubation time. The following concentrations (2 μ M, 4 μ M, 10 μ M) and incubation times (2, 4, 6, 24, 48 hours prior to fixation) were tested on 3D hiPSC cultured under the distinct medium conditions. I found that 2 μ M EdU concentration was too low to label the proliferative cells when tested at the selected time points, whereas 10 μ M concentration resulted in spheroids bursting within 2 hours of incubation. When cells were incubated in 4 μ M for 2, and 4 hours, EdU staining was only detected in spheroids cultured in E8 medium, while in E8 BMP4 Edu was not seen after 2 hours; but very low expression was detected after 4 hours. However, Edu labelling at the selected time points was not detected in both conditions KSR BMP4 and KSR, and it is impossible that cells are not proliferating. Then, I opted for 4 μ M concentration 6 hours before the endpoint due to the ideal EdU labelling for all conditions without affecting the spheroids. In E8 medium, spheroids showed highly proliferative cells with homogenous EdU expression (Figure 4.5 A). When spheroids were cultured in KSR BMP4 medium, cell proliferation was potentially reduced and EdU expression was restricted to the tip of the elongated spheroid (Figure 4.5 A). In the intermediate conditions, the proliferation rate in E8 BMP4 was significantly decreased, whereas spheroids cultured in KSR proliferative cells notably polarised toward the budding area (Figure 4.5 A). In addition, data quantification revealed higher proliferative cells in the self-renewing state (E8); however, the percentage of proliferative cells was decreased upon BMP4 treatment in both medium (E8 and KSR (Figure 4.5 B). Altogether, these results indicate that biochemical cues in the medium regulate cell proliferation, suggesting that low cell proliferation is associated with BMP4 addition to the medium. In contrast, KSR medium governs proliferative cells polarisation, which induces morphogenesis and differentiation.

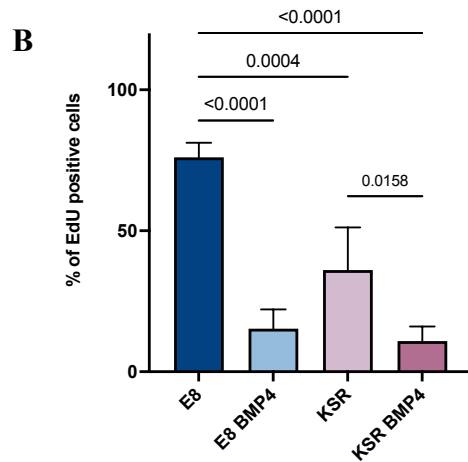
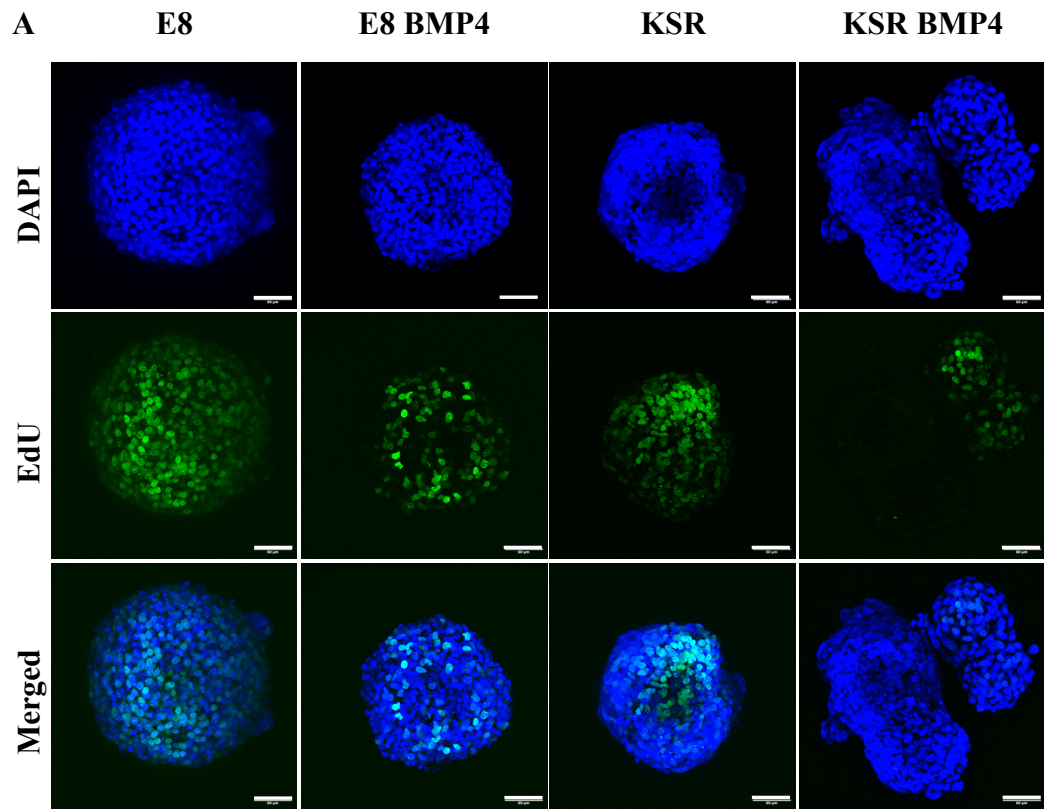


Figure 4.5 Distinct proliferation phenotype in response to biochemical cues.

A) Proliferation assay indicated by EdU staining labels for 6 hours before the endpoint (96 hours) shows high EdU positive expression in E8 medium, spheroids in KSR BMP4 shows EdU positive cells restricted to the budding area. Both controls E8 BMP4 and KSR shows reduced EdU expression, in KSR medium EdU positive cells begin to polarise toward the budding. Scale bars 60 μm . **B)** Quantification of the percentage of EdU expression in E8 medium, KSR BMP4 and their controls E8 BMP4 and KSR, statistic test ordinary one-way ANOVA (n=4 spheroids, bars= mean and SD).

4.3.2 Cellular tension drives elongation and budding formation under differentiation conditions

It has been reported that changes in cell morphology occur due to cellular tension generated within the tissue (Clarke and Martin, 2021). To explore the patterning of F-actin orientation, I stained for phalloidin and YAP translocation to determine cell tension.

Phalloidin staining revealed that spheroids cultured in E8 medium exhibited organised and tightly packed F-actin with homogenous network orientation (Figure 4.6 A). In KSR BMP4 condition we observed a disorganised and stretched F-actin network localised more around the edges (Figure 4.6 A). However, images of spheroids cultured in E8 BMP4 showed F-actin accumulation in the core of the spheroids (Figure 4.6 A). In KSR medium culture condition we also observed a disorganised F-actin network stretching around the edges (Figure 4.6 A). Overall, these data suggested that BMP4 and KSR trigger changes in morphology through cellular tension produced from F-actin orientation.

Next, a pipeline to quantify the F-actin orientation was created using icy software to calculate F-actin distribution based on the F-actin intensity in the centre or peripherally region as described in Chapter 2 (section 2.5.3.4 and Figure 2.1 A, Appendix 1) in detail. The data revealed the percentage of the proportion of F-actin intensity expression of round shape when cultured in E8 medium mostly distributed in the inner core (centrally); however, in KSR BMP4, elongated spheroids showed more F-actin intensity expression to the periphery (Figure 4.6 B). In control conditions, E8 BMP4 medium F-actin intensity expression in the centre was similar to E8 medium condition. Nonetheless, more variation was observed between spheroids, whereas in KSR condition, F-actin was expressed in the periphery without significant differences compared to KSR medium conditions (Figure 4.6 B). These observations indicated that in both differentiation conditions, KSR and KSR BMP4 cellular tension drives morphogenesis.

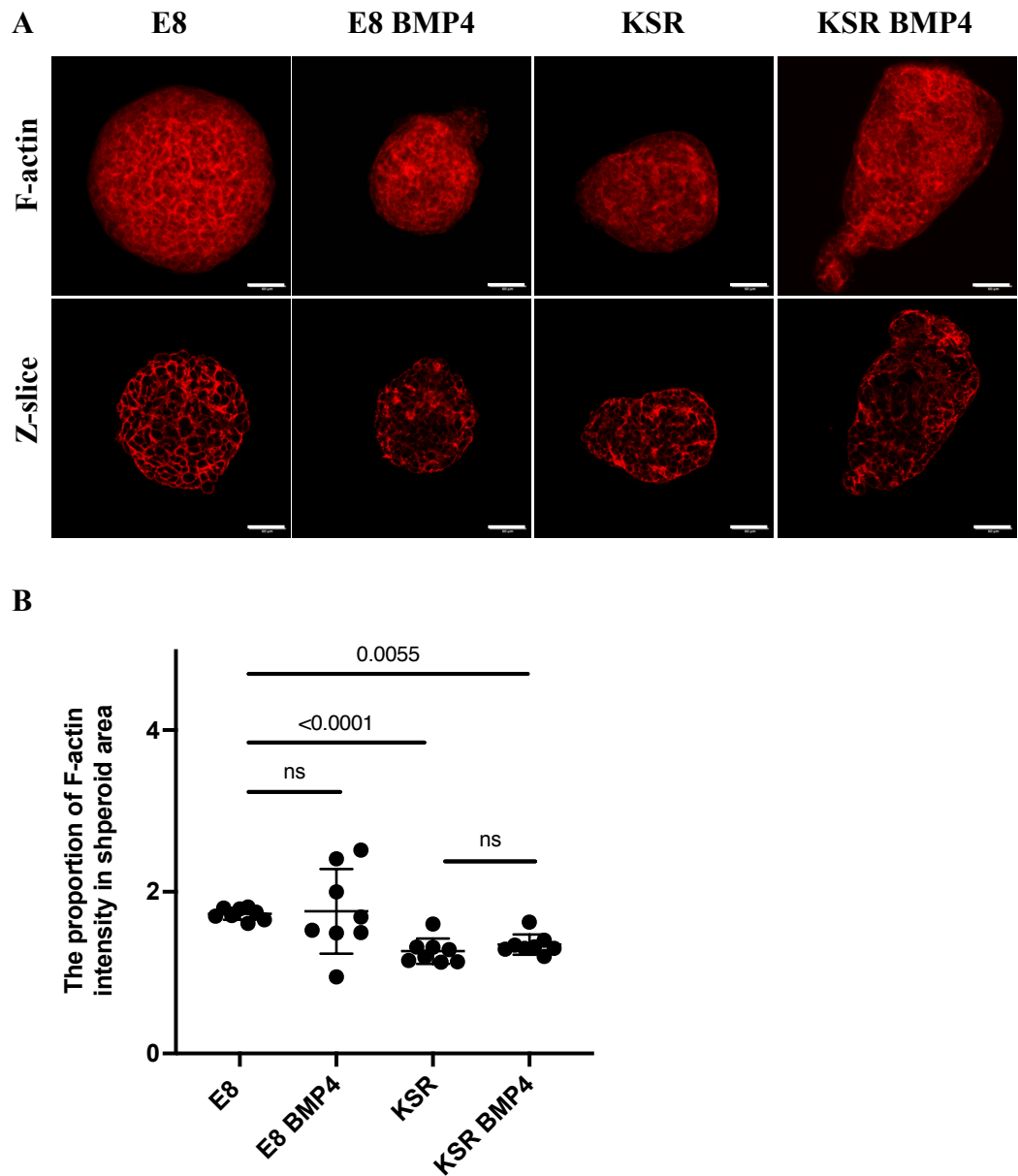


Figure 4.6 F-actin network orientation drives elongation in the 3D models.

A) Phalloidin staining after 96 hours shows a homogenous F-actin network in E8 medium condition, loose F-actin network was observed in KSR BMP4 condition, E8 BMP4 and KSR (z- slice; scale bar 60 μ m). **B)** Quantification of the F-actin intensity expression in the proportion spheroid area. The graph shows the distribution ratio related to the inner region of the spheroid area, statistic unpaired t-test (n=8 spheroids, bars= mean and SD).

YAP is a mechanotransductive protein that can sense the tension in response to mechanical stimuli, and it is localised in the nucleus if active (under tissue tension) and in the cytoplasm when inactive (Halder et al., 2012). To acquire some mechanistic insights and molecular demonstration of whether cellular tension influences spheroids morphogenesis in the 3D model. I opt to compare YAP localisation in the two extremes of distinct morphologies cultured in E8 vs. KSR BMP4 (round vs. elongated), as shown in (Figure 4.7 A). The 3D hiPSC spheroid in the E8 medium showed YAP expression clearly in the cytoplasm suggesting inactivation of YAP, whereas in KSR BMP4 medium (elongated area) exhibited YAP expression in the nucleus suggesting activation of YAP in response to cellular tension (Figure 4.7 A).

Altogether, these data showed that cellular tension on different spheroid morphology under diverse medium conditions investigated by F-actin distribution and nucleus/cytoplasmic YAP localisation direct budding formation and differentiation of the three germ layers.

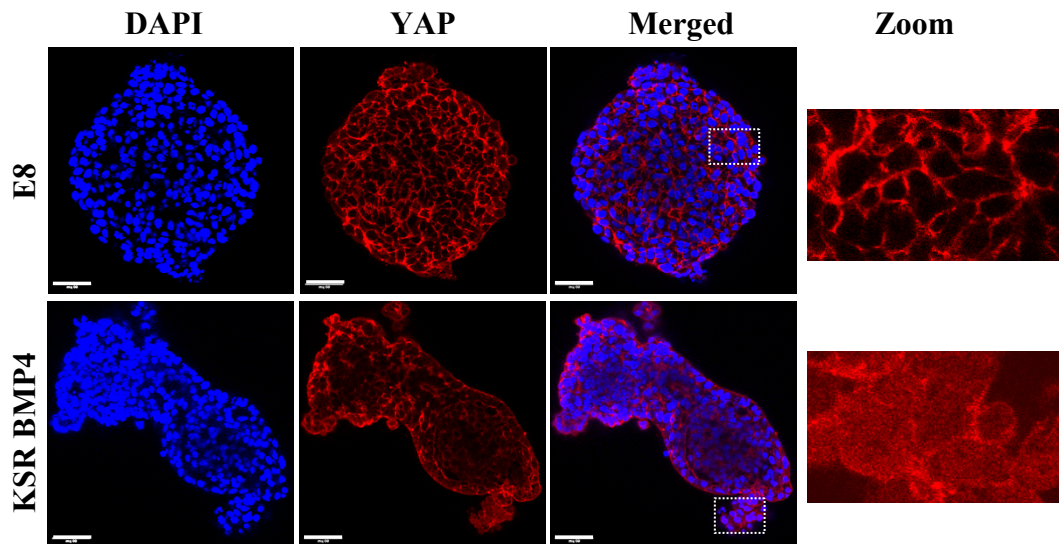


Figure 4.7 YAP translocation influences morphogenesis in hiPSC.

Immunostaining of YAP localisation shows cytoplasmic YAP in E8 medium (top), in KSR BMP4 (bottom) condition YAP localised to the nucleus as indicated in the magnification images (z- slice; scale bar 60 μ m).

4.4 Discussion

In the gastrulation process *in vivo*, the three germ layers specification from the pluripotent cells of the epiblast is associated with dynamic changes in morphology represented by the A-P axis formation in the human embryo (Probst et al., 2021). hiPSC lines are pluripotent cells with the ability and the propensity to specify to the three germ layers *in vitro* (Rowe and Daley, 2019). In this chapter, I hypothesised that 3D hiPSC undergo elongation and differentiate to form the tri-germ layer lineages upon BMP4 treatment. Then, I showed that biochemical cues of the different medium conditions (E8, KSR BMP4, and their controls E8 BMP4 and KSR) regulate cell proliferation together with cellular tensions controlling morphogenesis and elongation in the 3D gastrulation-like model.

Several studies have described 3D gastrulation models under defined culture conditions when stimulating WNT, FGF, NODAL and BMP4 signalling pathway or their inhibitors to induce symmetry breaking and differentiation into germ layers lineages (Liu and Warmflash, 2021, Martyn et al., 2018). Signalling pathways *in vivo* occur in a feedback manner as BMP signalling is initiated from the ExE, thereby activating the WNT pathway to NODAL activation and then turning back to BMP (Ben-Haim et al., 2006a, Camacho-Aguilar and Warmflash, 2020, Chhabra et al., 2019). Consequently, this signalling cascade creates morphogen gradients that allow for the spatial organisation of germ layer specification (Liu and Warmflash, 2021, Camacho-Aguilar and Warmflash, 2020). It has been proven that BMP4 triggers first TE formation and mesodermal (primitive streak) and all the tri-lineage specifications. Inhibition of BMP4 signalling resulted in the loss of mesoderm formation, therefore differentiation (Gunne-Braden et al., 2020, Nemashkalo et al., 2017). This has been well established in hESC treated with BMP4 in a 2D micropattern system, the three germ layers self-organised, forming a radial pattern very similar to *in vivo* (Warmflash et al., 2014, Gunne-Braden et al., 2020). In the 3D epiblast model, BMP4 signalling is used to induce symmetry breaking, identified via the segregation of BRA/SOX2 domains without an axis formation (Simunovic et al., 2019). However, a recent study revealed that the use of WNT agonist pulse CHIRON stimulates axial elongation and triggers the expression of BRA (mesoderm), SOX17 (endoderm), and SOX2 (ectoderm) in the anterior; CDX2 and GATA6 in the posterior resembling the

TE. Substituting this with BMP4 results in failure to establish elongation and lack of BRA marker expression, therefore, differentiation (Moris et al., 2020). Both studies explored the main features of gastrulation, showing the ability of BMP4 to break symmetry and undergo EMT. On the other hand, the further study showed the inability of BMP4 to establish axial elongation and lineages specification (Simunovic et al., 2019, Moris et al., 2020). Overall, this has opened the opportunity for us to investigate the use of BMP4 in 3D models in suspension adapted from the well-defined 2D micropattern system by Warmflash (Warmflash et al., 2014, Deglincerti et al., 2016, Minn et al., 2020).

In this Chapter, I have shown that 3D hiPSC treated with BMP4 under defined culture condition was able to break symmetry, form axial elongation and generate the tri-germ layers (ectoderm, mesoderm, and endoderm). The identification of A-P domains was assumed entirely based on live imaging by tracking the elongation direction and then crosschecked with confocal images for each spheroid. However, this method is not ideal, to identify A-P domains, immunostaining markers assessments are needed to validate this. Lineage specifications were shown by the expression markers SOX2, BRA/EOMES and SOX17. Notably, SOX2 expression indicates that the cells may remain pluripotent or differentiated towards ectoderm lineage. This can be determined by the presence or absence of OCT4 expression (Nazareth et al., 2013). The defined concentration of BMP4 doses has been investigated in many studies, a low dose of BMP4 was not able to induce differentiation, and cells remained SOX2 positive (pluripotent). In contrast, in higher concentrations 5 ng/ml or 10 ng/ml, most cells expressed BRA. However, 50 ng/ml concentration of BMP4 was sufficient to promote self-organised pattern formation of the three germ layers (Simunovic et al., 2019, Tewary et al., 2017, Gunne-Braden et al., 2020). Here, I compared the culture conditions representing self-renewing (E8 medium) versus the differentiation using (KSR medium) with BMP4 and respective controls to explore how biochemical cues influence differentiation. After 96 hours in culture, spheroids in E8 medium condition remained pluripotent and expressed a high level of OCT4, low level of SOX2, and absence of both BRA and SOX17 expression. The presence of SOX2 expression in the undifferentiated state is due to the transduction vector (SOX2) during the hiPSC reprogramming; this was reported in many HipSci cell lines, including Hoik_1 (Vigilante et al., 2019, Kilpinen et al., 2017). In contrast, cells in the KSR BMP4 spontaneously generate A-P axial elongation and reproducible polarisation

of SOX17 marker (endoderm) at the tip of the extended elongation, and neighbouring cells express BRA (mesoderm) and SOX2 marker adjacent to each other. This suggests that 50 ng/ml BMP4 in the KSR medium is sufficient to induce morphogenesis and germ layers specification in a 3D model using hiPSC consistent with the 2D micropattern model. Moreover, elongated spheroids exhibit OCT4 expression in the neck of the spheroid, together with no detection of OCT4 expression on the posterior side. This is similar to the 2D micropattern in response to BMP4 treatment, hESC expressed pluripotency markers at the central colony. This phenotype resembles an early developmental phase when the primitive streak started to form the rest of the epiblast remains pluripotent (Chhabra et al., 2019). In another recent study using a 2D micro-disc adapted from the conventional micropatterned method, they performed single RNA sequencing demonstrating the formation of distinct cell lineages during *in vitro* gastrulation in the micropatterned model. These cell lineages include epiblast, ectoderm, mesoderm, endoderm, primordial germ cells PGCs, and ExE-like corresponding to TE (Minn et al., 2020). In addition, the positive OCT4 marker in the neck of the spheroid SOX17 marker co-expression was observed in KSR BMP4 may indicate PE population. It has been suggested that the SOX17 marker contributes to regulating cell fate commitment during the early stages of development (Niakan et al., 2010, Probst et al., 2021). In a previous study, Niakan et al. determined the ability of SOX17 to regulate gene expressions related to pluripotency and self-renewing (SOX2, OCT4 and NANOG) to promote differentiation (Niakan et al., 2010). They suggest that SOX17 compete with SOX2, NANOG, and Oct4 and promotes differentiation-related gene expression. mESC were treated with doxycycline to induce SOX17 expression, thus significantly inhibiting self-renewal markers. On the other hand, the lack of SOX17-positive cells led to a potential increase in self-renewal OCT4 or NANOG. This interesting finding may elucidate our immunostaining observation in spheroids in KSR BMP4 medium and the emergence of the SOX17 marker together with the OCT4 marker, which may be involved in OCT4 downregulation and the emergence of SOX17 positive cells only in the assumed anterior domain. The other markers, SOX2 and BRA were absent in the E8 BMP4 medium, while in KSR, high expression of SOX2 and a decrease in BRA marker were observed. This indicates that BMP4 induced SOX17 expression when added to the E8 medium; however, in KSR, spheroids undergo spontaneous differentiation toward SOX2

lineage. These results support that SOX17 marker first inhibits self-renewing gene expression (shown in E8 BMP4) and induces germ layers specification under the appropriate differentiation medium. Unlike the KSR BMP4 condition, when spheroids culture in E8 BMP4, they expressed SOX17 only with a significant reduction in OCT4 marker and the lack of SOX2 and BRA markers. This could be due to the low expression of SOX17 and the absence of axial elongation. Various studies have claimed that SOX17 is a critical marker that may induce PGCs formation during early development (Minn et al., 2020, Tewary et al., 2017). However, we define the expression of SOX17 when cultured in KSR BMP4 as PE population and endoderm due to the observation of SOX2 expression. Theoretically, this is consistent with the literature on the PGCs identities in the absence of SOX2 expression (Fang et al., 2020).

Having observed how spheroids behave in each medium condition, I asked whether biochemical cues in the medium influence cell proliferation and cellular tension, therefore, morphogenesis. The proliferation assay revealed interesting observations when spheroids were cultured in BMP4 supplemented medium and KSR medium; to our knowledge, this has yet to be investigated previously. Here, our control is the self-renewing condition in (E8 medium) as they exhibited a homogeneously increased cell proliferation. When BMP4 was added to the medium, it significantly decreased cell proliferation in both KSR and E8. On the other hand, KSR medium alone or without BMP4 triggers polarisation in cell proliferation. This potentially suggests that biochemical cues in the medium regulate proliferation in E8 medium cells rapidly dividing and having prolonged proliferation resembling the early embryonic cells (Padgett and Santos, 2020, Prakash Bangalore et al., 2017).

Furthermore, it has been found that cells cultured in the E8 medium express higher reactive oxygen species (ROS) and higher mitochondrial potential than the KSR medium. This elevated ROS significantly increase cell proliferation and lowers their differentiation capacity compared to E8 medium (Prakash Bangalore et al., 2017). Another possibility is that E8 medium consists of a high concentration of bFGF2 (100 ng/ml), which maintains self-renewing and proliferation (Mossahebi-Mohammadi et al., 2020, Levenstein et al., 2006). During differentiation, cells exhibit a slower proliferation (Padgett and Santos,

2020). This explains the observation when BMP4 reduced proliferation, and KSR medium governs the polarisation toward the budding area and induces elongation.

At the tissue level, morphogenesis and cell fate decisions are regulated by the interplay between physical and morphogen signalling of the local environment (Vianello and Lutolf, 2019, Kim et al., 2018b). In response to biochemical cues, cells generate physical tensions via the cytoskeletal or cell-adhesions that drive changes in tissue morphology and lineage differentiation (Kim et al., 2018b). Here, I postulated that cellular tension controls spheroid morphology by investigating the F-actin distribution and YAP mechanotransduction protein as readouts for produced forces between cells of the observed phenotype. The F-actin staining results and the quantification data revealed that in E8 medium, the spherical structure showed intact F-actin network and the proportion of F-actin intensity expression (distributed in the inner region) of the spheroid area. This suggests that the produced tension from the inner core thus drives the sphere to expand homogeneously. In KSR BMP4 elongated structure, the stretched F-actin intensity is expressed more around the periphery, indicating higher tension around the edges, especially at the elongated area, which may contribute to the elongation process. In the intermediate conditions, in response to the BMP4 addition to the E8 medium, the proportion of F-actin intensity in the spheroid area showed central expression and accumulation of F-actin adjacent to the budding formation; however, the KSR medium spheroids behave a lot similarly to the KSR BMP4. It has been reported that the polymerisation of the F-actin network toward the plasma membrane or the edge generates pushing forces resulting in shape changes (Clarke and Martin, 2021). This emphasises that in response to biochemical cues (BMP4 or KSR medium), F-actin network orientation generates physical forces and regulates morphological changes. However, further experiments coupling F-actin staining (pushing) with myosin II staining (pulling) to explore how pushing and pulling forces coordinate to guide morphogenesis would be interesting (Clarke and Martin, 2021). Integrating our F-actin results with YAP staining results support the notion that spheroids in E8 medium experience low tension as they express cytoplasmic YAP in the inactive form.

In contrast, nuclear YAP expression is observed in the elongated area of the KSR BMP4 condition. This has been shown in a recent study, during intestinal crypt formation YAP

was expressed evenly nuclear through the tissue then nuclear YAP localisation became restricted to the budding area (Gjorevski et al., 2022). Overall, these findings showed that biochemical cues interplay with physical signals to regulate shape changes and differentiation.

In this Chapter, I reported that BMP4 signalling in 3D model of gastrulation using hiPSC induces axis formation and differentiation into ectoderm, mesoderm, and endoderm. I also investigated how biochemical cues influence cell proliferation and cellular tensions regulate morphogenesis under distinct medium conditions. It is reasonable to postulate that morphogen signals *in vivo* and *in vitro* will trigger the morphogenesis process that will partially depend on their external environment. Cell- ECM via adhesion molecules interactions contribute to transmitting physical forces to direct cell fate organisation (Vining and Mooney, 2017). A limitation of this work is that the selection of antibodies for each lineage needed to be revised to validate the emergence of the three germ layers specification, especially for the ectodermal marker, as SOX2 can indicate pluripotency. Further investigation on additional expression markers will help to validate lineages including CDX2 (TE), NANOG, FOXA2, NESTIN, and SOX1. Investigating the signalling pathways using SMAD2/3 and SMAD4 immunofluorescence staining to obtain morphogen gradient profiles using this model will be interesting.

5 PHYSICAL CONFINEMENT INFLUENCES MORPHOLOGICAL CHANGES AND EXPRESSION OF LINEAGE SPECIFICATION MARKERS

5.1 *Introduction*

Morphological changes during early development are regulated through signalling cascade feedback and endogenous physical cues transmitted between the cells and ECM (Muncie et al., 2020, Nemashkalo et al., 2017). In addition, there is a pivotal contribution originating from the local environment of the uterus or extraembryonic tissues to provide mechanical stress and physical constraints, thus directing the morphogenesis (Vianello and Lutolf, 2019, Indana et al., 2021).

Previously (in Chapter 4), I showed how biochemical cues under defined medium conditions drive changes in morphology and induced three germ layers differentiation in a 3D hiPSC model of gastrulation. The emergence of SOX17, BRA, and SOX2 expression might depend on the shape changes of 3D spheroids in suspension. Following this observation, we set to address whether morphogenesis is required to direct lineage differentiation and patterning. In this Chapter, the PEG-based hydrogels system was used as a tool aiming to investigate how physical confinement influences morphogenesis and lineage specifications. This system has been established and fully characterised previously by former members of Eileen Gentleman's group.

I hypothesised that PEG-peptide hydrogels would prevent elongation and, thus, affects not just morphogenesis but also cell fate specification. Similar to the 3D hiPSC spheroids in suspension protocol (Chapter 4), cells were cultured in (E8, KSR BMP4, E8 BMP4, and KSR) mediums post-embedding in PEG-based hydrogels of different physical properties. Our approach enables us to investigate in hiPSC the inter-correlation of changes in shape with the patterning of germ layers.

5.2 *PEG-peptide hydrogel modulation resulted in softer gels*

Having observed the distinct morphological changes in 3D in suspension in (Chapter 3) (described in section 3.2) here, we harnessed a platform for physically confined spheroid. This platform has been reported previously by the Gentleman's group to explore the role of matrix remodelling in the hiPSC-derived intestinal organoids (Jowett et al., 2021). The tetra-PEG hydrogels are created basis on two sequential reactions on the bases of (A_4+B_4) or (A_4+C_4) design (Figure 5.1 A-C). The first step of this reaction mechanism is where the NPC end of the PEG-4NPC reacted with the amine group (N-terminal) at the hetero peptide (non-functional, adhesive, or degradable) at a 1:1 ratio forming in tetra PEG-peptide conjugates (A_4). Next, hydrogel networks were formed when the tetra PEG-peptide conjugates (A_4) reacted with PEG-4VS (B_4) non-degPEG or PEG-4Acr (C_4) deg-PEG via Michael addition between the free thiol group at (C-terminal) of the peptide form the cysteine residue with the vinyl sulfone or acrylate group at the chain end. The group has reported that this A_4+B_4 design showed high crosslinking efficiency (>90% efficiency) and stiffer hydrogels when formed at low polymer concentrations compared to other systems (Jowett et al., 2021, Lust et al., 2021).

Therefore, to obtain some insight into the mechanical behaviour of both hydrogel designs (A_4+B_4) and (A_4+C_4), characterisation measurements, including degradation assay and rheology, were performed (Figure 5.2 A-C). First, to determine whether the deg-PEG (PEG-4Acr) undergoes degradation over time which could be indicated through the tryptophane release when the peptide conjugates bonds break down. Here, 2.5% polymer concentration hydrogels were formed and crosslinked on the following conditions (100% PEG-4VS), (100% PEG-4Acr), (75% PEG-4Acr + 25% PEG-4VS), and (50% PEG-4Acr+ 50% PEG-4VS). Hydrogels were submerged in a culture medium and monitored for 11 days. This experiment revealed that 100% PEG-4Acr and 75% PEG-4Acr softened by day 7, but 100% PEG-4Acr degraded completely by day 11 (Figure 5.2 A). These observations confirmed that 100% PEG-4Acr behaves differently compared to 100% PEG-4VS in terms of the ability to soften over time.

Next, we sought to choose what percentage of deg-PEG is needed to modulate semi-rigid hydrogel, the hydrogels were formulated at (100% PEG-4VS), (75% PEG-4Acr +25%

PEG-4VS), and controls (50% PEG-4Acr+ 50% PEG-4VS), and (25% PEG-4Acr + 75% PEG-4VS). Hydrogel degradation was assessed by measuring the absorbance of tryptophan released in the medium. Our data showed that the deg-PEG hydrogel designed using 75% PEG-4Acr has the highest value compared to the other hydrogel conditions (Figure 5.2 B). However, for more accurate mechanical characterisation, small amplitude oscillatory rheology measurements were used (Figure 5.2 C). The obtained readout refers to the (G' prime) - the storage modulus is used to detect hydrogel elasticity. These data confirmed that standard PEG hydrogels cross-linked with non-degPEG (100% non-degPEG) did not exhibit significant changes in stiffness over 5 days under standard culture conditions $G' \sim 488.3$ Pa to 329.9 Pa (P value = ns) (Figure 5.2 C). Hydrogels formed with deg-PEG (75% PEG-4Acr) softened over 5 days and were significantly softer than day 0 with a $G' \sim 272$ Pa to 78.7 Pa (P < 0.0001). After day 5 the hydrogel was fully softened, which was not possible to measure in the rheometer (Figure 5.2 C). Similarly, both intermediate hydrogels were softened at different degrees, 75% PEG-4VS $G' \sim 460.1$ Pa to 232 Pa (P = 0.0086), whereas 50% PEG-4VS $G' \sim 354$ Pa to 126.5 Pa (P < 0.0001), statistic test used in this analysis is one sample t-test (Figure 5.2 C). Altogether, these results showed that the deg-PEG condition supports hydrogel softening, allowing us to modulate softer hydrogel initially at day 0 compared to non-degPEG condition thus continuing to be softer over time.

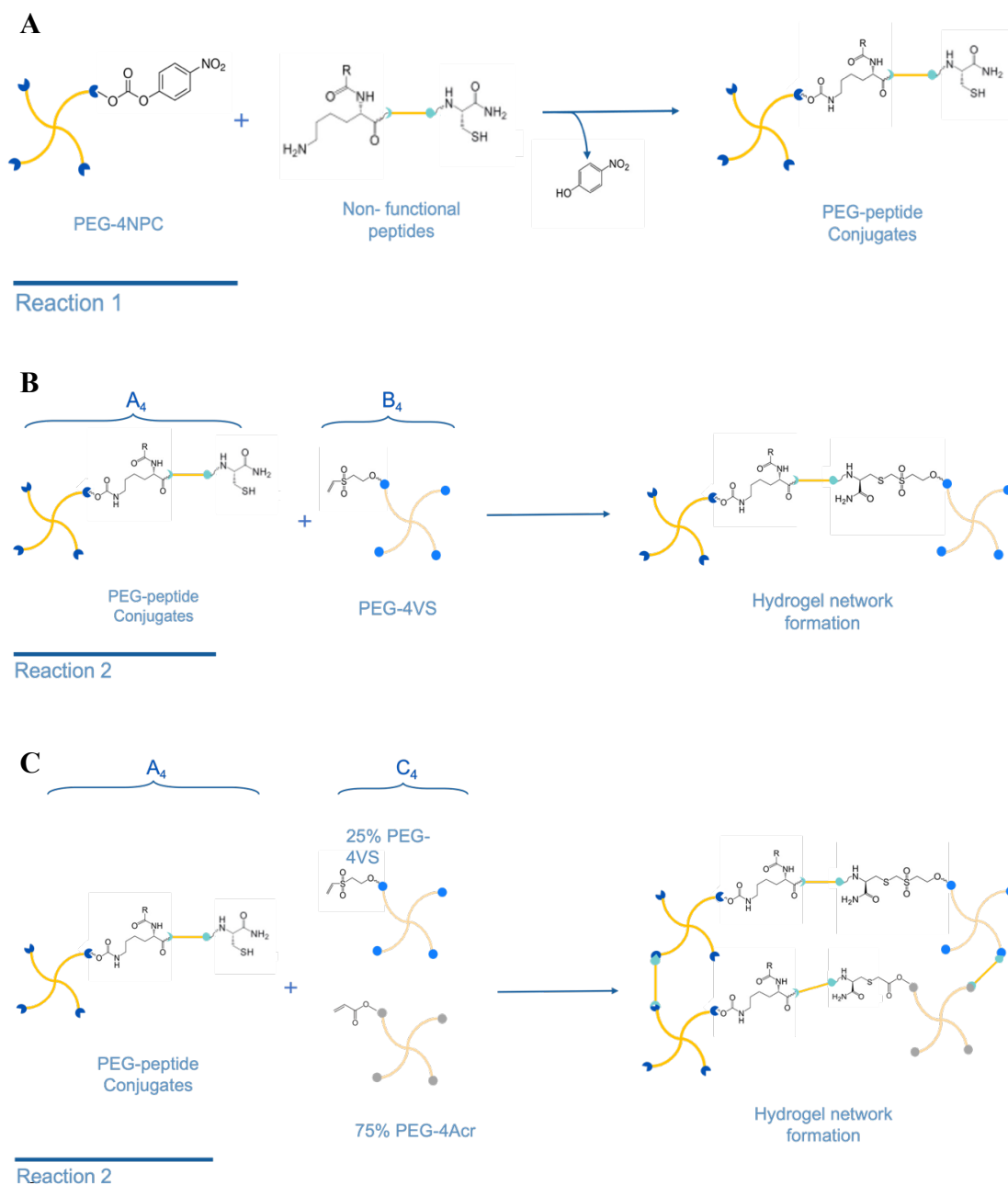


Figure 5.1 PEG-peptide hydrogel network fabrication.

A) PEG-peptide hydrogel design based on two reactions, first, PEG-4 NPC binds to a non-functional peptide (KDWERC) to form PEG-peptide conjugate with a solid content concentration 2.5%. **B)** This is followed by crosslinking with another PEG-4VS (non-degPEG) to form the hydrogel network. **C)** PEG-peptide modified hydrogel to form a deg-PEG; here PEG-peptide conjugate is crosslinked with 25% PEG-4VS and 75% PEG-4Acr to form the network.

A 100%PEG-4VS 100%PEG-4Acr 75%PEG-4Acr 50%PEG-4Acr

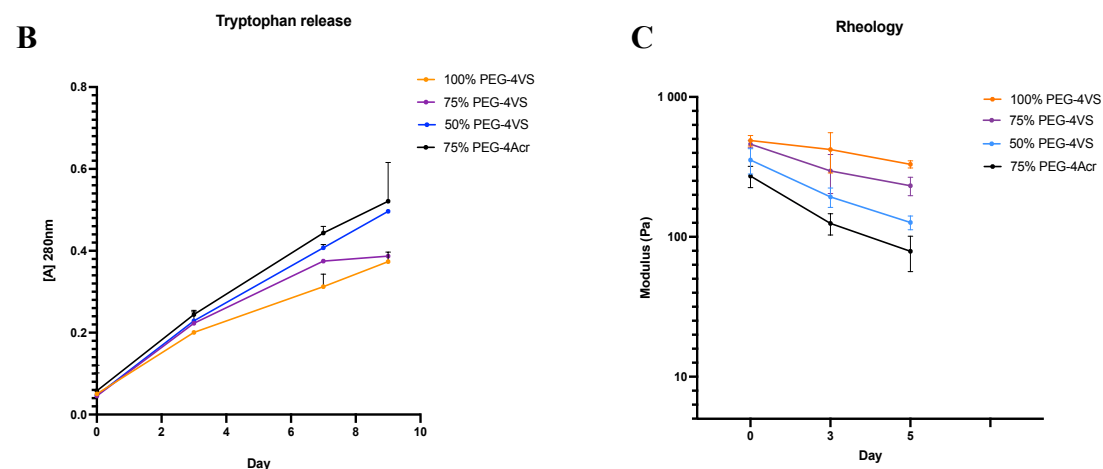
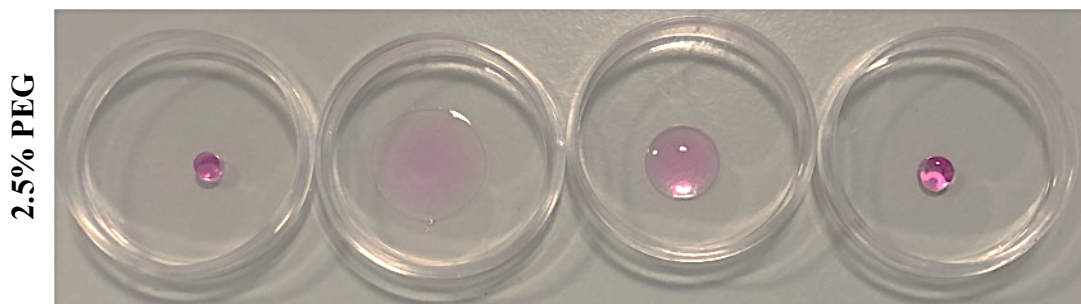


Figure 5.2 PEG-peptide hydrogels characterisation.

A) PEG-peptide hydrogels were formed at different conditions and monitored for 7 days. These images showed the degradability properties of the non-degPEG (100% PEG-4Acr), degPEG (75% PEG-4Acr), and selected control conditions 100% PEG-4Acr, 50-PEG-4Acr, and 75% PEG-4VS. **B)** Quantification of tryptophan release in the media (n=3 gels, bars SD). **C)** Rheology measurement showed the changes in hydrogel stiffness over time, the graph showed the high degradability in 75% PEG-4Acr, (n=3 gels, bars SD). (*Tryptophan assay and rheology measurements done by Alicja Kuziola*).

5.3 *PEG-peptide hydrogel encapsulation prevents morphological changes*

To determine the optimal PEG-peptide hydrogel (non-degPEG) stiffness supporting cell viability, hydrogels were formed with polymer concentrations of 2.5% (soft gel) and 5% (stiffer gel) conjugated with (Ac-CREW-ERC-NH₂) KDWERC. The cell culture experiment work is similar to the protocol in suspension (described in Chapter 3) when hiPSC spheroids formed after two days in culture in E8 medium, were harvested and encapsulated in the hydrogels (Figure 5.3 A). The hydrogels were crosslinked within 30-45 minutes. Encapsulated spheroids were then placed in (E8, KSR BMP4, and KSR) medium (the E8 BMP4 was not planned to be tested at this stage). Encapsulated spheroids in 2.5% PEG-peptide hydrogel prevented changes in morphology, and spheroids maintained round morphologies, unlike 3D models in suspension, whereas 5% PEG-peptide hydrogel resulted in poor spheroids structure, which showed fractures around the edges (Figure 5.3 B). These findings revealed that both soft and stiff gel impede morphogenesis, including sphere expansion in E8 (in 5% and 2.5%), elongation in KSR BMP4, and control conditions E8 BMP4 and KSR (in 2.5%).

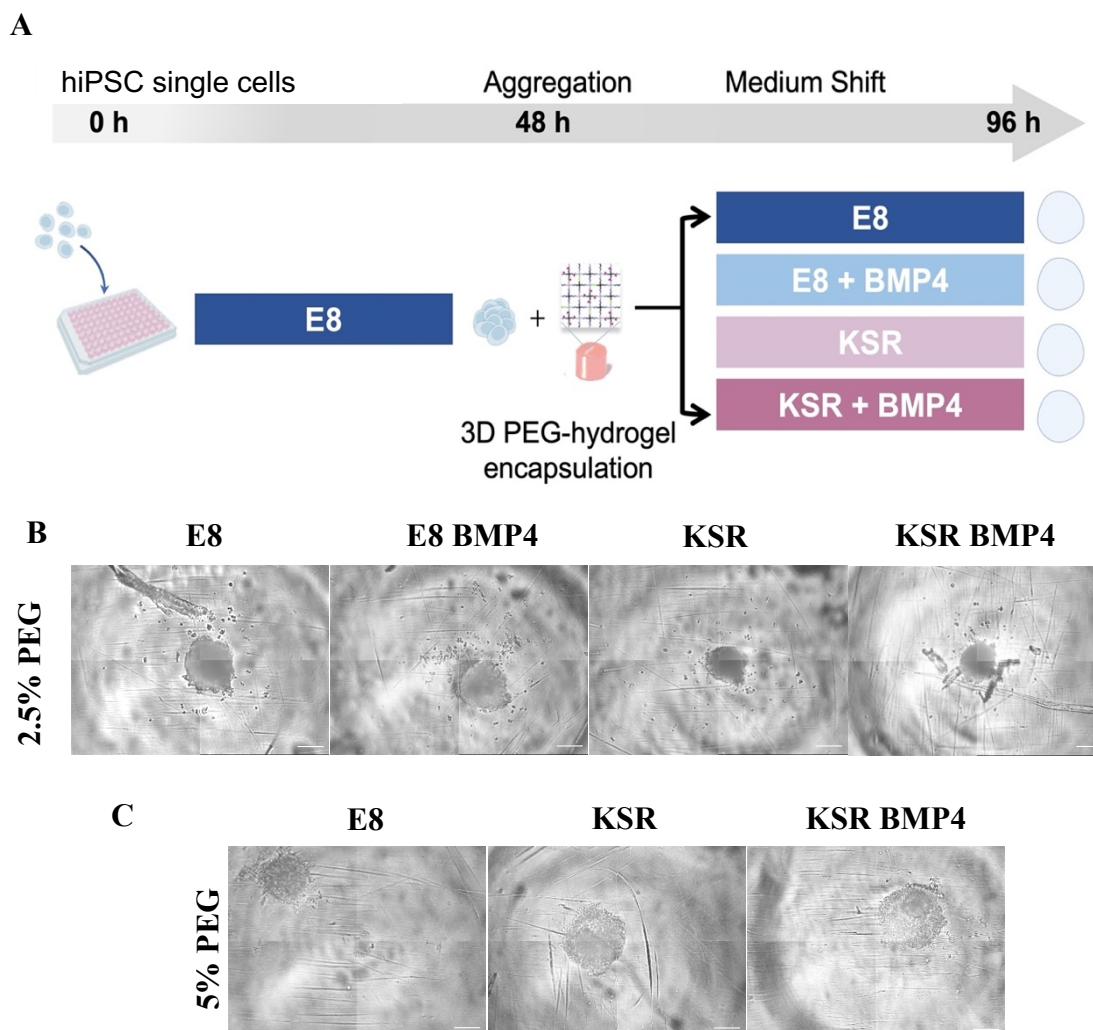


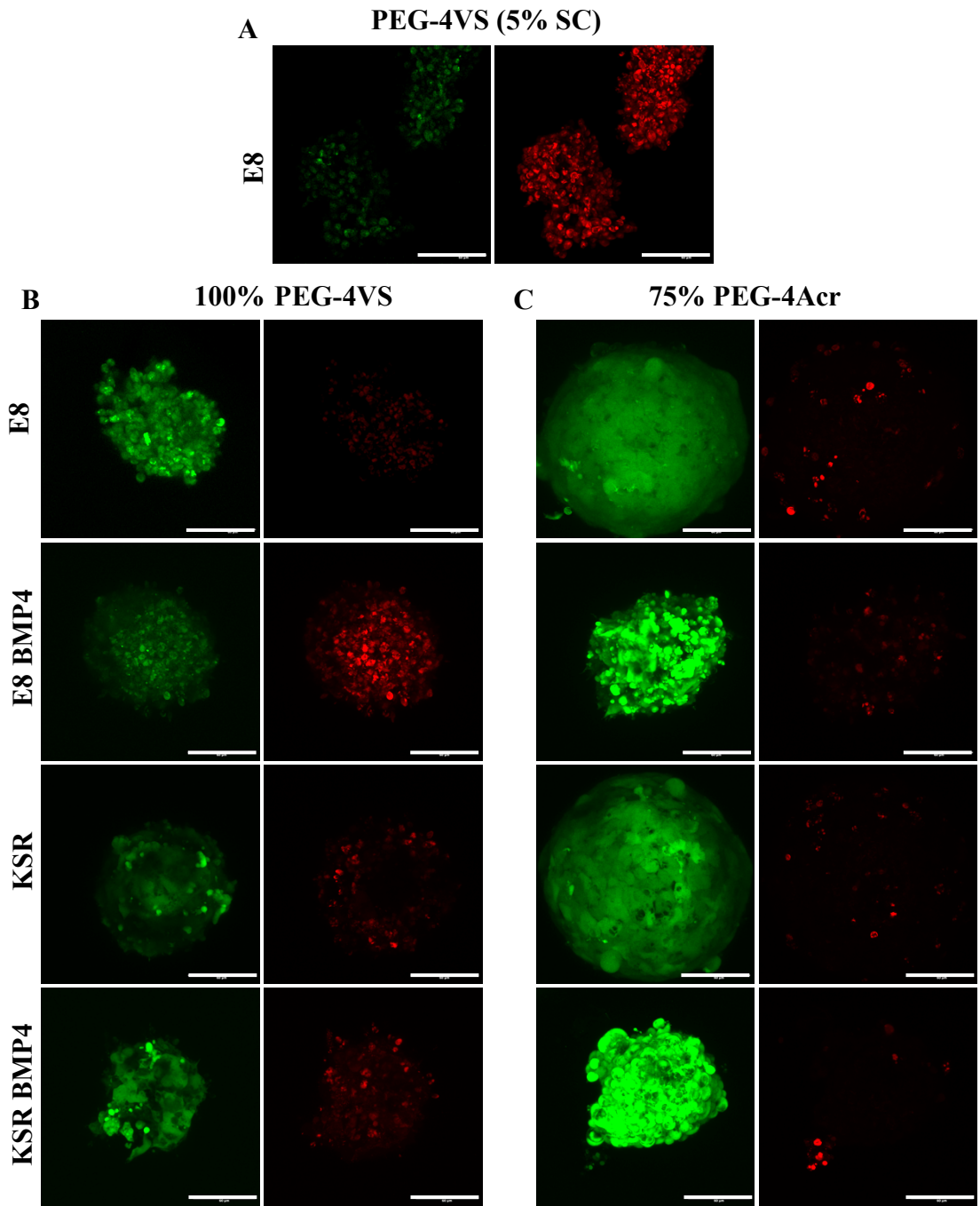
Figure 5.3 hiPSC encapsulation in PEG-peptide hydrogel prevents morphological changes.

A) Schematic of experiment workflow, hiPSC seeded in low attachment 96-wells plate in E8 medium for 2 days to form spheroids. After 2 days, hiPSC spheroids were encapsulated in non-degPEG (PEG-4VS) hydrogel, when the hydrogel is fully crosslinked medium was changed to E8, KSR BMP4 medium or control conditions E8 BMP4 and KSR medium. **B-C)** Optimisation of hydrogel encapsulation using different polymer concentrations to change the hydrogel properties, PEG-peptide hydrogels formed at different stiffness (2.5% and 5%) showed no morphological changes after 96 hours under different medium conditions; however, in 5% spheroids lose their compaction and showed fractured spheroid. Scale bars 200 μm .

5.4 *Soft PEG-peptide hydrogels promote cell viability*

Next, we sought to explore the effect of hydrogel stiffness on hiPSC viability when embedded in non-degPEG or deg-PEG after 96 hours. Cell viability assay was performed using live/dead staining after 96 hours in culture (Figure 4.4 A-D). First, E8 medium condition was used as a standard control to determine whether 2.5% or 5% non-degPEG hydrogels promote cell viability. Confocal images revealed that spheroids embedded in 2.5% polymer concentration non-degPEG exhibited fewer dead cells than the 5% non-degPEG (Figure 5.4 A-B). These results suggested that 2.5% non-degPEG promotes cell viability, which was then used to create the hydrogel for all further experiments.

Therefore, the hydrogel design was modulated by swapping the non-deg PEG with deg-PEG as previously described in (section 5.2) to determine if softening gels improve cell viability. Live/dead assay was performed for both hydrogel conditions after 96 hours of culture in (E8, KSR BMP4, E8 BMP4 and KSR) medium. The results showed that E8 medium spheroid exhibited more live cells in deg-PEG compared to the standard hydrogel condition non-degPEG (Figure 5.4 B-D). Embedded spheroids in KSR BMP4 also showed better survival than non-degPEG (Figure 5.4 B-D). Controls E8 BMP4 and KSR showed more viability in the modulated hydrogel (Figure 5.4 B-D). Overall, these readouts suggested that deg-PEG promotes cell viability and reduces apoptosis thus allowing spheroid growth.



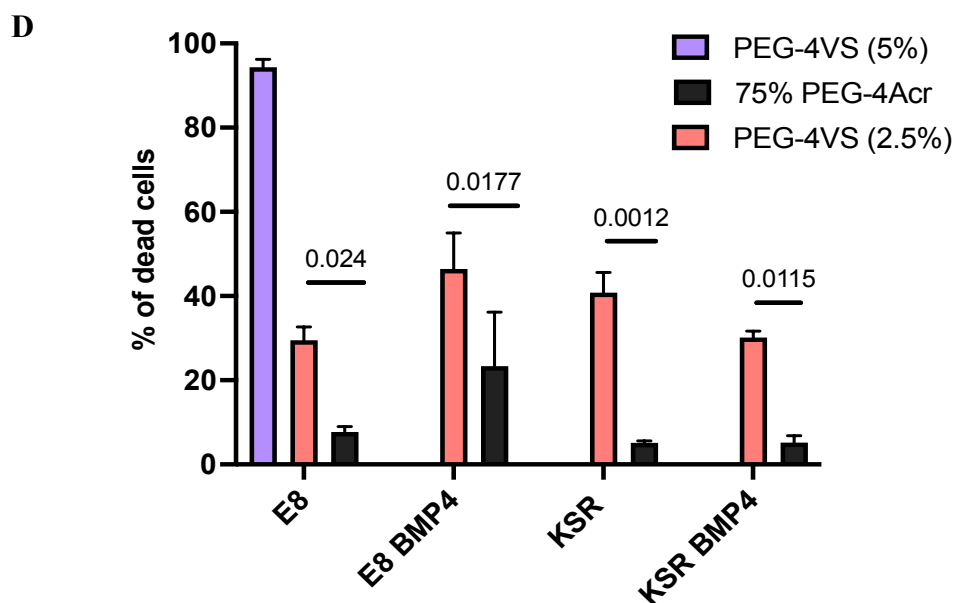
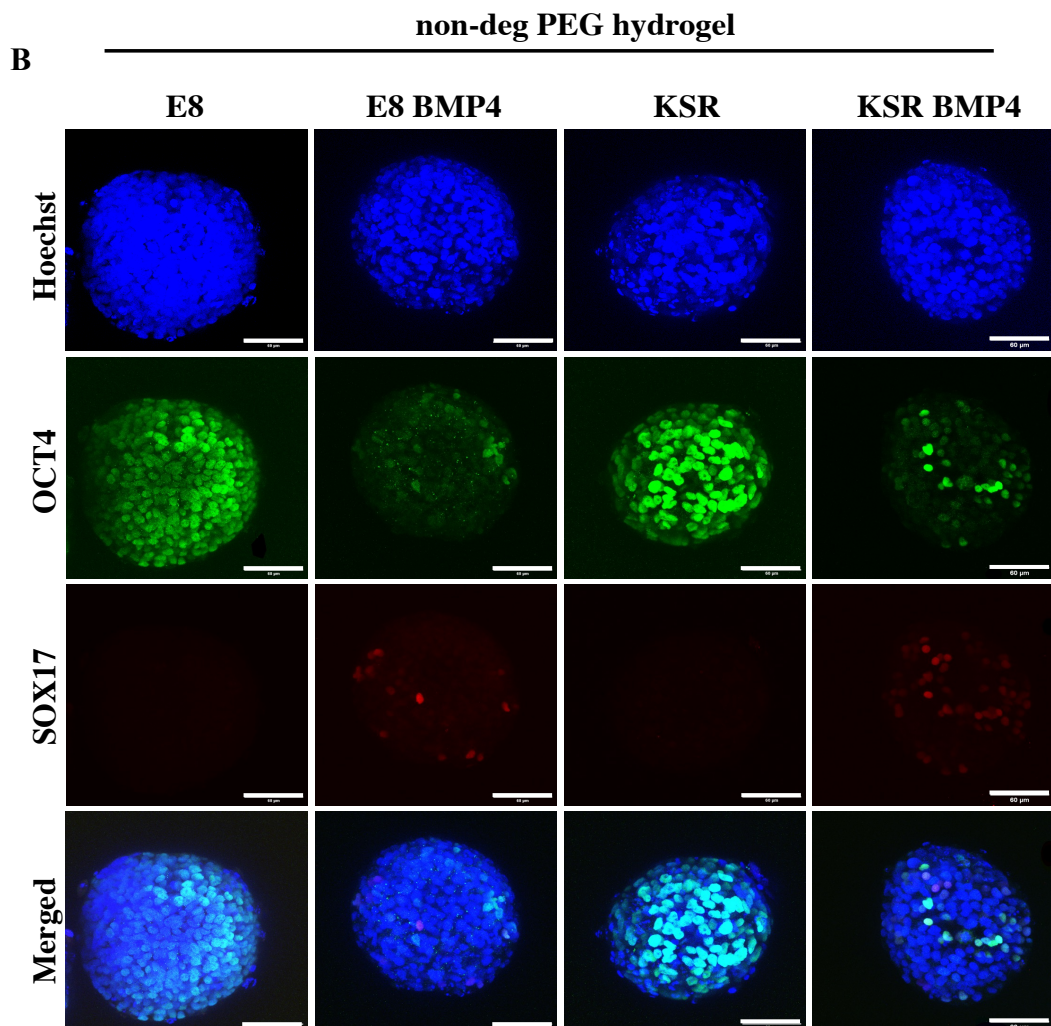
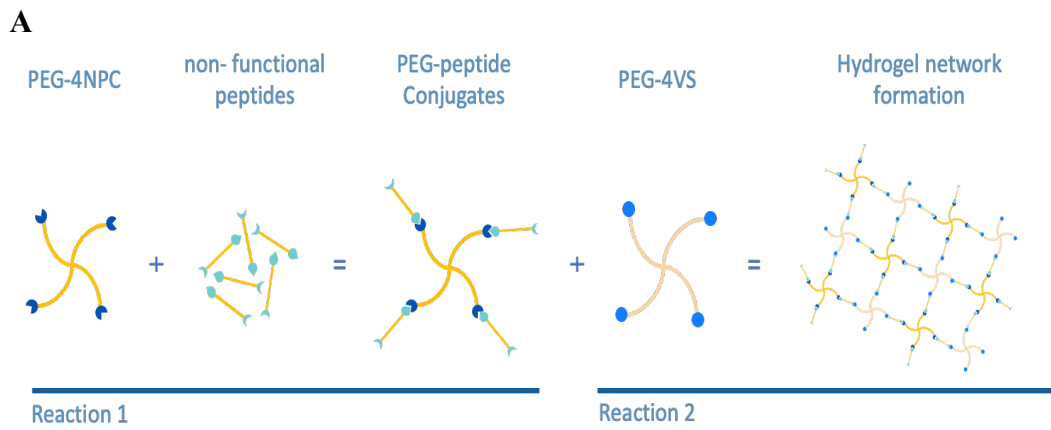


Figure 5.4 Cell viability in different hydrogel conditions.

Live (Green), Dead (Red) staining was performed after 96 hours in culture. **A)** hiPSC spheroids embedded in polymer concentration (5%) of non-degPEG and cultured in E8 medium showed excessive cell death. **B)** In contrast, cells encapsulated in softer gel 2.5% non-degPEG showed better survival in E8 medium condition, in KSR BMP4 and E8 BMP4 exhibited more dead cells. **C)** Modified hydrogel deg-PEG maintains a better environment that promotes spheroids growth and cell viability in all medium conditions compared to non-degPEG conditions. Scale bar 60 μ m. **D)** Quantification of the percentage of dead cells in each medium condition encapsulated in non-degPEG both stiff gel (5%), softer gels (2.5%) and deg-PEG, statistic test 2-way Anova (n= 4 spheroids, bars= mean and SD).

5.5 *Physical confinement disturbs the emergence of lineages specifications*

To address whether the differentiation of the three germ layers depends on changes in morphology, I postulated that physical confinement affects both morphogenesis and differentiation. As expected, when 3D spheroids embedded in 2.5% polymer concentration of non-degPEG hydrogel not only impeded changes in shape after 96 hours of BMP4 treatment but also resulted in significant downregulation of SOX17 (endoderm) expression (Figure 5.5 A-B, Figure 5.7 B) compared to 3D spheroid in suspension (see Chapter 4, Figure 4.1A). Confined spheroids in E8 medium exhibited high levels of the pluripotency marker OCT4, with negative SOX17 expression, whereas in KSR BMP4 medium spheroids exhibited a significant reduction in OCT4 marker and dramatically low SOX17 expression (Figure 5.5 B, Figure 5.7 A-B). In control conditions, when embedded spheroids were cultured in E8 BMP4 medium, this resulted in a significant reduction in the pluripotency marker and extremely low expression of SOX17 (Figure 5.5 B, Figure 5.7 A-B). In the KSR medium, spheroids maintain high expression of the OCT4 marker and inhibition of the SOX17 marker comparable to the self-renewing condition E8 medium (Figure 5.5 B, Figure 5.7 A-B). This indicated that upon confinement, cells did not undergo differentiation when cultured in KSR medium. Moreover, I stained for BRA marker (mesoderm) the results showed negative expression of BRA in all medium conditions (E8, KSR BMP4, E8 BMP4, and KSR)- images are not shown. Immunostaining was performed for secondary antibodies control as shown in (Figure 5.5 D). Overall, these results confirmed that embedding hiPSC in a confined environment blocks morphogenesis and revealed that despite the addition of BMP4 conditions were not sufficient to promote SOX17 expression.



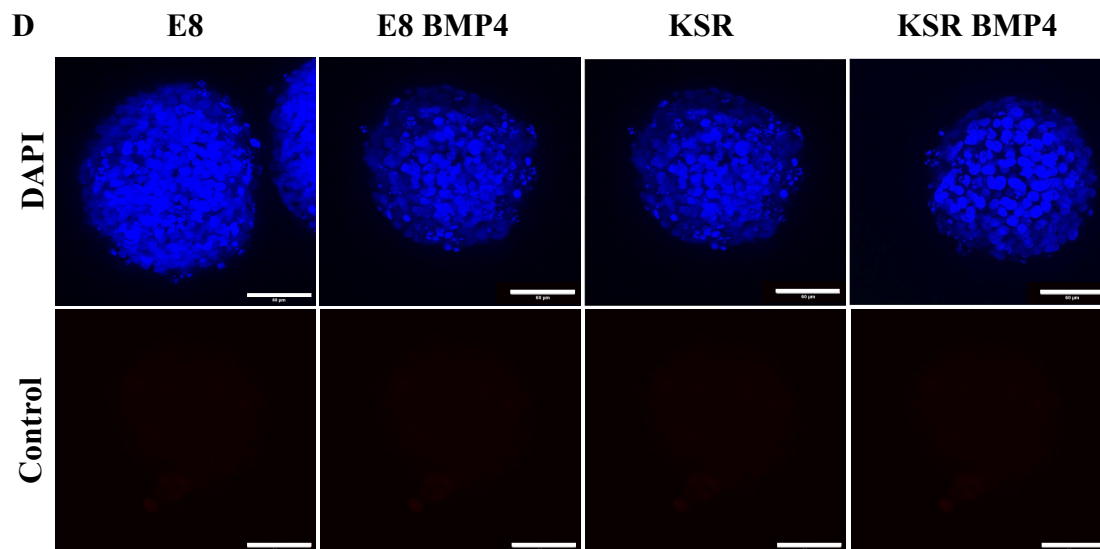


Figure 5.5 hiPSC spheroids encapsulated in non-degPEG and the emergence of SOX17 expression.

A) A Schematic diagram for non-degPEG hydrogel formation by crosslinking peptide conjugate with 100% PEG-4VS. **B)** Spheroids encapsulated in non-degPEG for 96 hours and immunostained for OCT4 and SOX17 markers. In E8 medium spheroid maintained high OCT4 expression, whereas reduction in OCT4 was observed in KSR BMP4 and E8 BMP4 conditions, however high OCT4 expression was detected in KSR condition. SOX17 was not detected in E8 medium condition, low SOX17 expression was observed in spheroid cultured in KSR BMP4. In control conditions, SOX17 low expression was detected in E8 BMP4, and in KSR the marker was not expressed. **D)** Immunostaining control for secondary antibodies (Alexa fluor 488 and 633), DAPI (top), and Controls (bottom). Scale bar 60 μm .

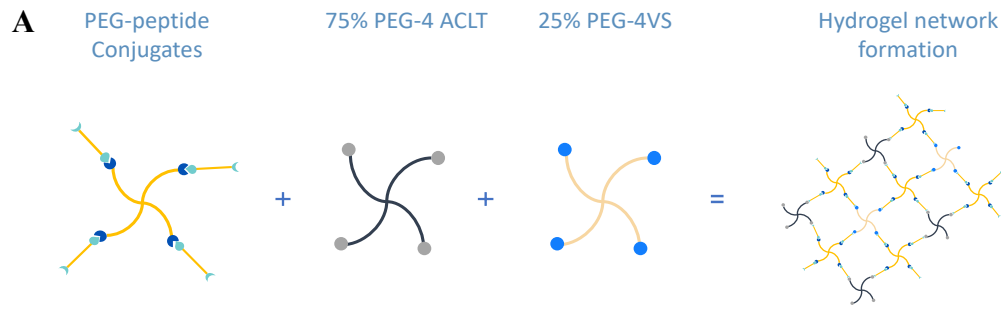
5.6 *Modulating PEG-peptide degradability promotes SOX17 expression*

Based on the previous observation SOX17 stimulation was dramatically reduced and the BRA expression was inhibited completely (BRA staining is not shown) when spheroids were cultured in a confined environment. This led us to investigate whether a 3D hydrogel that was not as rigidly confining would be more permissive to differentiation given the same biochemical signals.

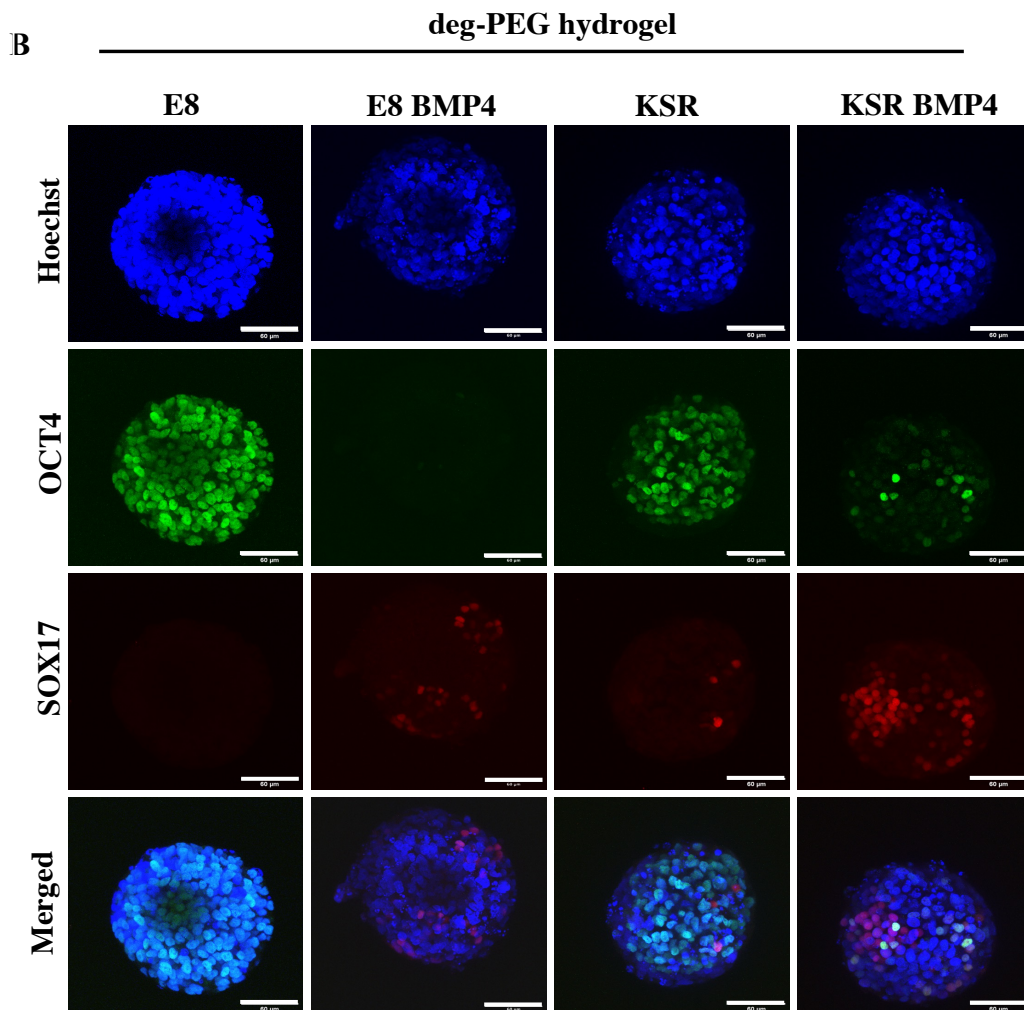
I stained for OCT4 and SOX17 markers to determine whether deg-PEG influences endoderm specification. The immunostaining after 96 hours of culture showed that in self-renewing condition (E8 medium) encapsulated spheroids within deg-PEG hydrogels maintained high expression of OCT4 pluripotency marker and negative expression of

SOX17 (Figure 5.6 A-B). As expected, in the KSR BMP4 medium condition, significant reduction of OCT4 marker was observed, also an increase of SOX17 expression was identified compared to non-degPEG (Figure 5.6 B; Figure 5.7 A-B). When spheroids were encapsulated in deg-PEG and cultured in E8 BMP4, OCT4 remained downregulated, and a significant increase in SOX17 expression was seen in contrast to embedded spheroid in non-deg-PEG (Figure 5.6 B; Figure 5.7 A-B) Furthermore, spheroids were embedded in deg-PEG and cultured in the KSR medium resulted in significantly reduce of OCT4 marker expression when compared to non-degPEG condition. Also, SOX17 expression remains low in this condition (Figure 5.6 B; Figure 5.7 A-B). Similar to non-degPEG, the mesoderm marker BRA in all medium conditions was negative and had no sign of BRA expression (is not shown in the Figures). This assessment was combined with the control immunostaining for secondary antibodies (Figure 5.6 D).

PHYSICAL CONFINEMENT INFLUENCES MORPHOLOGICAL CHANGES AND EXPRESSION
OF LINEAGE SPECIFICATION MARKERS



Reaction 2



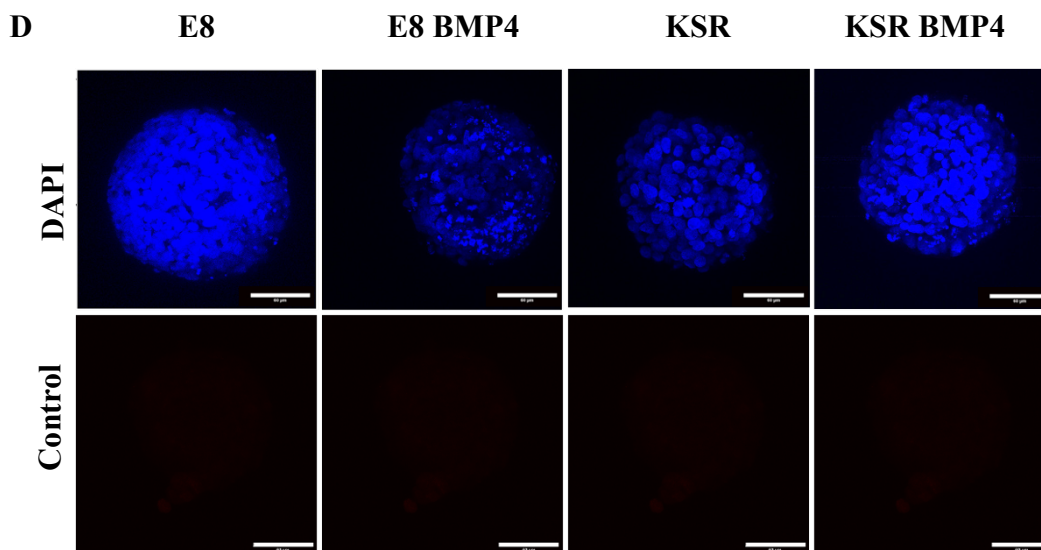


Figure 5.6 hiPSC Spheroids post-encapsulation in 75%PEG-4Acr and SOX17 expression.

A) Modifying hydrogel design to obtain deg-PEG hydrogel by crosslinking peptide conjugate with 75% PEG-deg and 25% PEG-4VS. **B)** Spheroids after being encapsulated in deg-PEG for 96 hours. Immunostaining images showed OCT4 and SOX17 expression in defined medium conditions. In E8 medium, the spheroid maintained high expression of OCT4, as expected in both KSR BMP4, E8 BMP4, and KSR showed OCT4 reduction. In E8 condition, SOX17 marker was not expressed, in contrast, an increase of SOX17 marker was detected in KSR BMP4 and E8 BMP4, and low expression was seen in KSR. **D)** Images show immunostaining control for secondary antibodies (Alexa fluor 488 and 633), DAPI (top), and Controls (bottom). Scale bar 60 μm .

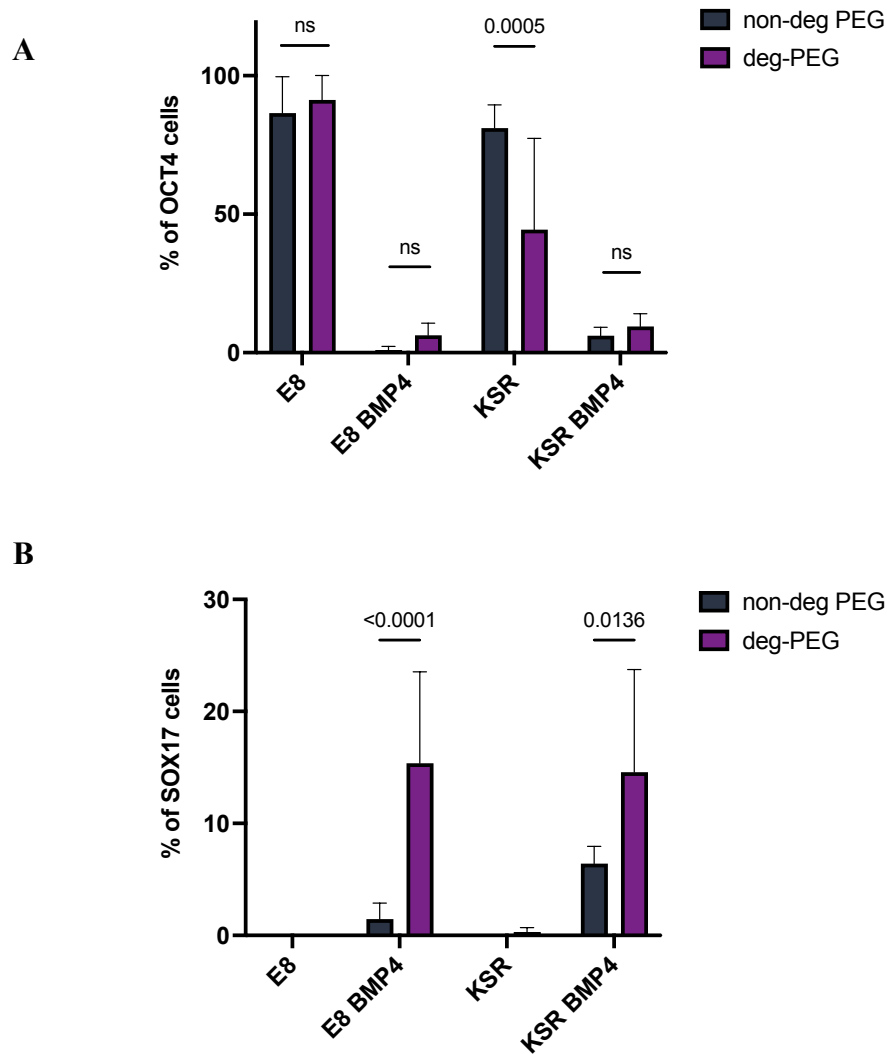


Figure 5.7 Diverse expression of OCT4 and SOX17 markers in non-deg PEG and deg-PEG hydrogels.

A) Quantification of the percentage of positive cells expressing OCT4 in non-deg PEG hydrogel compared to deg-PEG hydrogel cultured in E8, KSR BMP4, E8 BMP4 and KSR, statistic 2-way Anova (n= 8 spheroids per condition, P-value =0.0005, bars= mean and SD). **B)** Quantification of the percentage of SOX17-positive cells non-deg PEG hydrogel showing the significant reduction in KSR BMP4 and E8 BMP4 compared to deg-PEG hydrogel, statistic 2-way Anova (n= 8 spheroids per condition, P-value <0.0001, P< 0.05, bars= mean and SD).

5.7 Discussion

Morphogenesis and the specification of three germ layers during gastrulation are controlled by morphogen signalling to induce lineage specification and mediated by physical signals between cells and remarkably the local tissue environment (Muncie et al., 2020). Understanding the contribution of biochemical and physical factors on governing differentiation and shape changes in free-floating 3D models is challenging (Vianello and Lutolf, 2019). Thus, the use of PEG-based hydrogels by tuning the physical properties, including stiffness and degradability, enables interrogating if physical confinement affects morphogenesis and differentiation (Gjorevski et al., 2016). In this Chapter, we sought to investigate if morphogenesis is required to obtain appropriate lineages of three germ layers within an organised manner. To address this question 3D hiPSC spheroids were embedded in well-defined PEG-peptide hydrogels and varying stiffness and degradability. Comparing self-renewing versus differentiation medium gives rise to distinct morphological changes and the emergence of lineages specification in suspension as described in (Chapters 3 and 4). Herein, our findings revealed that physical confinement prevented elongation thus disturbing the SOX17 differentiation. Also, the expression of BRA was completely negative (not shown in the figures of this thesis). Modulating hydrogel stiffness and swapping to a more degradable hydrogel that softens over time showed remarkable stimulation of SOX17 expression, with the lack of SOX17 polarisation when compared to 3D in suspension.

PEG-based hydrogels are often used to study the role intrinsic mechanical cues play in supporting intestinal organoids and controlling neural tube morphogenesis (Gupta et al., 2021, Ranga et al., 2014). The hydrogel system was previously established by Lutolf's group using 8-arm PEG-VS and PEG-Acr. The hydrogel system was functionalised by transglutaminase factor (FXIIIa) which was identified to crosslink with some ECM compositions such as fibronectin (Gjorevski and Lutolf, 2017, Ehrbar et al., 2007). Another system that has been reported is the use of (A₂+B₄) design in which PEG-based hydrogels initially functionalised with two identical bifunctional peptides this resulted in reacting towards the chain end of any PEG arm thus affecting network efficiency (Sakai et al., 2008, Jowett et al., 2021). This limitation is fundamental when creating low polymer concentration hydrogel such as 2.5% resulting in poor network formation and

gelation which changes hydrogels' mechanical properties (Jowett et al., 2021). Nevertheless, our hydrogel-described platform overcame the limitation of the enzymatic reaction and insufficient network formation using a tetra-PEG-based system and hetero-bifunctional peptide on the bases of (A₄+B₄) or (A₄+C₄) design. Thus, this allows a much higher homogenous network resulting in better network efficiency, especially when creating low polymer concentration hydrogels (Jowett et al., 2021, Lust et al., 2021). A previous study claimed that PEG-Acr hydrogels could not be formed below 4% polymer concentration (Phelps et al., 2012), however, we were able to form PEG-Acr at 2.5% concentration for both 100% PEG-Acr and 75% PEG-Acr (deg-PEG). These results emphasise the high network efficiency with other existing hydrogel systems. Nonetheless, a limitation of mechanical assay of the hydrogels systems when formulating non-degPEG and deg-PEG hydrogels at the same polymer concentration (in our condition 2.5%) due to the differences of the initial stiffness between systems. To overcome this deg-PEG hydrogel should be formed at a higher polymer concentration (i.e., 3% or 3.5%) which should be measured using rheology assessment to validate that both non-degPEG and deg-PEG hydrogels show the same mechanical properties (initial stiffness).

Unlike 3D spheroids in suspension (in Chapter 4), when hiPSC spheroids are embedded in 2.5% PEG hydrogels in both (non-degPEG and deg-PEG) maintained round shape and morphological changes were not observed post-culturing in different mediums. This indicates that soft hydrogels retain enough constraint to prevent axis formation thus, elongation implying that changes in shape are driven by cellular movement in the 3D structure (Gupta et al., 2021). Recently, the effect of matrix properties on hiPSC morphogenesis using alginate hydrogels has been investigated by modifying stiffness and adhesion properties. Their findings determined that fast relaxing alginate (fast softening over time) promotes spheroids growth and cell viability, and incorporating RGD ligand supports the lumen formation (Indana et al., 2021). The impact of stiffness is consistent with our results; spheroids in 5% non-degPEG (100% PEG-4VS) showed very low viability compared to 2.5% soft gel both non-degPEG and deg-PEG. This indicates that restriction in growth and cell apoptosis is likely due to lack of nutrient and oxygen diffusions to the core of spheroids in the rigid matrix.

Moreover, modulating non-degPEG hydrogel by changing the crosslinking composition to deg-PEG improved the cell viability of 3D spheroids cultured in (E8, KSR BMP4, E8 BMP4 and KSR). The reason behind these observations could be the different mechanical properties since deg-PEG undergo hydrolysis over time via breaking the ester bonds, which degrades the network and presumably allows for cell growth (Khan et al., 2020). It has been reported in several studies that degradable hydrogel promotes viability and proliferation due to the matrix elasticity (Caiazza et al., 2016, Indana et al., 2021, Ranga et al., 2016). When single mESC are embedded in soft PEG-based hydrogel, they maintain a moderate viability rate similar to a standard 2D gelatine-coated culture condition (Caiazza et al., 2016). Nevertheless, the rate of biochemical cues diffusion in the hydrogel system, perhaps regulated by stiffness and mesh size, impacts viability and cell activity during encapsulation. In this context, a recent study on our hydrogel system revealed that the stiffness could be modulated without affecting the ability of nutrients and biochemical cues diffusions for polymer concentrations up to 5% (Lust et al., 2021). The advantage of deg-PEG (PEG-4Acr) is the ability to softening over time hydrogel to non-degPEG (PEG-4VS), which overcomes the limitation of hydrogel formation at a lower concentration as 1% is viscous liquids (Lust et al., 2021). This might be similar to the effect of degradable hydrogels via MMPs in intestinal organoids allowing for matrix remodelling and inducing cell proliferation and growth (Jowett et al., 2021). However, this type of hydrogel was not tested in this 3D model of gastrulation. Taking these findings together, in response to degradability in deg-PEG allows for better cell viability compared to the non-degPEG.

The inability of spheroids to change shape interfered with the expression of SOX17 (endoderm) and blocked BRA (mesoderm) expression after embedding in both non-degPEG and deg-PEG. In suspension culture, the spheroids consistently gave rise to the three germ layers in an organised pattern, which was absent in the encapsulated spheroids. The results showed that in non-degPEG, spheroids cultured in E8 medium were able to maintain high expression of the pluripotency marker OCT4, likewise in the deg-PEG hydrogel. These observations indicated that physical confinement in soft hydrogels promotes OCT4 expression under undifferentiated conditions. Surprisingly, KSR medium cells showed an increase in OCT4 marker expression similar to the E8 medium condition in the PEG-4VS, whereas the deg-PEG OCT4 was slightly downregulated. A

study by Lutolf's group revealed the optimal microenvironment (degradable and soft) of PEG-based hydrogel to promote high levels of pluripotency markers expression (Caiazzo et al., 2016). The emergence of the SOX17 marker was significantly reduced, and random expression was observed under differentiation conditions, in addition to the loss of polarisation phenotype in the KSR BMP4 medium compared to 3D spheroids in suspension. However, deg-PEG hydrogel promotes SOX17 in KSR BMP4 and E8 BMP4, suggesting that SOX17 expression favours degradable/softer gel. Several findings demonstrated that the mechanical properties of the cell surrounding the microenvironment control cell fate decisions (Ranga et al., 2014, Gjorevski et al., 2016, Vining and Mooney, 2017).

The emergence of SOX17 positive cells was explored in a 2D topography model, hESC were seeded on top of soft matrices targeted endodermal differentiation while this marker was reduced when cells were cultured on a stiffer surface (Rasmussen et al., 2016). A recent study reported that when hESC were seeded on top of a rigid substrate (2700 Pa), post-BMP4 treatment triggered a mesodermal specification (Muncie et al., 2020). This explains our observation of BRA inhibition in soft hydrogel but non-degPEG and deg-PEG with initial ($G' \sim 400$ Pa) stiffness. In addition, SOX2 was not explored in the embedded 3D hiPSC, which will be noteworthy to investigate. A recent study of a 3D model of neural progenitor cells showed that the SOX2 marker was highly expressed in the degradable hydrogels (Madl et al., 2019). The physical properties of the native tissue vary during developmental stages *in vivo*, which regulate the differentiation process towards the three germ layers (Rasmussen et al., 2016, Muncie et al., 2020).

Overall, the data in this Chapter suggests that tissue morphogenesis is required to obtain a proper differentiation of the three germ layers. The emergence of the endodermal and the lack of mesodermal expression showed that mechanical properties play a crucial role to maintain differentiation during development. Based on the observation of SOX17 expression when spheroid was embedded in deg-PEG, further experiments were conducted to modulate hydrogel properties using degradable sequences (MMPs). The MMPs can break down the peptide sequence allowing hydrogel to soften, thus may facilitate spheroids growth or elongation. It has been reported that MMPs activity in 3D mouse ESCs mediates basement membrane remodelling, which promotes spheroids

growth and the formation of the primitive streak (Kyprianou et al., 2020). Investigating this may give additional insight into the ability of 3D hiPSC to remodel the surrounding environment which might allow the spheroids to elongate.

6 DISCUSSION & FUTURE DIRECTIONS

6.1 *Discussion*

During early embryogenesis, the emergence of the three lineages (ectoderm, mesoderm and endoderm) is coupled with dynamic changes in morphology through forming the A-P axis in the human embryo (Arnold and Robertson, 2009). The underlying mechanisms of the signalling pathway (BMP4, NODAL, WNT and FGF) involved in generating self-organised germ layers on defined geometrical size have been extensively investigated in 2D micropattern models (Siggia and Warmflash, 2018, Tewary et al., 2017). Therefore, morphogenesis is an important event during gastrulation, which is highly regulated by physical cues between (cell-cell) or external physical forces from the tissue environment of the uterus (Vianello and Lutolf, 2019). Much less is understood about how biochemical cues and physical cues trigger tissue rearrangements and whether they are regulated mechanically (tissue environment) or biochemically (cellular response) (Vianello and Lutolf, 2019, Trubuil et al., 2021). The main aim of this project is to explore how biochemical cues (BMP4/ KSR) and physical confinement separately influences morphogenesis and differentiation in a 3D hiPSC model of gastrulation. To achieve this, I proposed an adapted method of a previously well-defined 2D micropattern system based on a BMP4 treatment (Warmflash et al., 2014) in a 3D model that shows both axial formation and tri-lineage specification incorporating PEG-peptide hydrogels to prevent elongation. This platform allows us to question whether morphogenesis is required to direct lineage differentiation and patterning.

The hiPSC in a 3D model of gastrulation of standardised size cultured under distinct medium conditions (E8, KSR BMP4, and their controls E8 BMP4 and KSR) were characterised to quantify the consistent changes in morphology in (Chapter 3). The developed platform decouples the biochemical and physical cues allowing us to control each parameter. Our results demonstrated that biochemical signals trigger morphological changes observing spherical shape in E8 and axial elongation in KSR BMP4. However, in E8 BMP4, spheroids maintained a small spherical shape that tends to form small buds, and when spheroids were cultured in KSR formed an intermediate shape that underwent

spontaneous buds formation. High-content analysis approaches to obtain quantitative readouts from digital microscopy images provide distinctive automated multi-parametric data to quantify cell behaviours (Mattiuzzi Usaj et al., 2016). In this context, a robust high-content live imaging method was employed to monitor the 3D spheroids' behaviour, this generates brightfield images of 96 time-points which are then used as readouts to quantify changes in shape and area. Quantification and segmentation of the 3D spheroids phase contrast images are challenging and only often compatible with acquiring further analysis. We successfully described a novel image analysis method using CellProfiler that can be easily used to obtain an efficient analysis of 3D spheroids quantifying area, size, shape, and roundness (Alsehli et al., 2021). This pipeline exploits live images based on background subtraction of pixel intensities of two following time points producing an image of the spheroid structure only called (Delta). This Delta image was used effectively to segment the spheroids, generating datasets that capture the morphological variation of diverse culture conditions (Alsehli et al., 2021).

One of the main findings in (Chapter 4) is that adding BMP4 to the differentiation medium (KSR medium) stimulates reproducible differentiation of the tri-germ layers in suspension. Several studies investigated the effect of the BMP4 signalling pathway to form a radial pattern of the three lineages in the 2D micropattern system (Warmflash et al., 2014, Vickers et al., 2021, Tewary et al., 2017). However, previously described 3D models revealed that ESCs treated with BMP4 were not able to form axial elongation and differentiation toward the three germ layers (Baillie-Benson et al., 2020, Moris et al., 2020). Our data also showed that biochemical cues BMP4 and KSR play a role in promoting morphogenesis and shape changes by regulating proliferation and cellular tension (F-actin, and YAP) in the 3D gastrulation models. The EdU staining demonstrated that cell proliferation highly depended on the medium composition (BMP4 and KSR).

The addition of BMP4 to E8 medium reduces the proliferation; however, in KSR alone, the proliferation tends to polarise more toward the budding area. These findings elucidate the observation in the KSR BMP4 medium, which showed that the proliferation is restricted to the elongated tip. Moreover, the phalloidin staining revealed that the F-actin network is distributed differently in response to the biochemical cues. Highlighting the

KSR BMP4 condition, F-actin is expressed more around the edges suggesting that F-actin produces tension along the periphery of the 3D structure to direct the A-P elongation. This finding is also supported by the nuclear YAP expression indicating the presence of cellular tension in the elongated area of the KSR BMP4 condition. Together, these readouts implied that axial elongation and the differentiation of the three germ layers on the anterior side occurred due to the crosstalk between the biochemical signal that drives proliferation and physical forces generated from the F-actin distribution. This has been reported during gastrulation *in vivo*; the sequence of morphogenesis events and lineages specification in early stages are regulated by the interplay between morphogen signalling and physical forces generated by cell-cell adhesion or cytoskeletal tension (Vianello and Lutolf, 2019, Kim et al., 2018b). These outcomes allow further investigation of physical forces generated by cell-cell adhesion or actomyosin contractility.

Following on the previous observations suggesting that the three germ layers differentiation could rely on shape changes in free-floating culture, in (Chapter 5) the aim is to explore this by impeding changes in morphology using PEG-based hydrogels. The physical confinement using (our in-house) PEG-4VS with a determined stiffness of 2.5% polymer concentration prevents morphological changes, dramatically reduces the expression of SOX17 and inhibits the BRA marker (mesoderm). To identify if modulating non-degPEG hydrogel degradability by altering the hydrogel crosslinking with deg-PEG promotes morphogenesis and differentiation. Similar to the non-degPEG, the modified deg-PEG did not promote elongation; however, it stimulated SOX17 expression in KSR BMP4 and E8 BMP4 conditions and BRA was not detected. Here, the focus was mainly on the SOX17 marker (endoderm) expressed in KSR BMP4 (located at the tip) and E8 BMP4 (in the small bud) in suspension. Using the PEG-peptide hydrogels system as a tool to block the elongation or small budding from happening enabled us to determine that morphogenesis is crucial to induce the formation of the three germ layers in an organised manner. Not to exclude that modulating PEG-peptide hydrogel properties promoted SOX17 expression and cell viability. These suggested soft hydrogels favour the differentiation toward SOX17 expression, while stiff hydrogels notably direct differentiation toward BRA expression (Muncie et al., 2020, Rasmussen et al., 2016).

Overall, this approach enables us to dissect the inter-correlation of 3D hiPSC spheroids' changes in shape with the patterning of germ layers.

6.1.1 Strengths

Morphogenesis and cell fate specification of a normal early embryo requires incorporating biochemical and biophysical signals from the native microenvironment (Lenne et al., 2021, Arnold and Robertson, 2009). In this thesis, the proposed methods of hiPSC-derived 3D gastrulation-like models have several strengths. This platform allows the decoupling of both biochemical and physical cues by comparing the medium and PEG-based hydrogel conditions offering the opportunity to investigate how the two processes coordinate to influence germ layers differentiation. BMP4 morphogen triggers pattern formation in 2D micropattern, mirroring the signalling pathway in early embryonic development. At the same time, in 3D model, it has been substituted with pulses of the WNT agonist CHIRON (Siggia and Warmflash, 2018, Moris et al., 2020, Morris et al., 2012). To the best of my knowledge, no previous work has published a 3D model of gastrulation using hiPSC treated with BMP4 to characterise differentiation propensity and the impact of physical confinement. It has been reported that hiPSC could experience high chances of genetic variations during each step in the culture (Volpato and Webber, 2020, Schwartzenruber et al., 2018). This 3D differentiation protocol minimises the steps of single-cell dissociation and reaggregation. It bypasses the CHIRON pulse step in a routine culture which could reduce the possible hiPSC heterogeneity during routine culture. Another study using hESC 2D micropattern determined that BMP4 stimuli resulted in a fast commitment to lineage specification and downregulate pluripotency (Gunne-Braden et al., 2020), which has yet to be investigated in 3D.

The 3D protocol produces a standardised spheroid that generates a reproducible morphology under the selected medium conditions (E8, KSR BMP4, E8 BMP4 and KSR) in a 96-well plate. The high-throughput 96-well V-bottom plate platform enabled monitoring of single spheroid behaviour per well via high-content live imaging. This powerful tool generates automated phenotypic data for each spheroid (24 replicates/per medium condition) at a time per cell line. In addition, the created pipeline for integrating high-throughput screening and profiling of spheroids for live imaging enabled efficient

segmentation of simple phase-contrast images which can be implemented easily for other 3D spheroid models (Alsehli et al., 2021). For example, this protocol can be used to test inhibitor molecules for screening purposes to capture the impact on morphogenesis and quantify shape changes including (roundness, deformation, and area).

The use of HipSci cell lines is a potential tool in this project which was developed to generate a large number of hiPSC lines from healthy individuals and donors with genetic diseases (Kilpinen et al., 2017). The cell lines are derived and characterised for genomic (DNA sequencing), and phenotypic analysis, including cell shape, proliferation and proteomic assays (Kilpinen et al., 2017, Vigilante et al., 2019). These data are available through the website (www.hipsci.org), which enabled us to choose the Hoik_1 line for the high-quality control in culture and the absence of possible genetic variation. This study facilitates the investigation of phenotypic outliers related to the germ layers differentiation or adhesions and possible variations between the cell lines of different donors (Vigilante et al., 2019). This will provide remarkable improvement in the hiPSC drug screening or disease modelling by exploring the variability in cell behaviour per hiPSC lines.

Moreover, developing a 3D model of gastrulation using BMP4 stimuli was important to us in parallel with previous work on 2D micropatterned by Fiona Watt's group investigating the impact of genetic variation on differentiation of selected hiPSC lines (Vickers et al., 2021, Tewary et al., 2017). Building upon this study using the identified outliers hiPSC in 3D would be interesting to explore whether these phenotypes are restricted for 2D, and question if more genetic variants might occur in the germ layers in 3D or elongation. Overall, the proposed 3D model in my thesis could be used to investigate the influence of genetic variants not only differentiation-related but also ECM receptors or cell adhesion, including F-actin or cell tensions (YAP) that impact morphogenesis.

The employment of the PEG-peptide hydrogels system in this project allows for dissecting the role of how physical properties influence morphogenesis, thus, germ layers differentiation. The (non-adhesive/non-degradable) conjugated peptide used in the hydrogel formation for this study provides only a physical barrier without interaction with

spheroids' biological activity. For this reason, this system is well-suited to the aims of this thesis, exploring the causative effect of changes in shape on differentiation. However, the platform can be further modified by incorporating adhesive (RGD) or (MMPs) sequence to explore the contribution of ECM on morphogenesis (Trubuil et al., 2021, Indana et al., 2021). Taking this together, the access of HipSci lines with the hydrogels system in this project can be extended to overcome the phenotypic outliers aiming to induce differentiation propensity (Vickers et al., 2021).

6.1.2 Limitations

This work focussed on investigating the contribution of biochemical cues and physical confinement separately influence morphogenesis and three germ layers specification in 3D hiPSC-derived models of gastrulation. The hiPSC cell line used to develop this platform was obtained from the HipSci cell biobank of a healthy donor (Hoik_1). This helps minimise excessive optimisation, including technical troubleshooting during experiments to build up the readouts. The hiPSC cell lines may exhibit variations in pluripotency such as genetic or non-genetic factors such as cell-adhesion related which impact the differentiation of the three germ layers (Vigilante et al., 2019, Vickers et al., 2021).

Testing other HipSci cell lines from healthy donors is preferable to validate the observed phenotype and differentiation capacity under diverse medium conditions. However, the inaccessibility of the JuliStage live imaging microscopy due to device technical issues during the COVID pandemic was a major limitation to screening more cell lines. I performed a validation assessment using cell lines (eojr_2 and Yuze_1) from healthy donors to explore whether axial elongation is restricted to Hoik_1 cell line. I used confocal microscopy to capture changes in morphology after 96 hours (live imaging is not available for this cell line). The eojr_2 line did not form a proper spheroid resulting in failure to maintain spheroid expansion in E8, form axial elongation in KSR BMP4 and not able to form both intermediate phenotypes when cultured in E8 BMP4 and KSR. This could be related to hiPSC colonies quality during routine 2D culture, which has a massive amount of detached single cells affecting aggregation. In the Yuze_1 line, the cells showed reproducible phenotypes similar to the Hoik_1, confirming that the observed

readouts of morphological changes were not restricted to one cell line. In this assessment, SOX17 and OCT4 immunostaining was performed on spheroids in KSR BMP4, OCT4 was downregulated, and polarisation of the SOX17 marker was detected (Appendix 2). This assay was a quick assessment for validation; however, it is not sufficient; it would be valuable to stain for (BRA, EOMES, and SOX2) markers. However, a recent study in the group using the 2D micropattern system revealed that the Yuze-1 cell line is a phenotypic outlier for SOX2 and BRA expression, which is not investigated in this differentiation assays (Vickers et al., 2021). In addition, morphological changes between the technical and biological replicates generate variations when forming spheroids or elongation (double or multiple budding) (Baillie-Benson et al., 2020). For exploring more cell lines, further titration, including cell seeding densities is required to obtain standardised spheroids formation or proper elongation (Moris et al., 2020, Baillie-Benson et al., 2020).

Investigating the emergence of lineage specification of the three germ layers was built on the expression SOX2 (ectoderm-like), BRA and EOMES (mesoderm), and SOX17 (endoderm); and (OCT4) for pluripotency. Some limitations are associated with the immunostaining technique and the selection of the differentiation markers, firstly SOX2 is a critical marker that can indicate pluripotent cells; secondly, SOX17 for the endodermal marker is not sufficient more markers need to be tested to validate lineage identity, such as NESTIN and SOX1 for ectoderm, and FOXA2 or GATA6. Another limitation of this study is that I perform the immunostaining using OCT4 and one differentiation marker for each 3D spheroid due to the same source of antibody species. It will be ideal to show all three germ layers together for example, in KSR BMP4 to demonstrate the organised pattern. For example, FOXA2 expression would confirm whether SOX17 positive cells are an endoderm population (Hashmi et al., 2021). In contrast, NANOG, and BLMP1 expression would distinguish the PGCs population (Niakan et al., 2010), and CDX2 would validate if the posterior side of the elongated 3D spheroid expresses a trophectoderm (Warmflash et al., 2014, Morris et al., 2012). After BMP4 stimulation, exploring SMAD activity on the elongated spheroid would help to give some insight into the BMP4 dynamic signal gradient and to validate the distinction between the anterior and posterior sides.

The hydrogel approach carries limitations in terms of addressing cell extrinsic signals; when spheroids were encapsulated in different hydrogel systems (non-degPEG vs. deg-PEG), the initial stiffness varies between the two systems. Ideally, to compare the impact of degradability on spheroid morphology and lineage specification in these hydrogel systems, the initial stiffness of non-degPEG and deg-PEG should be considered. This can be improved by increasing the polymer concentration when forming deg-PEG hydrogel and insure that measured mechanical properties correspond with deg-PEG hydrogel. In addition, hydrogel degradability was mainly investigated on non-degPEG formed at 2.5% polymer concentration, whereas 5% polymer concentration was only used in non-deg-PEG. This should be explored to identify whether 5% deg-PEG would increase the degradability of the stiff gel and questions whether this impacts cell viability.

Multiple obstacles are associated with confocal imaging of 3D spheroids in suspension or encapsulated in the hydrogel. The clarity of the images in the core of spheroids was a major issue which can be improved using clearing methods after staining. When imaging the encapsulated spheroids, it could be out of the range of the Z-stack due to the spheroid's position resulting in poor imaging that showed a cavity-like formation that doesn't exist when compared to control or other images. A possible solution would be using super-resolution microscopy, such as light sheet microscopy or spinning disk confocal images. In addition, 3D image analysis is challenging, which could prevent us from obtaining readouts on specific staining. In this thesis, quantification of YAP nuclear/cytoplasmic localisation was not included due to the difficulties in segmenting the nucleus and quantifying YAP expression, especially between the Z-stacks.

6.2 *Future Directions*

6.2.1 Genetic variation of hiPSC

Based on the previous work of HipSci project large panel of hiPSC was characterised from healthy donors and individuals with genetic variants analysed for morphology, proliferation, and cell adhesion (Leha et al., 2016, Vigilante et al., 2019, Kilpinen et al., 2017). In this thesis, individual cell lines (Hoik_1) from HipSci were selected for culture and characterised using both live imaging and confocal techniques to capture morphogenesis and the emergence of lineage specifications. Other cell lines (eojr_2 and Yuze_1) were only used for rapid validation to ensure the consistency of morphology. Further screening of hiPSC lines known for genetic variants would help to identify phenotypic outliers associated with ECM-cell interaction or cell adhesion in this 3D model. Focussing on the main conditions of E8 medium to quantify cell line pluripotency capacity and KSR BMP4 medium to determine germ layers differentiation derived from different cell lines might reveal additional phenotypic variations.

The outcome of these experiments will provide morphological observations data set to be characterised using the frame-to-frame pipeline and quantify spheroid behaviour. Then, these readouts can be used to link potential axial elongation variations with differentiation markers expression in each cell line. These cell lines with genetic variations might have a low ability to initially form spheroid that impacts elongation and differentiation, which was observed during eojr_2 (normal cell line). In a recent study, the cell line eojr_2 was selected as a control in a micropattern-based system which showed normal pattern formation of the three germ layers (Vickers et al., 2021) except when this was cultured in 3D cells failed to aggregate and differentiate. This could be investigated by increasing the cell seeding density or immunofluorescence labelling of cell-adhesion markers. It would be worth exploring the pluripotency and differentiation propensities in a large panel of HipSci lines and mapping the phenotypic outliers compared to the 2D model. This might detect unexpected genetic variants that influence changes in morphology and thus predict differentiation efficacy.

This approach provides a valuable platform to benchmark hiPSC from patients with genetic abnormalities into transitional applications such as CRISPR-based technology to

improve disease modelling and drug screening, not essentially for genes related to gastrulation.

6.2.2 Time-course of germ layer differentiation

Tissue rearrangements and lineage specification of three germ layers during early development happen following signalling dynamic wave within a time scale (Camacho-Aguilar and Warmflash, 2020, Chhabra et al., 2019, Niakan et al., 2012). The cellular movement is initiated when the primitive streak forms; these cells undergo EMT to give rise to the mesoderm and endoderm lineages (Muncie et al., 2020, Hashmi et al., 2021). It has been demonstrated that SOX17 expressed initially within the epiblast co-expressed with OCT4 marker (Niakan et al., 2010). The ability of the BMP4 signal to stimulate most of the existing pluripotency within 30 minutes pulse of BMP4 exposure, therefore, induce changes in cell morphology and differentiation was reported in the 2D micropattern model (Gunne-Braden et al., 2020).

Investigating the emergence of the tri-lineage fates over time-course immunostaining allows us to gain insight into the onset expression and patterning process (Camacho-Aguilar and Warmflash, 2020, Moris et al., 2020). In cells cultured KSR BMP4, the immunostaining of the three germ layers revealed SOX17 OCT4 co-expression in the neck of the spheroid, whereas in the elongated tip, only SOX17 was expressed, and BRA marker was found in low levels. The time-course immunostaining post BMP4 induction in time points (0,12,24,48 hours) additional to 96 hours for BRA and SOX17 can demonstrate the origin distribution of marker expression. BRA marker could be expressed from the onset of BMP4 treatment and might be detected at high levels or in a different region of the 3D model. In a recent study, the expression of the BRA marker polarised and was seen within the first 24 hours, and by 96 hours, BRA overlapped with SOX2 marker (Moris et al., 2020). Tracking the expression of SOX17 marker during time-course would help to explore how OCT4 and SOX17 coordinate. Several questions will be answered, including whether SOX17 is initially stimulated during the early time point of BMP4 treatment if OCT4 is required to drive differentiation, and if SOX17 OCT4 together triggers axial elongation. The lineage-tracing approach could reveal the causative link of shape changes and patterning of germ layers in this proposed 3D

gastrulation model. Fluorescent reporter cell lines would be a valuable option to visualise and track cells when they exist pluripotency, the A-P domains and differentiation markers expression.

6.2.3 Transcriptomics characterisation

Transcriptomics of a 3D gastrulation-like model derived from hESC treated with CHIRON displayed reproducible pattern gene expression that notably matches the organisation of those in the human embryo (Moris et al., 2020, van den Brink et al., 2020). Genetics characterisation for 3D gastrulation by single-cell RNA sequencing (scRNA sequencing) and genome-wide RNA Tomography (tomo-seq) identified multiple lineages and gene expressions that were not reported before (Junker et al., 2014, Moris et al., 2020, van den Brink et al., 2020). On the single-cell level, RNA-seq showed expression of relative markers for ectoderm, endoderm, mesoderm and primordial germ cells. In contrast, tomo-seq revealed detailed data on pattern gene expression of anterior-posterior domains, somites and tailbud mirroring the *in vivo* embryo (van den Brink et al., 2020, Moris et al., 2020).

In this thesis, our understanding of the hiPSC 3D model after BMP4 induction or KSR medium is largely based on imaging for differentiation markers. Exploiting transcriptomics characterisation would provide greater insight into the identity of spheroids under distinct medium conditions. In the KSR BMP4 condition, transcriptomics analysis of Sc-RNA-seq would provide insight into the cell identity and distinguish between cell population that co-express OCT4/SOX17 markers or express SOX17 only. Investigating this in control conditions E8 BMP4 and KSR in parallel with KSR BMP4 would help to determine the contribution of biochemical cues in cell fate decisions. In comparison to the previously described hESC 3D gastrulation model (Moris et al., 2020, van den Brink et al., 2020) and *in vivo*, this analysis would also help to explore how similar the lineages expression to our proposed hiPSC 3D BMP4-dependent model.

Furthermore, tomo-seq is another transcriptomic method that can be used to map gene expression organisation in this 3D model along the A-P axis. In this technique, gastruloids were sectioned, followed by mRNA extraction which then used for RNA sequencing (Moris et al., 2020). Lineages differentiation in spheroids cultured in KSR BMP4 are

expressed in the assumed anterior domain, whereas in the assumed posterior, OCT4 expression was lost; this analysis would help to determine the cell identity based on the genetic expression. The generated readouts could demonstrate the ability of BMP4-treated hiPSC to produce reproducible gene pattern expression compared to hESC model and then the normal human embryo. Also, this might reveal differential gene expression in the hiPSC model to hESC.

Transcriptomics characterisation is a powerful tool to identify the gene expression, which enables to validate the lineages specifications observed in our 3D model. HipSci lines in undifferentiated or differentiation conditions and transcriptomics would allow for mapping gene expression of gastrulation and determining the association of genetic variation in hiPSC on the pluripotency and differentiation propensities.

6.2.4 PEG-peptide hydrogel modification

The mechanical properties of the microenvironment generate biophysical cues which integrate with the morphogen stimuli influencing the cell fate decisions (Indana et al., 2021, Vianello and Lutolf, 2019, Walters and Gentleman, 2015). *In vivo*, the mechanical transition of the uterine environment regulates lumen formation during blastocyst and shape deformation during axis formation leading to germ layers differentiation (Vianello and Lutolf, 2019, Gupta et al., 2021). Our understanding of how modification in mechanical properties and the exerted forces control differentiation in the early embryo is limited (Indana et al., 2021, Vianello and Lutolf, 2019, Vining and Mooney, 2017).

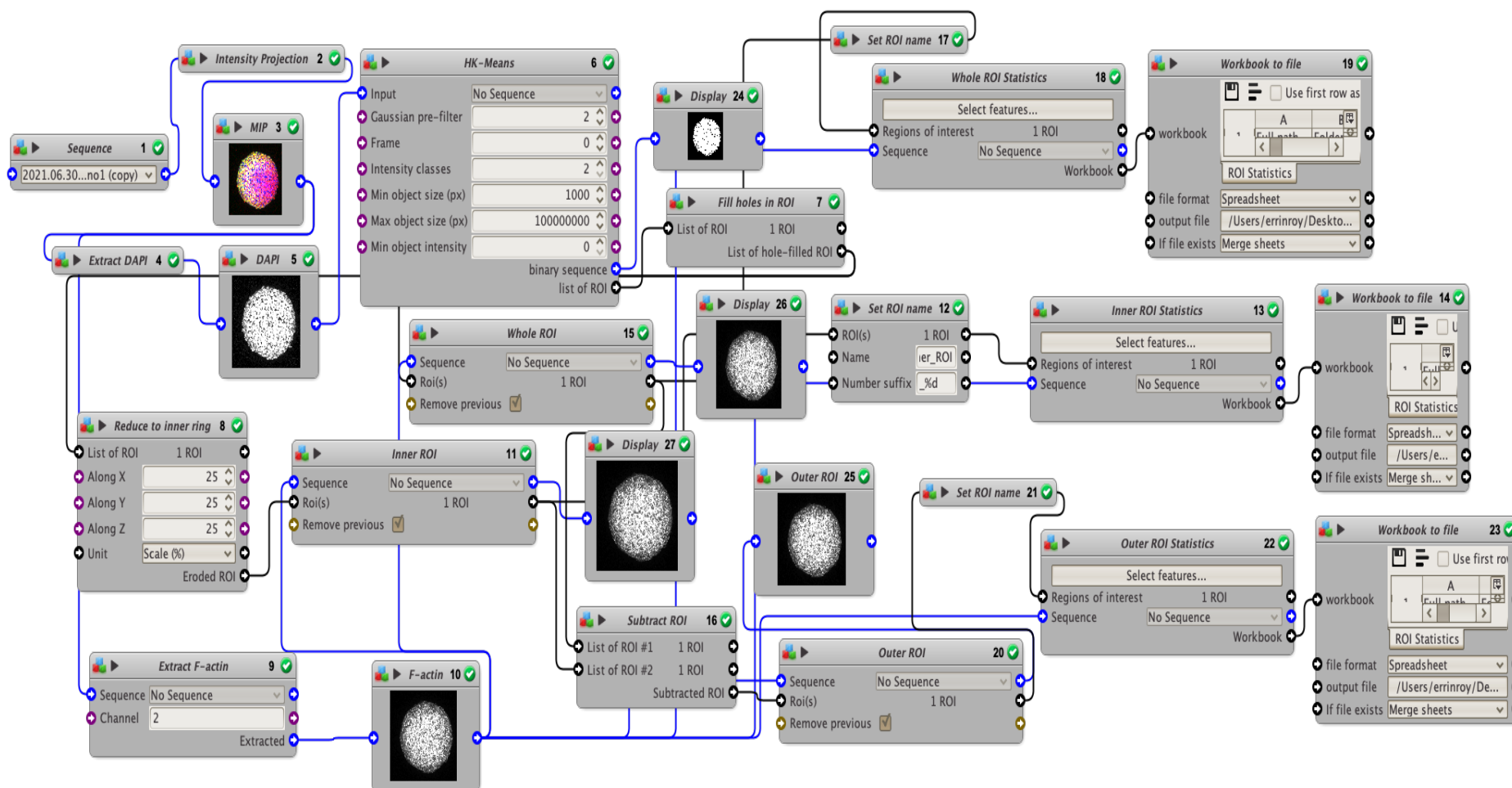
In this project, the effect of physical confinement by tuning PEG-peptide hydrogels stiffness and degradability determines that elongation which is presumably essential to obtain the proper formation of the three germ layers. However, ECM-cell interactions are also important in driving morphogenesis and cell fate which is not investigated in this thesis (Gjorevski et al., 2016, Ranga et al., 2014). This has been widely studied in intestinal organoids (Jowett et al., 2021) and neural tube models (Ranga et al., 2016). In our described hiPSC-derived 3D model of gastrulation would be interesting to explore this, which allows for in-depth quantitative across the hiPSC lines that could determine ECM-cell interactions and differentiation potential.

Embedded in determined stiffness (2.5%) of deg-PEG hydrogel (75% PEG-4Acr exhibited better cell viability) and notably stimulated SOX17 expression compared to non-degPEG (PEG-4VS). This platform can be further improved to establish a better system incorporating the adhesive (RGD) degradable (MMPs) motifs, for instance, which allows exploring the ECM-cell impact on morphogenesis and lineage specification. A recent study reported that fast relaxing alginate hydrogel with high RGD concentration promotes viability and lumen formation, which is required in the neural tube and intestinal organoid (Indana et al., 2021). In contrast, MMPs activity regulates basement membrane remodelling in mouse ESCs allowing for spheroids growth and elongation (Kyprianou et al., 2020). For example, using deg-PEG hydrogel for its ability to promote cell viability, further experiments by altering its properties, such as RGD or MMPs sequence, might allow for spheroid growth or ECM remodelling. Physically confined spheroids in (non-functional peptide) hydrogel could be missing their own ECM biological motifs, allowing ECM-cell interaction and promoting changes in the shape (Foyt et al., 2018). This is an interesting approach that offers to gain insight into the role of the ECM-cell interaction on morphogenesis and then differentiation. Another possible approach is photosensitive hydrogels, where the crosslinking sites cleaved upon light resulting in softening hydrogel in photolabile areas (Spiteri et al., 2020). This system allows controlling the hydrogel's physical properties to regulate the formation of the germ layers differentiation; as an example, soft gel induces SOX2 and SOX17, whereas stiff hydrogel favoured BRA expression (Spiteri et al., 2020, Muncie et al., 2020, Rasmussen et al., 2016).

Modulating PEG-peptide hydrogel properties enables dissecting the role of physical cues directing morphogenesis and germ layers differentiation. Exploring these proposed experiments across hiPSC lines known for phenotypic outliers may help rescue specific germ layers. Because cell fate decisions are regulated by physical and biochemical cues of the surrounding microenvironment, this could promote differentiation to improve various hiPSC-derived organoids (gut, pancreas, or brain) development (Turner et al., 2016).

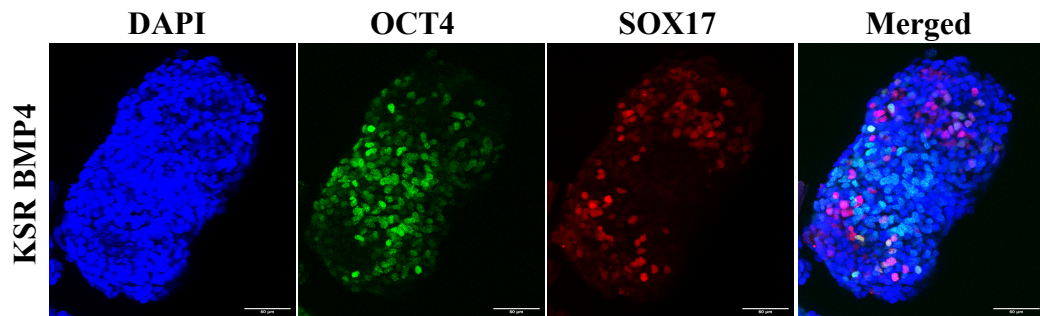
APPENDIX 1

The Icy pipeline used for F-actin analysis.



APPENDIX 2

Yuze_1 cell line stain for OCT4 and SOX17 after culture in KSR BMP4 medium formed an axial elongation and exhibited SOX17 expression.



REFERENCE LIST

- AASEN, T., RAYA, A., BARRERO, M. J., GARRETA, E., CONSIGLIO, A., GONZALEZ, F., et al. 2008. Efficient and rapid generation of induced pluripotent stem cells from human keratinocytes. *Nature biotechnology*, 2611, 1276-1284. doi.org/10.1038/nbt.1503
- ALSEHLI, H., MOSIS, F., THOMPSON, C., HAMRUD, E., WISEMAN, E., GENTLEMAN, E., et al. 2021. An integrated pipeline for high-throughput screening and profiling of spheroids using simple live image analysis of frame to frame variations. *Methods*, 19033-43. doi.org/10.1016/j.ymeth.2020.05.017
- ARIAS, A. M., MARIKAWA, Y. & MORIS, N. 2022. Gastruloids: Pluripotent stem cell models of mammalian gastrulation and embryo engineering. *Dev Biol*, 48835-46. doi.org/10.1016/j.ydbio.2022.05.002
- ARNOLD, S. J. & ROBERTSON, E. J. 2009. Making a commitment: cell lineage allocation and axis patterning in the early mouse embryo. *Nat Rev Mol Cell Biol*, 102, 91-103. doi.org/10.1038/nrm2618
- BAILLIE-BENSON, P., MORIS, N. & MARTINEZ ARIAS, A. 2020. Pluripotent stem cell models of early mammalian development. *Current Opinion in Cell Biology*, 6689-96. doi.org/10.1016/j.ceb.2020.05.010
- BAO, M., CORNWALL-SCOONES, J. & ZERNICKA-GOETZ, M. 2022. Stem-cell-based human and mouse embryo models. *Current Opinion in Genetics & Development*, 76101970. doi.org/10.1016/j.gde.2022.101970
- BARRY, J., HYLLNER, J., STACEY, G., TAYLOR, C. J. & TURNER, M. 2015. Setting Up a Haplobank: Issues and Solutions. *Current Stem Cell Reports*, 12, 110-117. doi.org/10.1007/s40778-015-0011-7
- BATEMAN, J. F., BOOT-HANDFORD, R. P. & LAMANDÉ, S. R. 2009. Genetic diseases of connective tissues: cellular and extracellular effects of ECM mutations. *Nat Rev Genet*, 103, 173-183. doi.org/10.1038/nrg2520
- BAUWENS, C. L., PEERANI, R., NIEBRUEGGE, S., WOODHOUSE, K. A., KUMACHEVA, E., HUSAIN, M., et al. 2008. Control of human embryonic stem cell colony and aggregate size heterogeneity influences differentiation trajectories. *Stem Cells*, 269, 2300-2310. doi.org/10.1634/stemcells.2008-0183
- BECCARI, L., MORIS, N., GIRGIN, M., TURNER, D. A., BAILLIE-JOHNSON, P., COSSY, A.-C., et al. 2018. Multi-axial self-organization properties of mouse embryonic stem cells into gastruloids. *Nature*, 5627726, 272-276. doi.org/10.1038/s41586-018-0578-0

- BEDZHOV, I. & ZERNICKA-GOETZ, M. 2014. Self-Organizing Properties of Mouse Pluripotent Cells Initiate Morphogenesis upon Implantation. *Cell*, 1565, 1032-1044. doi.org/10.1016/j.cell.2014.01.023
- BEN-HAIM, N., LU, C., GUZMAN-AYALA, M., PESCATORE, L., MESNARD, D., BISCHOFBERGER, M., et al. 2006a. The nodal precursor acting via activin receptors induces mesoderm by maintaining a source of its convertases and BMP4. *Dev Cell*, 113, 313-323. doi.org/10.1016/j.devcel.2006.07.005
- BEN-HAIM, N., LU, C., GUZMAN-AYALA, M., PESCATORE, L., MESNARD, D., BISCHOFBERGER, M., et al. 2006b. The Nodal Precursor Acting via Activin Receptors Induces Mesoderm by Maintaining a Source of Its Convertases and BMP4. *Developmental Cell*, 113, 313-323. doi.org/10.1016/j.devcel.2006.07.005
- BLACHE, U., FORD, E. M., HA, B., RIJNS, L., CHAUDHURI, O., DANKERS, P. Y. W., et al. 2022. Engineered hydrogels for mechanobiology. *Nature Reviews Methods Primers*, 21, 98. doi.org/10.1038/s43586-022-00179-7
- BOCK, C., KISKINIS, E., VERSTAPPEN, G., GU, H., BOULTING, G., SMITH, Z. D., et al. 2011. Reference Maps of human ES and iPS cell variation enable high-throughput characterization of pluripotent cell lines. *Cell*, 1443, 439-452. doi.org/10.1016/j.cell.2010.12.032
- BRIGHT, J., HUSSAIN, S., DANG, V., WRIGHT, S., COOPER, B., BYUN, T., et al. 2015. Human secreted tau increases amyloid-beta production. *Neurobiol Aging*, 362, 693-709. doi.org/10.1016/j.neurobiolaging.2014.09.007
- CAI, X., WANG, K.-C. & MENG, Z. 2021. Mechanoregulation of YAP and TAZ in Cellular Homeostasis and Disease Progression. *Frontiers in Cell and Developmental Biology*, 9. doi.org/10.3389/fcell.2021.673599
- CAIAZZO, M., OKAWA, Y., RANGA, A., PIERSIGILLI, A., TABATA, Y. & LUTOLF, M. P. 2016. Defined three-dimensional microenvironments boost induction of pluripotency. *Nature Materials*, 153, 344-352. doi.org/10.1038/nmat4536
- CAMACHO-AGUILAR, E. & WARMFLASH, A. 2020. Insights into mammalian morphogen dynamics from embryonic stem cell systems. *Curr Top Dev Biol*, 137279-305. doi.org/10.1016/bs.ctdb.2019.11.010
- CARPENTER, A. E., JONES, T. R., LAMPRECHT, M. R., CLARKE, C., KANG, I. H., FRIMAN, O., et al. 2006. CellProfiler: image analysis software for identifying and quantifying cell phenotypes. *Genome Biology*, 710, R100. doi.org/10.1186/gb-2006-7-10-r100
- CARRAGHER, N., PICCININI, F., TESEI, A., JR, O. J. T., BICKLE, M. & HORVATH, P. 2018. Concerns, challenges and promises of high-content analysis of 3D cellular models. *Nature Reviews Drug Discovery*, 178, 606-606. doi.org/10.1038/nrd.2018.99

- CHAPMAN, S. C., COLLIGNON, J., SCHOENWOLF, G. C. & LUMSDEN, A. 2001. Improved method for chick whole-embryo culture using a filter paper carrier. *Dev Dyn*, 2203, 284-289. doi.org/10.1002/1097-0177(20010301)220:3<284::Aid-dvdy1102>3.0.Co;2-5
- CHEN, G., GULBRANSON, D. R., HOU, Z., BOLIN, J. M., RUOTTI, V., PROBASCO, M. D., et al. 2011. Chemically defined conditions for human iPSC derivation and culture. *Nature Methods*, 85, 424-429. doi.org/10.1038/nmeth.1593
- CHENG, P., ANDERSEN, P., HASSEL, D., KAYNAK, B. L., LIMPHONG, P., JUERGENSEN, L., et al. 2013. Fibronectin mediates mesendodermal cell fate decisions. *Development*, 14012, 2587-2596. doi.org/10.1242/dev.089052
- CHHABRA, S., LIU, L., GOH, R., KONG, X. & WARMFLASH, A. 2019. Dissecting the dynamics of signaling events in the BMP, WNT, and NODAL cascade during self-organized fate patterning in human gastruloids. *PLOS Biology*, 1710, e3000498. doi.org/10.1371/journal.pbio.3000498
- CHIN, M. H., MASON, M. J., XIE, W., VOLINIA, S., SINGER, M., PETERSON, C., et al. 2009. Induced pluripotent stem cells and embryonic stem cells are distinguished by gene expression signatures. *Cell Stem Cell*, 51, 111-123. doi.org/10.1016/j.stem.2009.06.008
- CLARKE, D. N. & MARTIN, A. C. 2021. Actin-based force generation and cell adhesion in tissue morphogenesis. *Current Biology*, 3110, R667-R680. doi.org/10.1016/j.cub.2021.03.031
- CLEVERS, H. 2016. Modeling Development and Disease with Organoids. *Cell*, 1657, 1586-1597. doi.org/10.1016/j.cell.2016.05.082
- COX, T. R. & ERLER, J. T. 2011. Remodeling and homeostasis of the extracellular matrix: implications for fibrotic diseases and cancer. *Dis Model Mech*, 42, 165-178. doi.org/10.1242/dmm.004077
- CRUZ-ACUÑA, R., QUIRÓS, M., FARKAS, A. E., DEDHIA, P. H., HUANG, S., SIUDA, D., et al. 2017. Synthetic hydrogels for human intestinal organoid generation and colonic wound repair. *Nat Cell Biol*, 1911, 1326-1335. doi.org/10.1038/ncb3632
- CSOBONYEIOVA, M., POLAK, S., KOLLER, J. & DANISOVIC, L. 2015. Induced pluripotent stem cells and their implication for regenerative medicine. *Cell and Tissue Banking*, 162, 171-180. doi.org/10.1007/s10561-014-9462-9
- D'ARCANGELO, E. & MCGUIGAN, A. P. 2015. Micropatterning strategies to engineer controlled cell and tissue architecture in vitro. *BioTechniques*, 581, 13-23. doi.org/10.2144/000114245
- DANOVI, D., FOLARIN, A., GOGOLOK, S., ENDER, C., ELBATSH, A. M. O., ENGSTRÖM, P. G., et al. 2013. A High-Content Small Molecule Screen

- Identifies Sensitivity of Glioblastoma Stem Cells to Inhibition of Polo-Like Kinase 1. *PLOS ONE*, 810, e77053. doi.org/10.1371/journal.pone.0077053
- DE CHAUMONT, F., DALLONGEVILLE, S., CHENOUEARD, N., HERVÉ, N., POP, S., PROVOOST, T., et al. 2012. Icy: an open bioimage informatics platform for extended reproducible research. *Nature Methods*, 97, 690-696. doi.org/10.1038/nmeth.2075
- DEGLINCERTI, A., ETOC, F., GUERRA, M. C., MARTYN, I., METZGER, J., RUZO, A., et al. 2016. Self-organization of human embryonic stem cells on micropatterns. *Nat Protoc*, 1111, 2223-2232. doi.org/10.1038/nprot.2016.131
- DENG, J., SHOEMAKER, R., XIE, B., GORE, A., LEPROUST, E. M., ANTOSIEWICZ-BOURGET, J., et al. 2009. Targeted bisulfite sequencing reveals changes in DNA methylation associated with nuclear reprogramming. *Nat Biotechnol*, 274, 353-360. doi.org/10.1038/nbt.1530
- DYE, B. R., HILL, D. R., FERGUSON, M. A. H., TSAI, Y.-H., NAGY, M. S., DYAL, R., et al. 2015. In vitro generation of human pluripotent stem cell derived lung organoids. *eLife*, 4e05098. doi.org/10.7554/eLife.05098
- EBERT, A. D., YU, J., ROSE, F. F., JR., MATTIS, V. B., LORSON, C. L., THOMSON, J. A., et al. 2009. Induced pluripotent stem cells from a spinal muscular atrophy patient. *Nature*, 4577227, 277-280. doi.org/10.1038/nature07677
- EHRBAR, M., RIZZI, S. C., SCHOENMAKERS, R. G., SAN MIGUEL, B., HUBBELL, J. A., WEBER, F. E., et al. 2007. Biomolecular Hydrogels Formed and Degraded via Site-Specific Enzymatic Reactions. *Biomacromolecules*, 810, 3000-3007. doi.org/10.1021/bm070228f
- FANG, F., LI, Z., ZHAO, Q., XIONG, C. & NI, K. 2020. Analysis of multi-lineage gene expression dynamics during primordial germ cell induction from human induced pluripotent stem cells. *Stem Cell Research & Therapy*, 111, 100. doi.org/10.1186/s13287-020-01620-y
- FOYT, D. A., NORMAN, M. D. A., YU, T. T. L. & GENTLEMAN, E. 2018. Exploiting Advanced Hydrogel Technologies to Address Key Challenges in Regenerative Medicine. *Adv Healthc Mater*, 78, e1700939. doi.org/10.1002/adhm.201700939
- FULTON, T., TRIVEDI, V., ATTARDI, A., ANLAS, K., DINGARE, C., ARIAS, A. M., et al. 2020. Axis Specification in Zebrafish Is Robust to Cell Mixing and Reveals a Regulation of Pattern Formation by Morphogenesis. *Current Biology*, 3015, 2984-2994.e2983. doi.org/10.1016/j.cub.2020.05.048
- FUSAKI, N., BAN, H., NISHIYAMA, A., SAEKI, K. & HASEGAWA, M. 2009. Efficient induction of transgene-free human pluripotent stem cells using a vector based on Sendai virus, an RNA virus that does not integrate into the host genome. *Proc Jpn Acad Ser B Phys Biol Sci*, 858, 348-362. doi.org/10.2183/pjab.85.348

- GAO, X., CUI, X., ZHANG, X., ZHAO, C., ZHANG, N., ZHAO, Y., et al. 2020. Differential genetic mutations of ectoderm, mesoderm, and endoderm-derived tumors in TCGA database. *Cancer Cell International*, 201, 595. doi.org/10.1186/s12935-020-01678-x
- GJOREVSKI, N. & LUTOLF, M. P. 2017. Synthesis and characterization of well-defined hydrogel matrices and their application to intestinal stem cell and organoid culture. *Nat Protoc*, 1211, 2263-2274. doi.org/10.1038/nprot.2017.095
- GJOREVSKI, N., NIKOLAEV, M., BROWN, T. E., MITROFANOVA, O., BRANDENBERG, N., DELRIO, F. W., et al. 2022. Tissue geometry drives deterministic organoid patterning. *Science*, 3756576, eaaw9021. doi.org/doi:10.1126/science.aaw9021
- GJOREVSKI, N., SACHS, N., MANFRIN, A., GIGER, S., BRAGINA, M. E., ORDÓÑEZ-MORÁN, P., et al. 2016. Designer matrices for intestinal stem cell and organoid culture. *Nature*, 5397630, 560-564. doi.org/10.1038/nature20168
- GONZÁLEZ, F., BOUÉ, S. & BELMONTE, J. C. I. 2011. Methods for making induced pluripotent stem cells: reprogramming à la carte. *Nature Reviews Genetics*, 124, 231-242. doi.org/10.1038/nrg2937
- GREEN, J. 2002. Morphogen gradients, positional information, and Xenopus: Interplay of theory and experiment. *Developmental Dynamics*, 2254, 392-408. doi.org/doi.org/10.1002/dvdy.10170
- GREEN, J. B. & SHARPE, J. 2015. Positional information and reaction-diffusion: two big ideas in developmental biology combine. *Development*, 1427, 1203-1211. doi.org/10.1242/dev.114991
- GREEN, J. B. A. & SMITH, J. C. 1991. Growth factors as morphogens: do gradients and thresholds establish body plan? *Trends in Genetics*, 78, 245-250. doi.org/doi.org/10.1016/0168-9525(91)90323-I
- GRSKOVIC, M., JAVAHERIAN, A., STRULOVICI, B. & DALEY, G. Q. 2011. Induced pluripotent stem cells — opportunities for disease modelling and drug discovery. *Nature Reviews Drug Discovery*, 1012, 915-929. doi.org/10.1038/nrd3577
- GUENTHER, M. G., FRAMPTON, G. M., SOLDNER, F., HOCKEMEYER, D., MITALIPOVA, M., JAENISCH, R., et al. 2010. Chromatin structure and gene expression programs of human embryonic and induced pluripotent stem cells. *Cell Stem Cell*, 72, 249-257. doi.org/10.1016/j.stem.2010.06.015
- GUNNE-BRADEN, A., SULLIVAN, A., GHARIBI, B., SHERIFF, R. S. M., MAITY, A., WANG, Y.-F., et al. 2020. GATA3 Mediates a Fast, Irreversible Commitment to BMP4-Driven Differentiation in Human Embryonic Stem Cells. *Cell Stem Cell*, 265, 693-706.e699. doi.org/10.1016/j.stem.2020.03.005

- GUPTA, A., LUTOLF, M. P., HUGHES, A. J. & SONNEN, K. F. 2021. Bioengineering in vitro models of embryonic development. *Stem Cell Reports*, 165, 1104-1116. doi.org/10.1016/j.stemcr.2021.04.005
- GUVENDIREN, M. & BURDICK, J. A. 2013. Engineering synthetic hydrogel microenvironments to instruct stem cells. *Current Opinion in Biotechnology*, 245, 841-846. doi.org/10.1016/j.copbio.2013.03.009
- HALDER, G., DUPONT, S. & PICCOLO, S. 2012. Transduction of mechanical and cytoskeletal cues by YAP and TAZ. *Nature Reviews Molecular Cell Biology*, 139, 591-600. doi.org/10.1038/nrm3416
- HALE, L. J., HOWDEN, S. E., PHIPSON, B., LONSDALE, A., ER, P. X., GHOBRIAL, I., et al. 2018. 3D organoid-derived human glomeruli for personalised podocyte disease modelling and drug screening. *Nature Communications*, 91, 5167. doi.org/10.1038/s41467-018-07594-z
- HANATANI, T. & TAKASU, N. 2020. CiRA iPSC seed stocks (CiRA's iPSC Stock Project). *Stem Cell Res*, 50102033. doi.org/10.1016/j.scr.2020.102033
- HANNA, J., WERNIG, M., MARKOULAKI, S., SUN, C.-W., MEISSNER, A., CASSADY, J. P., et al. 2007. Treatment of Sickle Cell Anemia Mouse Model with iPS Cells Generated from Autologous Skin. *Science*, 3185858, 1920-1923. doi.org/doi:10.1126/science.1152092
- HARRIS, K., AYLOTT, M., CUI, Y., LOUTTIT, J. B., MCMAHON, N. C. & SRIDHAR, A. 2013. Comparison of Electrophysiological Data From Human-Induced Pluripotent Stem Cell-Derived Cardiomyocytes to Functional Preclinical Safety Assays. *Toxicological Sciences*, 1342, 412-426. doi.org/10.1093/toxsci/kft113
- HARRISON, S. E., SOZEN, B., CHRISTODOULOU, N., KYPRIANOU, C. & ZERNICKA-GOETZ, M. 2017. Assembly of embryonic and extraembryonic stem cells to mimic embryogenesis in vitro. *Science*, 3566334, eaal1810. doi.org/doi:10.1126/science.aal1810
- HASHMI, A., TLILI, S., PERRIN, P., LOWNDES, M., PERADZIRYI, H., BRICKMAN, J. M., et al. 2022. Cell-state transitions and collective cell movement generate an endoderm-like region in gastruloids. *eLife*, 11e59371. doi.org/10.7554/eLife.59371
- HASHMI, A., TLILI, S., PERRIN, P., MARTINEZ-ARIAS, A. & LENNE, P.-F. 2021. Cell-state transitions and collective cell movement generate an endoderm-like region in gastruloids. *bioRxiv*, 2020.2005.2021.105551. doi.org/10.1101/2020.05.21.105551
- HEEMSKERK, I. & WARMFLASH, A. 2016. Pluripotent stem cells as a model for embryonic patterning: From signaling dynamics to spatial organization in a dish. *Dev Dyn*, 24510, 976-990. doi.org/10.1002/dvdy.24432

- HENG, B. C., ZHANG, X., AUBEL, D., BAI, Y., LI, X., WEI, Y., et al. 2021. An overview of signaling pathways regulating YAP/TAZ activity. *Cellular and Molecular Life Sciences*, 782, 497-512. doi.org/10.1007/s00018-020-03579-8
- HOFER, M. & LUTOLF, M. P. 2021. Engineering organoids. *Nature Reviews Materials*, 65, 402-420. doi.org/10.1038/s41578-021-00279-y
- INDANA, D., AGARWAL, P., BHUTANI, N. & CHAUDHURI, O. 2021. Viscoelasticity and Adhesion Signaling in Biomaterials Control Human Pluripotent Stem Cell Morphogenesis in 3D Culture. *Advanced Materials*, 3343, 2101966. doi.org/10.1002/adma.202101966
- IRIE, N., WEINBERGER, L., TANG, WALFRED W. C., KOBAYASHI, T., VIUKOV, S., MANOR, Y. S., et al. 2015. SOX17 Is a Critical Specifier of Human Primordial Germ Cell Fate. *Cell*, 1601, 253-268. doi.org/10.1016/j.cell.2014.12.013
- JANSEN, K. A., ATHERTON, P. & BALLESTREM, C. 2017. Mechanotransduction at the cell-matrix interface. *Semin Cell Dev Biol*, 7175-83. doi.org/10.1016/j.semcd.2017.07.027
- JOWETT, G. M., NORMAN, M. D. A., YU, T. T. L., ROSELL ARÉVALO, P., HOOGLAND, D., LUST, S. T., et al. 2021. ILC1 drive intestinal epithelial and matrix remodelling. *Nature Materials*, 202, 250-259. doi.org/10.1038/s41563-020-0783-8
- JUNKER, JAN P., NOËL, EMILY S., GURYEV, V., PETERSON, KEVIN A., SHAH, G., HUISKEN, J., et al. 2014. Genome-wide RNA Tomography in the Zebrafish Embryo. *Cell*, 1593, 662-675. doi.org/10.1016/j.cell.2014.09.038
- KAJI, K., NORRBY, K., PACA, A., MILEIKOVSKY, M., MOHSENI, P. & WOLTJEN, K. 2009. Virus-free induction of pluripotency and subsequent excision of reprogramming factors. *Nature*, 4587239, 771-775. doi.org/10.1038/nature07864
- KANG, X., YU, Q., HUANG, Y., SONG, B., CHEN, Y., GAO, X., et al. 2015. Effects of Integrating and Non-Integrating Reprogramming Methods on Copy Number Variation and Genomic Stability of Human Induced Pluripotent Stem Cells. *PLoS One*, 107, e0131128. doi.org/10.1371/journal.pone.0131128
- KAWASE, E. & NAKATSUJI, N. 2023. Development of substrates for the culture of human pluripotent stem cells. *Biomaterials Science*, 119, 2974-2987. doi.org/10.1039/D2BM01473D
- KERZ, M., FOLARIN, A., MELECKYTE, R., WATT, F. M., DOBSON, R. J. & DANОВI, D. 2016. A Novel Automated High-Content Analysis Workflow Capturing Cell Population Dynamics from Induced Pluripotent Stem Cell Live Imaging Data. *SLAS Discovery*, 219, 887-896. doi.org/10.1177/1087057116652064

- KHAN, A. H., COOK, J. K., WORTMANN III, W. J., KERSKER, N. D., RAO, A., POJMAN, J. A., et al. 2020. Synthesis and characterization of thiol-acrylate hydrogels using a base-catalyzed Michael addition for 3D cell culture applications. *Journal of Biomedical Materials Research Part B: Applied Biomaterials*, 1085, 2294-2307. doi.org/10.1002/jbm.b.34565
- KILPINEN, H., GONCALVES, A., LEHA, A., AFZAL, V., ALASOO, K., ASHFORD, S., et al. 2017. Common genetic variation drives molecular heterogeneity in human iPSCs. *Nature*, 5467658, 370-375. doi.org/10.1038/nature22403
- KIM, D. H., XING, T., YANG, Z., DUDEK, R., LU, Q. & CHEN, Y.-H. 2018a. Epithelial Mesenchymal Transition in Embryonic Development, Tissue Repair and Cancer: A Comprehensive Overview. *Journal of Clinical Medicine*, 71, 1. doi.org/10.3390/jcm7010001
- KIM, D. H., XING, T., YANG, Z., DUDEK, R., LU, Q. & CHEN, Y. H. 2017. Epithelial Mesenchymal Transition in Embryonic Development, Tissue Repair and Cancer: A Comprehensive Overview. *J Clin Med*, 71. doi.org/10.3390/jcm7010001
- KIM, E. J. Y., KOROTKEVICH, E. & HIIRAGI, T. 2018b. Coordination of Cell Polarity, Mechanics and Fate in Tissue Self-organization. *Trends Cell Biol*, 287, 541-550. doi.org/10.1016/j.tcb.2018.02.008
- KIM, J., KOO, B.-K. & KNOBLICH, J. A. 2020. Human organoids: model systems for human biology and medicine. *Nature Reviews Molecular Cell Biology*, 2110, 571-584. doi.org/10.1038/s41580-020-0259-3
- KIM, K., ZHAO, R., DOI, A., NG, K., UNTERNAEHRER, J., CAHAN, P., et al. 2011. Donor cell type can influence the epigenome and differentiation potential of human induced pluripotent stem cells. *Nature Biotechnology*, 2912, 1117-1119. doi.org/10.1038/nbt.2052
- KIMBREL, E. A. & LANZA, R. 2020. Next-generation stem cells — ushering in a new era of cell-based therapies. *Nature Reviews Drug Discovery*, 197, 463-479. doi.org/10.1038/s41573-020-0064-x
- KLEINMAN, H. K. & MARTIN, G. R. 2005. Matrigel: basement membrane matrix with biological activity. *Semin Cancer Biol*, 155, 378-386. doi.org/10.1016/j.semcancer.2005.05.004
- KYPRIANOU, C., CHRISTODOULOU, N., HAMILTON, R. S., NAHABOO, W., BOOMGAARD, D. S., AMADEI, G., et al. 2020. Basement membrane remodelling regulates mouse embryogenesis. *Nature*, 5827811, 253-258. doi.org/10.1038/s41586-020-2264-2
- LANCASTER, M. A. & HUCH, M. 2019. Disease modelling in human organoids. *Disease Models & Mechanisms*, 127. doi.org/10.1242/dmm.039347

- LECUIT, T. & LENNE, P. F. 2007. Cell surface mechanics and the control of cell shape, tissue patterns and morphogenesis. *Nat Rev Mol Cell Biol*, 88, 633-644. doi.org/10.1038/nrm2222
- LEHA, A., MOENS, N., MELECKYTE, R., CULLEY, O. J., GERVASIO, M. K., KERZ, M., et al. 2016. A high-content platform to characterise human induced pluripotent stem cell lines. *Methods*, 9685-96. doi.org/10.1016/j.ymeth.2015.11.012
- LEITCH, H. G., TANG, W. W. C. & SURANI, M. A. 2013. Chapter Five - Primordial Germ-Cell Development and Epigenetic Reprogramming in Mammals. *In: HEARD, E. (ed.) Current Topics in Developmental Biology*. Academic Press.
- LENNE, P.-F., MUNRO, E., HEEMSKERK, I., WARMFLASH, A., BOCANEGRA-MORENO, L., KISHI, K., et al. 2021. Roadmap for the multiscale coupling of biochemical and mechanical signals during development. *Physical Biology*, 184, 041501. doi.org/10.1088/1478-3975/abd0db
- LEVENSTEIN, M. E., LUDWIG, T. E., XU, R. H., LLANAS, R. A., VANDENHEUVEL-KRAMER, K., MANNING, D., et al. 2006. Basic fibroblast growth factor support of human embryonic stem cell self-renewal. *Stem Cells*, 243, 568-574. doi.org/10.1634/stemcells.2005-0247
- LIU, L. & WARMFLASH, A. 2021. Self-organized signaling in stem cell models of embryos. *Stem Cell Reports*, 165, 1065-1077. doi.org/10.1016/j.stemcr.2021.03.020
- LÓPEZ-ANGUITA, N., GASSALOGU, S. I., STÖTZEL, M., BOLONDI, A., CONKAR, D., TYPOU, M., et al. 2022. Hypoxia induces an early primitive streak signature, enhancing spontaneous elongation and lineage representation in gastruloids. *Development*, 14920. doi.org/10.1242/dev.200679
- LUST, S. T., HOOGLAND, D., NORMAN, M. D. A., KERINS, C., OMAR, J., JOWETT, G. M., et al. 2021. Selectively Cross-Linked Tetra-PEG Hydrogels Provide Control over Mechanical Strength with Minimal Impact on Diffusivity. *ACS Biomaterials Science & Engineering*, 79, 4293-4304. doi.org/10.1021/acsbiomaterials.0c01723
- LUTOLF, M. & HUBBELL, J. 2005. Synthetic biomaterials as instructive extracellular microenvironments for morphogenesis in tissue engineering. *Nature biotechnology*, 231, 47-55. doi.org/10.1038/nbt1055
- MADL, C. M., LESAVAGE, B. L., DEWI, R. E., LAMPE, K. J. & HEILSHORN, S. C. 2019. Matrix Remodeling Enhances the Differentiation Capacity of Neural Progenitor Cells in 3D Hydrogels. *Advanced Science*, 64, 1801716. doi.org/10.1002/advs.201801716
- MANDAI, M., WATANABE, A., KURIMOTO, Y., HIRAMI, Y., MORINAGA, C., DAIMON, T., et al. 2017. Autologous Induced Stem-Cell-Derived Retinal Cells

- for Macular Degeneration. *New England Journal of Medicine*, 37611, 1038-1046. doi.org/10.1056/NEJMoa1608368
- MARTELLO, G. & SMITH, A. 2014. The Nature of Embryonic Stem Cells. *Annual Review of Cell and Developmental Biology*, 301, 647-675. doi.org/10.1146/annurev-cellbio-100913-013116
- MARTYN, I., KANNO, T. Y., RUZO, A., SIGGIA, E. D. & BRIVANLOU, A. H. 2018. Self-organization of a human organizer by combined Wnt and Nodal signalling. *Nature*, 5587708, 132-135. doi.org/10.1038/s41586-018-0150-y
- MASSEY, A. J. 2015. Multiparametric Cell Cycle Analysis Using the Operetta High-Content Imager and Harmony Software with PhenoLOGIC. *PLOS ONE*, 107, e0134306. doi.org/10.1371/journal.pone.0134306
- MATTIAZZI USAJ, M., STYLES, E. B., VERSTER, A. J., FRIESEN, H., BOONE, C. & ANDREWS, B. J. 2016. High-Content Screening for Quantitative Cell Biology. *Trends Cell Biol*, 268, 598-611. doi.org/10.1016/j.tcb.2016.03.008
- MCCAULEY, H. A. & WELLS, J. M. 2017. Pluripotent stem cell-derived organoids: using principles of developmental biology to grow human tissues in a dish. *Development*, 1446, 958-962. doi.org/10.1242/dev.140731
- MINN, K. T., FU, Y. C., HE, S., DIETMANN, S., GEORGE, S. C., ANASTASIO, M. A., et al. 2020. High-resolution transcriptional and morphogenetic profiling of cells from micropatterned human ESC gastruloid cultures. *eLife*, 9e59445. doi.org/10.7554/eLife.59445
- MOLÈ, M. A., COORENS, T. H. H., SHAHBAZI, M. N., WEBERLING, A., WEATHERBEE, B. A. T., GANTNER, C. W., et al. 2021a. A single cell characterisation of human embryogenesis identifies pluripotency transitions and putative anterior hypoblast centre. *Nature Communications*, 121, 3679. doi.org/10.1038/s41467-021-23758-w
- MOLÈ, M. A., WEBERLING, A., FÄSSLER, R., CAMPBELL, A., FISHEL, S. & ZERNICKA-GOETZ, M. 2021b. Integrin β 1 coordinates survival and morphogenesis of the embryonic lineage upon implantation and pluripotency transition. *Cell Rep*, 3410, 108834. doi.org/10.1016/j.celrep.2021.108834
- MORIS, N., ANLAS, K., VAN DEN BRINK, S. C., ALEMANY, A., SCHRÖDER, J., GHIMIRE, S., et al. 2020. An in vitro model of early anteroposterior organization during human development. *Nature*, 5827812, 410-415. doi.org/10.1038/s41586-020-2383-9
- MORRIS, S. A., GREWAL, S., BARRIOS, F., PATANKAR, S. N., STRAUSS, B., BUTTERY, L., et al. 2012. Dynamics of anterior–posterior axis formation in the developing mouse embryo. *Nature Communications*, 31, 673. doi.org/10.1038/ncomms1671

- MOSSAHEBI-MOHAMMADI, M., QUAN, M., ZHANG, J. S. & LI, X. 2020. FGF Signaling Pathway: A Key Regulator of Stem Cell Pluripotency. *Front Cell Dev Biol*, 879. doi.org/10.3389/fcell.2020.00079
- MUNCIE, J. M., AYAD, N. M. E., LAKINS, J. N., XUE, X., FU, J. & WEAVER, V. M. 2020. Mechanical Tension Promotes Formation of Gastrulation-like Nodes and Patterns Mesoderm Specification in Human Embryonic Stem Cells. *Dev Cell*, 556, 679-694.e611. doi.org/10.1016/j.devcel.2020.10.015
- NAKAYA, Y. & SHENG, G. 2008. Epithelial to mesenchymal transition during gastrulation: An embryological view. *Development, Growth & Differentiation*, 509, 755-766. doi.org/10.1111/j.1440-169X.2008.01070.x
- NAZARETH, E. J. P., OSTBLOM, J. E. E., LÜCKER, P. B., SHUKLA, S., ALVAREZ, M. M., OH, S. K. W., et al. 2013. High-throughput fingerprinting of human pluripotent stem cell fate responses and lineage bias. *Nature Methods*, 1012, 1225-1231. doi.org/10.1038/nmeth.2684
- NEMASHKALO, A., RUZO, A., HEEMSKERK, I. & WARMFLASH, A. 2017. Morphogen and community effects determine cell fates in response to BMP4 signaling in human embryonic stem cells. *Development*, 14417, 3042-3053. doi.org/10.1242/dev.153239
- NEWMAN, A. M. & COOPER, J. B. 2010. Lab-specific gene expression signatures in pluripotent stem cells. *Cell Stem Cell*, 72, 258-262. doi.org/10.1016/j.stem.2010.06.016
- NGUYEN, H. N., BYERS, B., CORD, B., SHCHEGLOVITOV, A., BYRNE, J., GUJAR, P., et al. 2011. LRRK2 mutant iPSC-derived DA neurons demonstrate increased susceptibility to oxidative stress. *Cell Stem Cell*, 83, 267-280. doi.org/10.1016/j.stem.2011.01.013
- NIAKAN, K. K., HAN, J., PEDERSEN, R. A., SIMON, C. & PERA, R. A. R. 2012. Human pre-implantation embryo development. *Development*, 1395, 829-841. doi.org/10.1242/dev.060426
- NIAKAN, K. K., JI, H., MAEHR, R., VOKES, S. A., RODOLFA, K. T., SHERWOOD, R. I., et al. 2010. Sox17 promotes differentiation in mouse embryonic stem cells by directly regulating extraembryonic gene expression and indirectly antagonizing self-renewal. *Genes Dev*, 243, 312-326. doi.org/10.1101/gad.1833510
- NORMAN, M. D. A., FERREIRA, S. A., JOWETT, G. M., BOZEC, L. & GENTLEMAN, E. 2021. Measuring the elastic modulus of soft culture surfaces and three-dimensional hydrogels using atomic force microscopy. *Nat Protoc*, 165, 2418-2449. doi.org/10.1038/s41596-021-00495-4
- OKANO, H. & SIPP, D. 2020. New trends in cellular therapy. *Development*, 14718. doi.org/10.1242/dev.192567

- OKI, S., KITAJIMA, K. & MENO, C. 2010. Dissecting the role of Fgf signaling during gastrulation and left-right axis formation in mouse embryos using chemical inhibitors. *Developmental Dynamics*, 2396, 1768-1778. doi.org/10.1002/dvdy.22282
- OKITA, K., MATSUMURA, Y., SATO, Y., OKADA, A., MORIZANE, A., OKAMOTO, S., et al. 2011. A more efficient method to generate integration-free human iPS cells. *Nature Methods*, 85, 409-412. doi.org/10.1038/nmeth.1591
- PADGETT, J. & SANTOS, S. D. M. 2020. From clocks to dominoes: lessons on cell cycle remodelling from embryonic stem cells. *FEBS Letters*, 59413, 2031-2045. doi.org/10.1002/1873-3468.13862
- PAGLIUCA, F. W., MILLMAN, J. R., GÜRTLER, M., SEGEL, M., VAN DERVORT, A., RYU, J. H., et al. 2014. Generation of functional human pancreatic β cells in vitro. *Cell*, 1592, 428-439. doi.org/10.1016/j.cell.2014.09.040
- PARR, C. J. C., YAMANAKA, S. & SAITO, H. 2017. An update on stem cell biology and engineering for brain development. *Molecular Psychiatry*, 226, 808-819. doi.org/10.1038/mp.2017.66
- PEARL, JEREMY I., LEE, ANDREW S., LEVESON-GOWER, DENNIS B., SUN, N., GHOSH, Z., LAN, F., et al. 2011. Short-Term Immunosuppression Promotes Engraftment of Embryonic and Induced Pluripotent Stem Cells. *Cell Stem Cell*, 83, 309-317. doi.org/<https://doi.org/10.1016/j.stem.2011.01.012>
- PEREA-GOMEZ, A., VELLA, F. D. J., SHAWLOT, W., OULAD-ABDELGHANI, M., CHAZAUD, C., MENO, C., et al. 2002. Nodal Antagonists in the Anterior Visceral Endoderm Prevent the Formation of Multiple Primitive Streaks. *Developmental Cell*, 35, 745-756. doi.org/10.1016/S1534-5807(02)00321-0
- PETZOLD, J. & GENTLEMAN, E. 2021. Intrinsic Mechanical Cues and Their Impact on Stem Cells and Embryogenesis. *Frontiers in cell and developmental biology*, 9761871-761871. doi.org/10.3389/fcell.2021.761871
- PHELPS, E. A., ENEMCHUKWU, N. O., FIORE, V. F., SY, J. C., MURTHY, N., SULCHEK, T. A., et al. 2012. Maleimide cross-linked bioactive PEG hydrogel exhibits improved reaction kinetics and cross-linking for cell encapsulation and in situ delivery. *Adv Mater*, 241, 64-70, 62. doi.org/10.1002/adma.201103574
- PRAKASH BANGALORE, M., ADHIKARLA, S., MUKHERJEE, O. & PANICKER, M. M. 2017. Genotoxic Effects of Culture Media on Human Pluripotent Stem Cells. *Scientific Reports*, 71, 42222. doi.org/10.1038/srep42222
- PROBST, S., SAGAR, TOSIC, J., SCHWAN, C., GRÜN, D. & ARNOLD, S. J. 2021. Spatiotemporal sequence of mesoderm and endoderm lineage segregation during mouse gastrulation. *Development*, 1481. doi.org/10.1242/dev.193789

- RANGA, A., GIRGIN, M., MEINHARDT, A., EBERLE, D., CAIAZZO, M., TANAKA, E. M., et al. 2016. Neural tube morphogenesis in synthetic 3D microenvironments. *Proceedings of the National Academy of Sciences*, 11344, E6831. doi.org/10.1073/pnas.1603529113
- RANGA, A., GOBAA, S., OKAWA, Y., MOSIEWICZ, K., NEGRO, A. & LUTOLF, M. P. 2014. 3D niche microarrays for systems-level analyses of cell fate. *Nature Communications*, 51, 4324. doi.org/10.1038/ncomms5324
- RASMUSSEN, C. H., REYNOLDS, P. M., PETERSEN, D. R., HANSSON, M., MCMEEKING, R. M., DUFVA, M., et al. 2016. Enhanced Differentiation of Human Embryonic Stem Cells Toward Definitive Endoderm on Ultrahigh Aspect Ratio Nanopillars. *Advanced Functional Materials*, 266, 815-823. doi.org/10.1002/adfm.201504204
- RAYON, T., STAMATAKI, D., PEREZ-CARRASCO, R., GARCIA-PEREZ, L., BARRINGTON, C., MELCHIONDA, M., et al. 2020. Species-specific pace of development is associated with differences in protein stability. *Science*, 3696510. doi.org/10.1126/science.aba7667
- REUBINOFF, B. E., PERA, M. F., FONG, C. Y., TROUNSON, A. & BONGSO, A. 2000. Embryonic stem cell lines from human blastocysts: somatic differentiation in vitro. *Nat Biotechnol*, 184, 399-404. doi.org/10.1038/74447
- RIVERA-PÉREZ, J. A. & MAGNUSON, T. 2005. Primitive streak formation in mice is preceded by localized activation of Brachyury and Wnt3. *Dev Biol*, 2882, 363-371. doi.org/10.1016/j.ydbio.2005.09.012
- ROSSANT, J. & TAM, P. P. L. 2022. Early human embryonic development: Blastocyst formation to gastrulation. *Developmental Cell*, 572, 152-165. doi.org/10.1016/j.devcel.2021.12.022
- ROWE, R. G. & DALEY, G. Q. 2019. Induced pluripotent stem cells in disease modelling and drug discovery. *Nature Reviews Genetics*, 207, 377-388. doi.org/10.1038/s41576-019-0100-z
- SAITO-DIAZ, K. & ZELTNER, N. 2019a. Induced pluripotent stem cells for disease modeling, cell therapy and drug discovery in genetic autonomic disorders: a review. *Clinical Autonomic Research*, 294, 367-384. doi.org/10.1007/s10286-018-00587-4
- SAITO-DIAZ, K. & ZELTNER, N. 2019b. Induced pluripotent stem cells for disease modeling, cell therapy and drug discovery in genetic autonomic disorders: a review. *Clin Auton Res*, 294, 367-384. doi.org/10.1007/s10286-018-00587-4
- SAKAI, T., MATSUNAGA, T., YAMAMOTO, Y., ITO, C., YOSHIDA, R., SUZUKI, S., et al. 2008. Design and Fabrication of a High-Strength Hydrogel with Ideally Homogeneous Network Structure from Tetrahedron-like Macromonomers. *Macromolecules*, 4114, 5379-5384. doi.org/10.1021/ma800476x

- SATO, T. & CLEVERS, H. 2013. Growing self-organizing mini-guts from a single intestinal stem cell: mechanism and applications. *Science*, 3406137, 1190-1194. doi.org/10.1126/science.1234852
- SCHLAEGER, T. M., DAHERON, L., BRICKLER, T. R., ENTWISLE, S., CHAN, K., CIANCI, A., et al. 2015. A comparison of non-integrating reprogramming methods. *Nat Biotechnol*, 331, 58-63. doi.org/10.1038/nbt.3070
- SCHWARTZ, M. P., HOU, Z., PROPSON, N. E., ZHANG, J., ENGSTROM, C. J., COSTA, V. S., et al. 2015. Human pluripotent stem cell-derived neural constructs for predicting neural toxicity. *Proceedings of the National Academy of Sciences*, 11240, 12516-12521. doi.org/doi:10.1073/pnas.1516645112
- SCHWARTZENTRUBER, J., FOSKOLOU, S., KILPINEN, H., RODRIGUES, J., ALASOO, K., KNIGHTS, A. J., et al. 2018. Molecular and functional variation in iPSC-derived sensory neurons. *Nature Genetics*, 501, 54-61. doi.org/10.1038/s41588-017-0005-8
- SCHWEITZER, J. S., SONG, B., HERRINGTON, T. M., PARK, T.-Y., LEE, N., KO, S., et al. 2020. Personalized iPSC-Derived Dopamine Progenitor Cells for Parkinson's Disease. *New England Journal of Medicine*, 38220, 1926-1932. doi.org/10.1056/NEJMoa1915872
- SEIBLER, P., GRAZIOTTO, J., JEONG, H., SIMUNOVIC, F., KLEIN, C. & KRAINIC, D. 2011. Mitochondrial Parkin recruitment is impaired in neurons derived from mutant PINK1 induced pluripotent stem cells. *J Neurosci*, 3116, 5970-5976. doi.org/10.1523/jneurosci.4441-10.2011
- SEKI, R., OHTA, A., NIWA, A., SUGIMINE, Y., NAITO, H., NAKAHATA, T., et al. 2020. Induced pluripotent stem cell-derived monocytic cell lines from a NOMID patient serve as a screening platform for modulating NLRP3 inflammasome activity. *PLOS ONE*, 158, e0237030. doi.org/10.1371/journal.pone.0237030
- SHAHBAZI, M. N. & ZERNICKA-GOETZ, M. 2018. Deconstructing and reconstructing the mouse and human early embryo. *Nat Cell Biol*, 208, 878-887. doi.org/10.1038/s41556-018-0144-x
- SHI, Y., INOUE, H., TAKAHASHI, J. & YAMANAKA, S. 2020. Chapter 24 - Induced pluripotent stem cell technology: venturing into the second decade. In: LANZA, R., LANGER, R., VACANTI, J. P. & ATALA, A. (eds.) *Principles of Tissue Engineering (Fifth Edition)*. Academic Press.
- SHI, Y., INOUE, H., WU, J. C. & YAMANAKA, S. 2017. Induced pluripotent stem cell technology: a decade of progress. *Nat Rev Drug Discov*, 162, 115-130. doi.org/10.1038/nrd.2016.245
- SIGGIA, E. D. & WARMFLASH, A. 2018. Modeling Mammalian Gastrulation With Embryonic Stem Cells. *Curr Top Dev Biol*, 1291-23. doi.org/10.1016/bs.ctdb.2018.03.001

- SILVA, M., DAHERON, L., HURLEY, H., BURE, K., BARKER, R., CARR, ANDREW J., et al. 2015. Generating iPSCs: Translating Cell Reprogramming Science into Scalable and Robust Biomanufacturing Strategies. *Cell Stem Cell*, 161, 13-17. doi.org/10.1016/j.stem.2014.12.013
- SIMUNOVIC, M. & BRIVANLOU, A. H. 2017. Embryoids, organoids and gastruloids: new approaches to understanding embryogenesis. *Development*, 1446, 976-985. doi.org/10.1242/dev.143529
- SIMUNOVIC, M., METZGER, J. J., ETOC, F., YONEY, A., RUZO, A., MARTYN, I., et al. 2019. A 3D model of a human epiblast reveals BMP4-driven symmetry breaking. *Nature Cell Biology*, 217, 900-910. doi.org/10.1038/s41556-019-0349-7
- SMITH, A. 2006. A glossary for stem-cell biology. *Nature*, 4417097, 1060-1060. doi.org/10.1038/nature04954
- SOUSA-ORTEGA, A., VÁZQUEZ-MARÍN, J., SANABRIA-REINOSO, E., CORBACHO, J., POLVILLO, R., CAMPOY-LÓPEZ, A., et al. 2023. A Yap-dependent mechanoregulatory program sustains cell migration for embryo axis assembly. *Nature Communications*, 141, 2804. doi.org/10.1038/s41467-023-38482-w
- SPITERI, C., CAPRETTINI, V. & CHIAPPINI, C. 2020. Biomaterials-based approaches to model embryogenesis. *Biomaterials Science*, 824, 6992-7013. doi.org/10.1039/D0BM01485K
- STREETER, I., HARRISON, P. W., FAULCONBRIDGE, A., THE HIPSCI CONSORTIUM, FLICEK, P., PARKINSON, H., et al. 2016. The human-induced pluripotent stem cell initiative—data resources for cellular genetics. *Nucleic Acids Research*, 45D1, D691-D697. doi.org/10.1093/nar/gkw928
- SUGARMAN, J. 2008. Ethical issues in stem cell research and treatment. *Cell Research*, 181, S176-S176. doi.org/10.1038/cr.2008.266
- SUGITA, S., MANDAI, M., HIRAMI, Y., TAKAGI, S., MAEDA, T., FUJIHARA, M., et al. 2020. HLA-Matched Allogeneic iPSC Cells-Derived RPE Transplantation for Macular Degeneration. *J Clin Med*, 97, 2217. doi.org/10.3390/jcm9072217
- SULLIVAN, S., STACEY, G. N., AKAZAWA, C., AOYAMA, N., BAPTISTA, R., BEDFORD, P., et al. 2018. Quality control guidelines for clinical-grade human induced pluripotent stem cell lines. *Regen Med*, 137, 859-866. doi.org/10.2217/rme-2018-0095
- SZMAŃDA, J. B. & WITKOWSKI, K. 2021. Morphometric Parameters of Krumbein Grain Shape Charts—A Critical Approach in Light of the Automatic Grain Shape Image Analysis. *Minerals*, 119, 937. doi.org/10.3390/min11090937

- TABAR, V. & STUDER, L. 2014. Pluripotent stem cells in regenerative medicine: challenges and recent progress. *Nature Reviews Genetics*, 152, 82-92. doi.org/10.1038/nrg3563
- TAKAGI, S., MANDAI, M., GOCHO, K., HIRAMI, Y., YAMAMOTO, M., FUJIHARA, M., et al. 2019. Evaluation of Transplanted Autologous Induced Pluripotent Stem Cell-Derived Retinal Pigment Epithelium in Exudative Age-Related Macular Degeneration. *Ophthalmol Retina*, 310, 850-859. doi.org/10.1016/j.oret.2019.04.021
- TAKAHASHI, K., TANABE, K., OHNUKI, M., NARITA, M., ICHISAKA, T., TOMODA, K., et al. 2007. Induction of pluripotent stem cells from adult human fibroblasts by defined factors. *Cell*, 1315, 861-872. doi.org/10.1016/j.cell.2007.11.019
- TAKAHASHI, K. & YAMANAKA, S. 2006. Induction of pluripotent stem cells from mouse embryonic and adult fibroblast cultures by defined factors. *Cell*, 1264, 663-676. doi.org/10.1016/j.cell.2006.07.024
- TAKAYAMA, K., INAMURA, M., KAWABATA, K., KATAYAMA, K., HIGUCHI, M., TASHIRO, K., et al. 2012. Efficient generation of functional hepatocytes from human embryonic stem cells and induced pluripotent stem cells by HNF4 α transduction. *Mol Ther*, 201, 127-137. doi.org/10.1038/mt.2011.234
- TAM, P. P., PARAMESWARAN, M., KINDER, S. J. & WEINBERGER, R. P. 1997. The allocation of epiblast cells to the embryonic heart and other mesodermal lineages: the role of ingression and tissue movement during gastrulation. *Development*, 1249, 1631-1642. doi.org/10.1242/dev.124.9.1631
- TAM, P. P. L. & BEHRINGER, R. R. 1997. Mouse gastrulation: the formation of a mammalian body plan. *Mechanisms of Development*, 681, 3-25. doi.org/10.1016/S0925-4773(97)00123-8
- TEN BERGE, D., KOOLE, W., FUERER, C., FISH, M., EROGLU, E. & NUSSE, R. 2008. Wnt signaling mediates self-organization and axis formation in embryoid bodies. *Cell Stem Cell*, 35, 508-518. doi.org/10.1016/j.stem.2008.09.013
- TERHUNE, A. H., BOK, J., SUN, S. & FU, J. 2022. Stem cell-based models of early mammalian development. *Development*, 14920. doi.org/10.1242/dev.201015
- TEWARY, M., OSTBLOM, J., PROCHAZKA, L., ZULUETA-COARASA, T., SHAKIBA, N., FERNANDEZ-GONZALEZ, R., et al. 2017. A stepwise model of reaction-diffusion and positional information governs self-organized human peri-gastrulation-like patterning. *Development*, 14423, 4298-4312. doi.org/10.1242/dev.149658
- THÉRY, M. 2010. Micropatterning as a tool to decipher cell morphogenesis and functions. *Journal of Cell Science*, 12324, 4201-4213. doi.org/10.1242/jcs.075150

- THIERY, J. P., ACLOQUE, H., HUANG, R. Y. J. & NIETO, M. A. 2009. Epithelial-Mesenchymal Transitions in Development and Disease. *Cell*, 1395, 871-890. doi.org/10.1016/j.cell.2009.11.007
- THOMSON, J. A., ITSKOVITZ-ELDOR, J., SHAPIRO, S. S., WAKNITZ, M. A., SWIERGIEL, J. J., MARSHALL, V. S., et al. 1998. Embryonic stem cell lines derived from human blastocysts. *Science*, 2825391, 1145-1147. doi.org/10.1126/science.282.5391.1145
- TRUBUIL, E., D'ANGELO, A. & SOLON, J. 2021. Tissue mechanics in morphogenesis: Active control of tissue material properties to shape living organisms. *Cells & Development*, 168203777. doi.org/10.1016/j.cdev.2022.203777
- TURING, A. M. 1952. The chemical basis of morphogenesis. *Philosophical Transactions of the Royal Society of London. Series B, Biological Sciences*, 237641, 37-72. doi.org/10.1098/rstb.1952.0012
- TURNER, D. A., BAILLIE-JOHNSON, P. & MARTINEZ ARIAS, A. 2016. Organoids and the genetically encoded self-assembly of embryonic stem cells. *Bioessays*, 382, 181-191. doi.org/10.1002/bies.201500111
- UMEKAGE, M., SATO, Y. & TAKASU, N. 2019. Overview: an iPS cell stock at CiRA. *Inflammation and Regeneration*, 391, 17. doi.org/10.1186/s41232-019-0106-0
- UNGRIN, M. D., JOSHI, C., NICA, A., BAUWENS, C. & ZANDSTRA, P. W. 2008. Reproducible, Ultra High-Throughput Formation of Multicellular Organization from Single Cell Suspension-Derived Human Embryonic Stem Cell Aggregates. *PLOS ONE*, 32, e1565. doi.org/10.1371/journal.pone.0001565
- VAN DEN BRINK, S. C., ALEMANY, A., VAN BATENBURG, V., MORIS, N., BLOTENBURG, M., VIVIÉ, J., et al. 2020. Single-cell and spatial transcriptomics reveal somitogenesis in gastruloids. *Nature*, 5827812, 405-409. doi.org/10.1038/s41586-020-2024-3
- VAN DEN BRINK, S. C., BAILLIE-JOHNSON, P., BALAYO, T., HADJANTONAKIS, A. K., NOWOTSCHIN, S., TURNER, D. A., et al. 2014. Symmetry breaking, germ layer specification and axial organisation in aggregates of mouse embryonic stem cells. *Development*, 14122, 4231-4242. doi.org/10.1242/dev.113001
- VIANELLO, S. & LUTOLF, M. P. 2019. Understanding the Mechanobiology of Early Mammalian Development through Bioengineered Models. *Dev Cell*, 486, 751-763. doi.org/10.1016/j.devcel.2019.02.024
- VICKERS, A., TEWARY, M., LADDACH, A., POLETTI, M., SALAMETI, V., FRATERNALI, F., et al. 2021. Plating human iPSC lines on micropatterned substrates reveals role for ITGB1 nsSNV in endoderm formation. *Stem Cell Reports*, 1611, 2628-2641. doi.org/10.1016/j.stemcr.2021.09.017

- VIGILANTE, A., LADDACH, A., MOENS, N., MELECKYTE, R., LEHA, A., GHAHRAMANI, A., et al. 2019. Identifying Extrinsic versus Intrinsic Drivers of Variation in Cell Behavior in Human iPSC Lines from Healthy Donors. *Cell Reports*, 268, 2078-2087.e2073. doi.org/10.1016/j.celrep.2019.01.094
- VINING, K. H. & MOONEY, D. J. 2017. Mechanical forces direct stem cell behaviour in development and regeneration. *Nature Reviews Molecular Cell Biology*, 1812, 728-742. doi.org/10.1038/nrm.2017.108
- VITILLO, L. & KIMBER, S. J. 2017. Integrin and FAK Regulation of Human Pluripotent Stem Cells. *Curr Stem Cell Rep*, 34, 358-365. doi.org/10.1007/s40778-017-0100-x
- VOLPATO, V. & WEBBER, C. 2020. Addressing variability in iPSC-derived models of human disease: guidelines to promote reproducibility. *Dis Model Mech*, 131. doi.org/10.1242/dmm.042317
- WAINGER, B. J., KISKINIS, E., MELLIN, C., WISKOW, O., HAN, S. S., SANDOE, J., et al. 2014. Intrinsic membrane hyperexcitability of amyotrophic lateral sclerosis patient-derived motor neurons. *Cell Rep*, 71, 1-11. doi.org/10.1016/j.celrep.2014.03.019
- WALTERS, N. J. & GENTLEMAN, E. 2015. Evolving insights in cell-matrix interactions: elucidating how non-soluble properties of the extracellular niche direct stem cell fate. *Acta Biomater*, 113-16. doi.org/10.1016/j.actbio.2014.09.038
- WARMFLASH, A., SORRE, B., ETOC, F., SIGGIA, E. D. & BRIVANLOU, A. H. 2014. A method to recapitulate early embryonic spatial patterning in human embryonic stem cells. *Nature Methods*, 118, 847-854. doi.org/10.1038/nmeth.3016
- WARREN, L., MANOS, P. D., AHFELDT, T., LOH, Y.-H., LI, H., LAU, F., et al. 2010. Highly Efficient Reprogramming to Pluripotency and Directed Differentiation of Human Cells with Synthetic Modified mRNA. *Cell Stem Cell*, 75, 618-630. doi.org/10.1016/j.stem.2010.08.012
- WISEMAN, E., ZAMUNER, A., TANG, Z., ROGERS, J., MUNIR, S., DI SILVIO, L., et al. 2019. Integrated Multiparametric High-Content Profiling of Endothelial Cells. *SLAS DISCOVERY: Advancing the Science of Drug Discovery*, 243, 264-273. doi.org/10.1177/2472555218820848
- WOLPERT, L., TICKLE, C. & ARIAS, A. M. 2015. *Principles of development*, Oxford University Press, USA
- WU, S. M. & HOCHEDLINGER, K. 2011. Harnessing the potential of induced pluripotent stem cells for regenerative medicine. *Nature Cell Biology*, 135, 497-505. doi.org/10.1038/ncb0511-497

- YAMADA, Y., ONDA, T., HAGIUDA, A., KAN, R., MATSUNUMA, M., HAMADA, K., et al. 2022. RGDX1X2 motif regulates integrin $\alpha v\beta 5$ binding for pluripotent stem cell adhesion. *The FASEB Journal*, 367, e22389. doi.org/10.1096/fj.202200317R
- YAMANAKA, S. 2012. Induced pluripotent stem cells: past, present, and future. *Cell Stem Cell*, 106, 678-684. doi.org/10.1016/j.stem.2012.05.005
- YAMANAKA, S. 2020. Pluripotent Stem Cell-Based Cell Therapy-Promise and Challenges. *Cell Stem Cell*, 274, 523-531. doi.org/10.1016/j.stem.2020.09.014
- YU, J., CHAU, K. F., VODYANIK, M. A., JIANG, J. & JIANG, Y. 2011. Efficient Feeder-Free Episomal Reprogramming with Small Molecules. *PLOS ONE*, 63, e17557. doi.org/10.1371/journal.pone.0017557
- ZHAI, J., XIAO, Z., WANG, Y. & WANG, H. 2022. Human embryonic development: from peri-implantation to gastrulation. *Trends in Cell Biology*, 321, 18-29. doi.org/10.1016/j.tcb.2021.07.008
- ZHOU, W. & FREED, C. R. 2009. Adenoviral gene delivery can reprogram human fibroblasts to induced pluripotent stem cells. *Stem Cells*, 2711, 2667-2674. doi.org/10.1002/stem.201
- ZHU, Z. & HUANGFU, D. 2013. Human pluripotent stem cells: an emerging model in developmental biology. *Development*, 1404, 705-717. doi.org/10.1242/dev.086165